Surface studies of ionic oxides by electron spectroscopy

by

Martin Dennis Patrick Cotter B.Sc.

A thesis submitted for the degree of Doctor of Philosophy of the University of London and for the Diploma of Membership of Imperial College.

Department of Chemistry

Imperial College

London SW7 2AZ

Febuary 1988

To my parents, my brothers and Carol

..... eventually !!

The Meek

Acknowledgements

I would like to express my thanks and appreciation to my supervisor Russ for all his efforts.

I have had numerous exemplars whilst in the ESCALAB and would also like to thank them for their time and patience.

I would like also to thank the SERC for funding and to Dr.W.C.Mackrodt & ICI for their sponsorship.

Thankyou to a few of the group on level four.

Abstract

This thesis is concerned with segregation of cation dopants in oxide systems and with the structure of segregated overlayers.

Yttrium segregation in YSCZ (Yttrium stabilized cubic zirconia)was found to be present over a large depth compared with the pathlength of the electrons in XPS. Electron bombardment caused an anomalous reduction of the crystal with resulting in an oxygen desorption cross section calculated to be 3.9×10^{-20} cm^2.

Surface segregation of Ba from doped polycrystalline and single crystal MgO has been studied by XPS showing little variation in surface coverage of Ba over a range of bulk doping levels from 7ppm to 7000ppm in ceramic pellets equilibrated at 1630K. This is consistent with surface coverages derived from ionic model simulations of the surface if due account is taken of the strong variation of the segregation energy with coverage. The coverage of Ba on a MgO(001) single crystal surface doped by in-diffusion of Ba deposited onto the crystal can be made similar to that of the polycrystalline material. The Ba-segregated MgO(001) surface exhibits a complex LEED pattern.

Ordered BaO overlayers have been grown on MgO(001) by successive cycles of Ba deposition, oxygen exposure and high temperature annealing. The overlayers adopt the lattice spacing characteristic of bulk BaO for coverages in excess of 3 monolayers. Owing to the near equality between a_0(BaO) and $\sqrt{2}a_0$(MgO) the {20} LEED spots from MgO lie

close to {11} spots from the substrate. Ionic model calculations confirm that the surface structure proposed for BaO on MgO is energetically favoured with respect to alternative configurations.

Contents

		Page
Chapter 1	**Introduction**	1
1.1	Background to the present work	2
1.2	Basic principles of photoelectron spectroscopy	3
1.2.1	Introduction	3
1.2.2	The three step model	5
1.2.3	XPS	7
1.2.4	Primary structure in XPS	8
1.2.5	Satellite structure in XPS	18
1.2.6	Angular variation in XPS	19
1.2.7	Quantification of XPS	21
1.3	LEED	24
1.3.1	Introduction	24
1.3.2	Coherence length in LEED	25
1.4	Energy loss spectroscopy (ELS)	27
Chapter 2	**Experimental**	30
2.1	Introduction	31
2.2	The pumping system	33
2.3	Sample manipulation	34
2.4	The gas line and gas dosing	35
2.5	Introducing a new sample	35
2.6	Radiation sources	36
2.6.1	X-ray source	36
2.6.2	Impurity radiation in XPS	36
2.6.3	The ELS electron source	41
2.7	The analyser and lens system	41
2.7.1	The effect of pass energy and analyser slit width on analyser resolution	45

2.7.2 Modes of Analyser operation 46

2.8 Electron counting 48

2.9 Data storage and manipulation 49

2.10 The LEED gun and grid system 49

2.10.1 The LEED system 49

2.10.2 LEED detection 50

2.11 Internal sample preparation 51

2.11.1 Crystal annealing and heating 51

2.11.2 Argon etching. 54

Chapter 3 The study of yttrium stabilized cubic zirconia (YSCZ) 58

3.1 Introduction 59

3.2 Sample preparation 61

3.2.1 External 61

3.2.2 Internal 63

3.3 LEED studies of YSCZ 16% 64

3.3.1 Polar surfaces 68

3.3.2 Discussion of possible structures for YSCZ 72

3.4 XPS Studies of YSCZ 74

3.4.1 The quantification of Y^{3+} segregation 74

3.4.2 XPS shake-up structure comparison with Y_2O_3 and ZrO_2 82

3.5 Electron beam reduction of YSCZ 16% 88

3.5.1 Quantification of oxygen loss in the electron beam reduction of YSCZ 92

3.5.2 The oxidation of zirconium foil 99

3.6 ELS 101

Chapter 4 Electron spectroscopy of MgO (100) 107

4.1 Introduction 108

4.2 Experimental 112

4.3 XPS of MgO 116

4.4 The surface-core shift 128

Chapter 5 Growth of BaO overlayers on MgO(001) 132

5.1 Introduction 133

5.2 Experimental 135

5.2.1 MgO crystal preparation 135

5.2.2 The Ba Evaporator 135

5.2.3 R.F. heating/annealing 138

5.2.4 Oxygen dosing 138

5.2.5 Experimental flow chart 139

5.3 XPS results 139

5.3.1 XPS of Ba metal (only) growth on MgO(100) 139

5.3.2 XPS of epitaxial growth of BaO on MgO 139

5.3.3 The anomolous chemical shift associated with Ba and Ba^{2+} 147

5.3.4 Quantification of XPS associated with BaO coverages 148

5.4 ELS 152

5.5 LEED and the structure of BaO overlayers on MgO 154

5.6 Ionic model simulation of the MgO/BaO interface 160

Chapter 6 Barium segregation in doped MgO 166

6.1 Introduction 167

6.2 Experimental 170

6.3 Results 172

6.4 The heat of segregation 185

6.5 Segregation isotherms 187

References 194

Appendix A 207

Appendix B 212

List of figures

Chapter 1

Figure 1.1 The band structure for metals, semiconductors and insulators and the energy level diagram for photoemission. 9

Figure 1.2 The mean free path of electrons in solids versus electron energy. 11

Figure 1.3 XPS spectra of MgO (001). 12

Figure 1.4 Pictorial representation of the cross section of a 1:s orbital. 15

Figure 1.5 X-ray and Auger electron emission associated with core hole decay. 17

Figure 1.6 A typical ELS spectrum. 28

Chapter 2

Figure 2.1 The VG ESCALAB. 32

Figure 2.2 The X-ray source. 37

Figure 2.3 XPS spectra showing crossover and shadow peaks. 39

Figure 2.4 XPS spectrum showing O:Kα impurity radiation. 40

Figure 2.5 The LEG31 electron gun used for ELS. 42

Figure 2.6 Showing the path of the photoelectrons and the schematic of the counting electronics. 43

Figure 2.7 Energy level schematic for XPS. 44

Figure 2.8 Analyser transmission characteristics for CAE. 44

Figure 2.9 A schematic of the RF feedthrough. 53

Figure 2.10 Photograph of the RF feedthrough on the ESCALAB. 55

Figure 2.11 Photograph of YSCZ(001) being heated to white heat within the RF coil. 56

Chapter 3

Figure 3.1 LEED of 16Z YSCZ at 106eV beam energy. 65

Figure 3.2 LEED of 16% YSCZ at 106 eV beam energy 66

Figure 3.3 Plot of sinθ against $E^{-1/2}$ for YSCZ. 67

Figure 3.4 The possible crystal terminations of the fluorite structure in relation to YSCZ. 70

Figure 3.5(a) The flourite structure.(b) The addition of a half monolayer of O atoms. 71

Figure 3.6 (a) Al:Kα XPS of the 3d region of YSCZ(16%) (b) Mg:Kα XPS of the 3d region of YSCZ (9%). 75

Figure 3.7 Mg Kα wide scan spectra of 16% YSCZ. (a) Resistively annealed sample (b) Electron bombarded sample (c) Argon ion etched sample 76

Figure 3.8 Variation of Y/Zr ratio region versus kinetic energy for 16% YSCZ. 77

Figure 3.9 (a) Mg:Kα XPS of the 3d region of ZrO_2(b) Al:Kα XPS of the 3d region of Y_2O_3. 83

Figure 3.10 A schematic of the two suggested mechanisms for the formation of shake up satellites. 86

Figure 3.11 Mg Kα XPS spectra of YSCZ in the 3p region. 89

Figure 3.12 Mg:Kα XPS spectra of YSCZ (16%) in the 3d region. 90

Figure 3.13 XPS of 16% YSCZ after 1000 seconds of electron bombardment at 2.5 KeV and 5mA/cm^2 target current. 91

Figure 3.14 Variation with time of the Zr:3p and Y:3p signals in the Mg:Kα excited XPS spectrum of YSCZ. 93

Figure 3.15 The variation with time in the O:1s/Zr:$3p_{3/2}$ intensity ratio under electron irradiation as in figure 3.14. 94

Figure 3.16 schematic showing the mechanism for the electron stimulated desorption in YSCZ. 96

Figure 3.17 The variation of XPS in the Zr:3p region with oxygen dosing. 100

Figure 3.18 (a) ELS spectrum of 9% YSCZ annealed in oxygen with RF heating. (b) ELS spectrum of the same crystal after electron bombardment. 102

Figure 3.19 (a) ELS of YSCZ after more electron bombardment (b) ELS of YSCZ after argon bombardment. 103

Figure 3.20 The absorption spectrum of electron bombarded YSCZ. 106

Chapter 4 107

Figure 4.1 Schematic representation of the (100) surface of MgO (NaCl type). 110

Figure 4.2 LEED pattern of MgO(001) (a) 187eV beam energy (b) 141eV beam energy. 113

Figure 4.3 LEED MgO(001) with RF annealing after argon ion etching. 114

Figure 4.4 LEED MgO(001) with RF annealing only: (a) 57eV beam energy, (b) 100eV beam energy. 115

Figure 4.5 ELS spectrum of clean annealed MgO(001). 117

Figure 4.6 Wide scan XPS spectra of MgO(001) using (a) Mg:Kα and Al:Kα exciting radiation (b) Al:Kα exciting radiation. 118

Figure 4.7 Al:Kα excited Auger spectra of MgO(001). 120

Figure 4.8 Narrow scan XPS spectra of O:1s and Mg:1s core levels and associated satellite structure. 121

Figure 4.9 Narrow scan XPS spectra of the principle Mg core lines and their FWHM. 122

Figure 4.10 Diagram showing the origin of the phonon broadening of core lines. 125

Figure 4.11 O1s XPS spectra of clean annealed MgO(001) at (a) 90° and (b) 15° angle of emission. 130

Chapter 5 132

Figure 5.1 Diagram of the barium getter source. 137

Figure 5.2 Experimental flow chart of the method of BaO growth. 140

Figure 5.3 Ratio of Ba:$3d_{5/2}$ / Mg:1s monitored as a function of evaporation time. 141

Figure 5.4 Widescan Al:Kα excited XPS of (a) clean MgO(001) (b) BaO overlayer about 4 monolayers thick. 143

Figure 5.5 Ba:3d core level spectra showing the relative increase in the intensity with deposition time 144

in conjunction with figure 5.3.

Figure 5.6 O:1s core level structure in Al:Kα XPS at normal emission as a function of increasing BaO coverage. 145

Figure 5.7 O:1s spectra of MgO and BaO on MgO demonstrating angle resolved XPS 146

Figure 5.8 Calculated Ba:$3d_{5/2}$/Mg:1s XPS intensity ratio as a function of BaO coverage. 151

Figure 5.9 EEL spectra excited with 100eV electron beam in specular mode. 153

Figure 5.10 A plot of sinθ versus $1/E^{1/2}$ for the lowest order spots of MgO. 155

Figure 5.11 LEED of MgO 157

Figure 5.12 LEED pattern of BaO on MgO at 142 eV beam energy 158

Figure 5.13 LEED spot pattern of the identical crystal as in figure 5.12 but at 97.6 eV beam energy. 159

Figure 5.14 Schematic of the MgO and BaO blocks used in the ionic model calculations. 162

Figure 5.15 The plan view of the alternative configurations for the growth of BaO on MgO(001). 164

Figure 5.16 Fully relaxed structure for 2 monolayers of BaO on MgO. 165

Chapter 6

Figure 6.1 Widescan XPS excited with Al:Kα radiation for Ba doped MgO ceramic pellets. 173

Figure 6.2 Ba:3d structure in Al:Kα XPS of doped MgO ceramic pellets. 175

Figure 6.3 Intensity ratio between Ba:$3d_{5/2}$ and Mg:1s peaks in Mg:Kα XPS of Ba-doped MgO as a function bulk doping level. 176

Figure 6.4 Comparison between Ba:3d structure (a) from bulk BaO and (b) from Ba-segregated MgO. 179

Figure 6.5 The variation of Ba:$3d_{5/2}$ to Mg:1s intensity ratio as a function of angle of take-off of photoelectrons. 180

Figure 6.6 The calculated variation of Ba:$3d_{5/2}$ to Mg:1s 181

intensity ratio with substitutional incorporation of Ba at the Mg(001) surface.

Figure 6.7 LEED patterns for Ba-segregated MgO(001) as descibed in the text 182

Figure 6.8 Surface coverages of Ba at MgO(001) as a function of temperature. 190

List of Tables

Table 3.1	XPS of 16% YSCZ excited by MgKα radiation	79
Table 3.2	Angle resolved XPS of 9% YSCZ	80
Table 3.3	Spin orbit splittings in XPS of YSCZ	80
Table 3.4	XPS shake-up energies for YSCZ, Y_2O_3 and ZrO_2	80
Table 6.1	Heats of segregation of Ba to the MgO(001) surface	191

Chapter 1. Introduction

1.1 Background to the present work

The properties of oxide surfaces and their interactions with adsorbates play an important part in a number of areas of contemporary materials research including catalysis, ceramic technology and corrosion science. A better understanding of the stability and structure of crystal surfaces is hence of fundamental importance. It is well known that if sufficient cation impurity or dopant is present in the crystal there is the possibility of surface segregation and subsequent modification of the electronic and structural properties at the surface.

The study of crystal surface structure and of segregation has been made easier by the advent of Ultra High Vacuum (UHV) spectroscopies which have surface sensitivities of a few tens of Angstroms or less. This work concerns the application of three techniques to the study of segregation and surface structure in: yttrium stabilized cubic zirconia (YSCZ) (100), MgO(001), BaO overlayer growth on MgO(001) and BaO doped MgO polycrystalline pellets. When applicable the surface structure and reconstructions have been investigated by LEED(Low energy electron diffraction) surface composition by XPS (x-ray photoelectron spectroscopy) and surface electronic structure by ELS (electron energy loss spectroscopy).

This work was done in close collaboration with the theoretical modelling of segregation and related phenomena in oxides by W.C.Mackrodt et al at ICI Runcorn.

1.2 Basic principles of Photoelectron Spectroscopy

1.2.1 Introduction

The photoelectric effect involves emission of electrons from a solid under irradiation with radiation of a fixed frequency. Einstein[1] showed in 1905 that previous experiments demonstrating the photoelectric effect could be explained by quantum theory and that they obeyed the equation:

$$E_k = h\nu - E_b - \phi \qquad \ldots. 1.1$$

Where E_k is the kinetic energy of the excited electrons, $h\nu$ is the energy of the incident photons, ϕ is the work function[2] of the solid and E_b is the binding energy of the electron relative to the vacuum level.

The basis of photoelectron spectroscopy is the measurement of the kinetic energy of the emitted electron and the determination of E_b through equation 1.1. E_b for a particular species of photoelectron represents the energy difference between the initial and final states of the total system and as such problems in its theoretical estimation become apparent as the hole state is left to relax through various electronic processes. Koopmans[3] showed that if one assumes that there is no change in the wavefunctions of the electrons other than for that ejected (the "sudden" approximation), the negative of the orbital enegy calculated from Hartree-Fock equations is equivalent

to the binding energy. This neglects the relaxation of the hole state and electron correlation terms, but has proved to be useful in that it often gives a qualitatively correct ordering of energy levels.

A photo-electron spectrum (PES) is an energy distribution curve of counts of electrons (proportional to photoelectron current) per kinetic energy increment against electron energy. The distribution mirrors the electronic structure of the analysed material, as a loosely bound electron will be ejected with a higher kinetic energy than a tightly bound or core electron.

The ionizing photons most frequently used in modern PES experiments are so called HeI (21.2eV) and HeII(40.8eV) from a helium discharge lamp, X-rays such as AlKα(1487eV) and MgKα(1254eV) induced by high energy electron bombardment of the metal targets, and synchrotron radiation emitted by high energy electrons induced to move in a curved path. Ultra-violet radiation with a maximum energy of 40.8eV from discharge lamps restricts the excitation to within the valence levels, whereas X-rays excite both core and valence electrons. Synchrotron[4] radiation provides a continuously tunable source of radiation extending from the infrared through to ultraviolet and X-ray region. However, synchrotrons are large scale installations, and in many cases the radiation for surface science experiments is a by-product of high energy physics experiments.

The PES in this work mostly concerns X-ray photoelectron spectroscopy (XPS) which uses the second type

of ionising radiation.

1.2.2 The three step model[5]

The process of photoemission from a solid can be described by a three step model;(1) the initial photoionisation,(2) the transport of the electron to the surface and (3) the emission of the electron into the vacuum.

Photoionisation

Absorption of a photon from the incident radiation can excite a bound electron into an electronic state above the Fermi level. If the excitation energy is relatively low (as in UPS) there is the possibility of the excited electron being placed just above the Fermi energy where the density of empty states (DOS) is highly structured. The excitation probability for polycrystalline materials then represents a convolution of the filled and empty density of states. If the exciting radiation is of relatively high energy, as in XPS, the electron will usually be placed in a continuum state where it is essentially free (the empty DOS is relatively unstructured) but under the influence of pertubations of the periodic potential of the lattice[6].

Transportation

Although photons, which have a weak interaction with matter[7], can travel several thousand Angstroms into the bulk, the electrons created by photoionisation have strong interactions and only a small percentage escape into the

vacuum. The various inelastic interactions (electron-electron, electron-phonon, electron-plasmon, interband transitions,) produce a large backround in the spectrum on which the unscattered flux due to photoionisation sits. It must however be recognised that valence electron excitation may be synchronous with the primary photoionisation event, producing so-called shake up peaks in experimental spectra. The effect ofintrinsic and extrinsic loss processes on the spectrum in XPS is to produce an increased background directly after a peak resulting in the spectra having an increasing background intensity towards lower kinetic energy.

In the simplest model the intensity of electrons reaching the surface is a function of the inelastic mean free path (IMFP)[8] with the intensity of the emerging flux corresponding to a Beer-Lambert type law such that:

$$I(x) = I_o(x)\exp-(x/\lambda\cos\alpha) \quad \ldots. 1.2$$

Where:

I(x) is the intensity of the emerging flux from depth x

$I_o(x)$ is the photoelectron flux at a particular KE

x is the depth below the surface

λ is the inelastic mean free path (IMFP) defined as the depth from which 1/e of the photoelectrons produced at the depth escape from the solid surface with the same kinetic energy.

α is the angle between the surface normal and the analyser

The values of IMFPs are the subject of debate[9], but there has been formulated a "universal curve" which has been derived from studies on a wide range of materials and is shown in figure 1.1. Leckey and co-workers[10] have derived a theoretical expression for λ of the form $AE_k^{3/4}$ where A is a constant dependent on the sample and E_k the kinetic energy. This relationship only applies at relatively high kinetic energy where the electron energy is much greater than that of the excitations responsible for inelastic scattering. Various calculations using this method have been applied to XPS quantification in Chapters 4 and 5 and all pathlengths calculated come within the bounds of the universal curve. A fuller explanation can be found in Appendix B.

Emission of electrons and the work function

For photoemission to occur the electron must overcome a potential barrier at the surface, known as the work function. The work function arises because of differences in coordination between the surface and the bulk and is usually defined as the potential between the vacuum level and the Fermi level inside the solid[11].

1.2.3 XPS

Introduction

The technique of XPS utilises X-ray radiation to stimulate emission and was initially developed by Siegbahn and co-workers[12] using $MoK\alpha_1K\alpha_2$ radiation (17479eV) which

is energetic enough to excite most core levels. They found that the core-level peaks appearing in the XPS spectrum are characteristic of individual elements and proceeded to build up tabulations of core binding energies. Their pioneering work and subsequent improvement of tables within the literature allows the qualitative use of binding energies in determining unknown elements in various samples, which is still an important use of XPS. Such use of electron spectroscopy for chemical analysis leads to the acronym ESCA.

When working with insulators (as in this work) the Fermi level can be anywhere in the band gap and sample charging due to loss of photoelectrons may occur. Binding energies with respect to the Fermi level of the spectrometer are therefore not valid. Charge compensation from electron flood guns or the use of metal overlayers to provide a BE reference are often used in this situation. An alternative procedure, and that taken here, is to measure energies from a well-defined feature of the electronic structure like a valence band edge or a narrow XPS peak.

Most modern spectrometers have MgKα and AlKα dual radiation sources. The X-rays are produced by the $2P_{(1/2),(3/2)} \longrightarrow 1S$ transition induced by high energy electron bombardment. More novel (Ag and Zr)[13] anodes are being added to further improve the excitation capabilities.

1.2.4 Primary structure in XPS

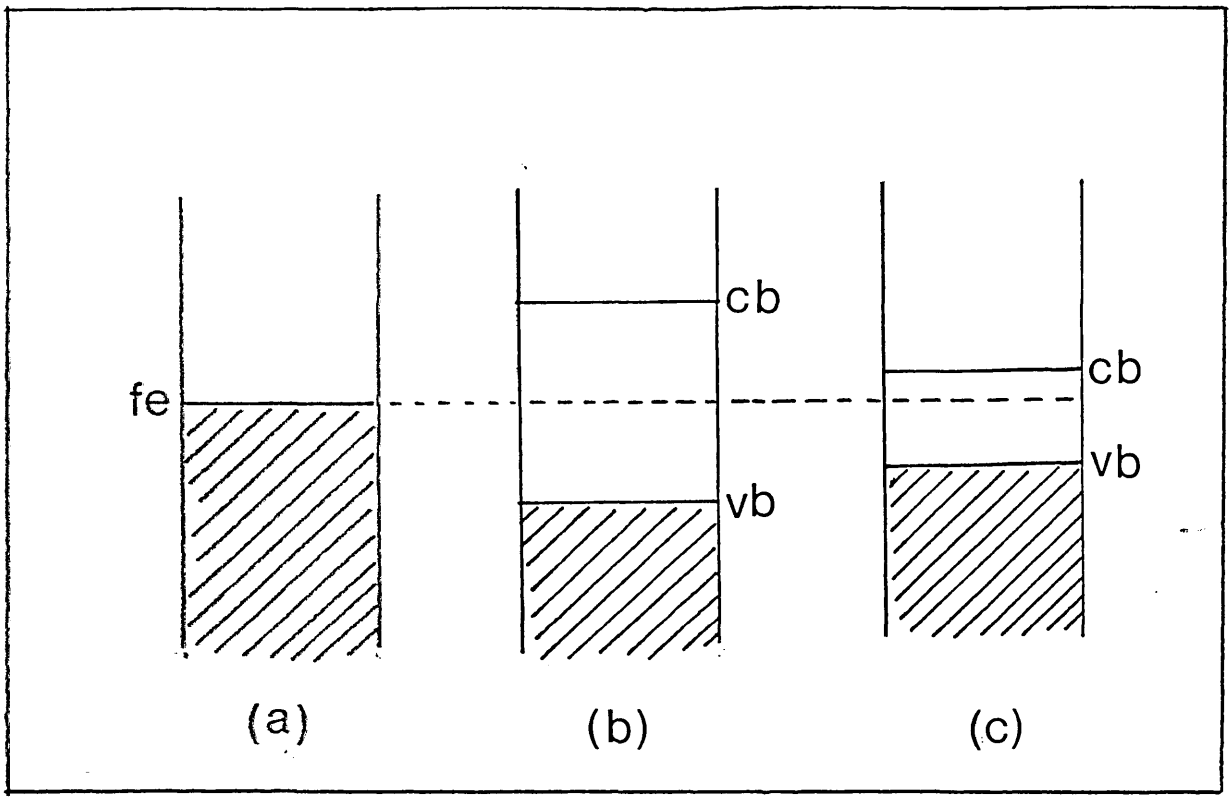


Figure 1.1 A schematic of the band structure of metals semiconductors and insulators with respect to the vacuum level.

(a) Metal , (b) Insulator where the fermi level at mid gap due to e-h pair excitation and (c) Semiconductor where the fermi level is pinned by n-type donor states below the CB edge.

Core levels

A typical XPS widescan spectrum of MgO can be seen in figure 1.2 and shows a series of labelled peaks on a large background. In fact within the bounds of the energy of the photon source core levels of every element present in the sample will be excited (and to within the sensitivity of the instrument). Qualitative identification is made by checking the binding energy of the individual peaks against literature values. Narrower scans are taken for more accurate quantification and examination of details of peak shapes.

Chemical shifts[14],[15]

The binding energy of core electrons is sensitive to the distribution of electrons in the valence levels of the sample of interest. Similar to NMR the non-equivalence of atoms, due to their differing chemical environment, manifests itself as a chemical shift. In principle each set of chemically inequivalent atoms will give a distinct core binding energy in XPS. The shift is generally to a higher binding energy with increasing oxidation state or with the more electronegative ligands. A well known exception is the chemical shift between Ba and Ba^{2+}, where anomalously, the inner 3d electrons are easier to withdraw in the ion than in the metal. This is further discussed in Chapter 5.

Spin orbit splitting

Ejection of an electron from inner core levels other

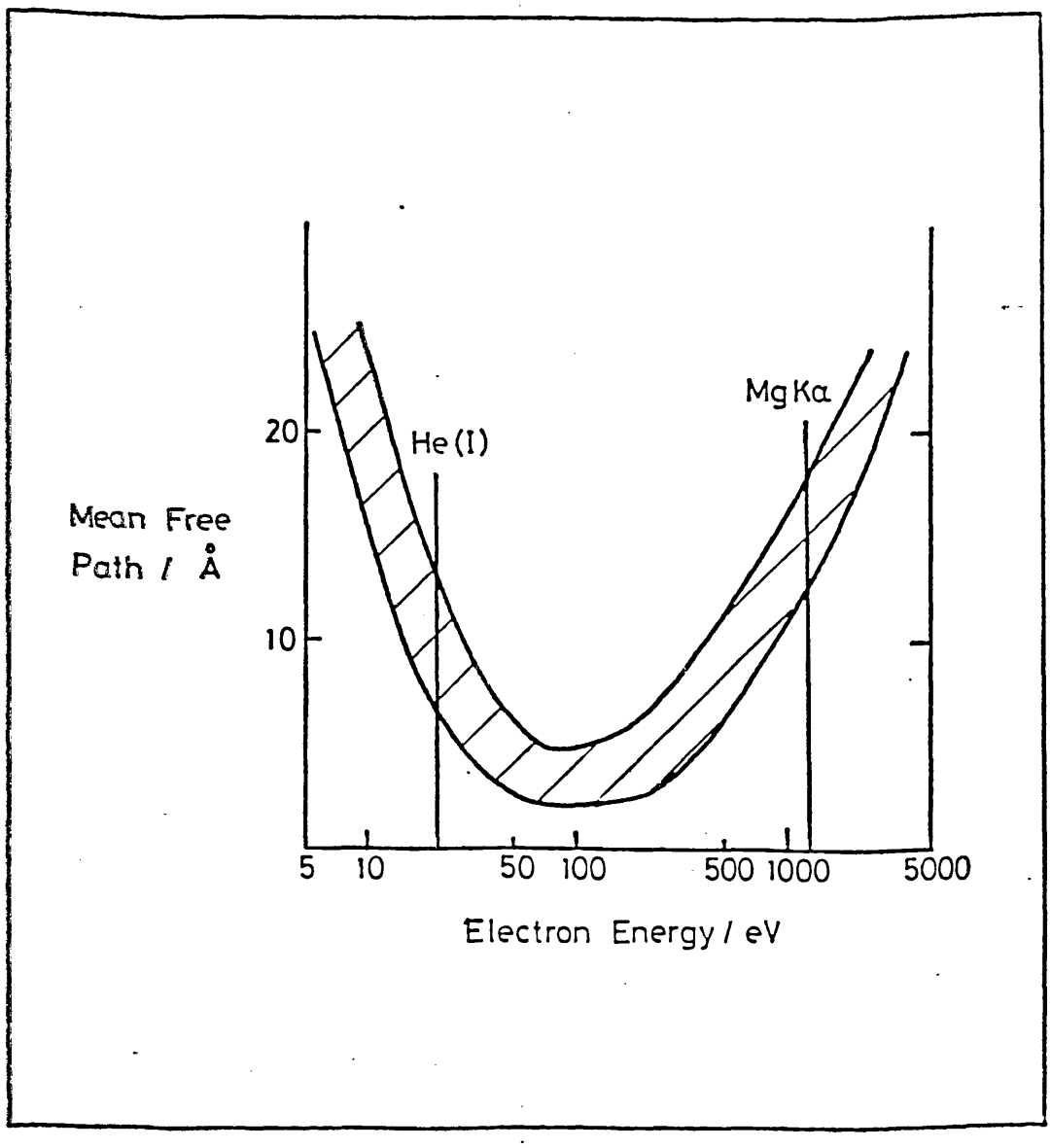


Figure 1.2 The mean free path of electrons in solids as a function of electron energy[8]. He(I) and Mg:Kα radiations are shown. The shaded region represents the error involved with the "universal curve".

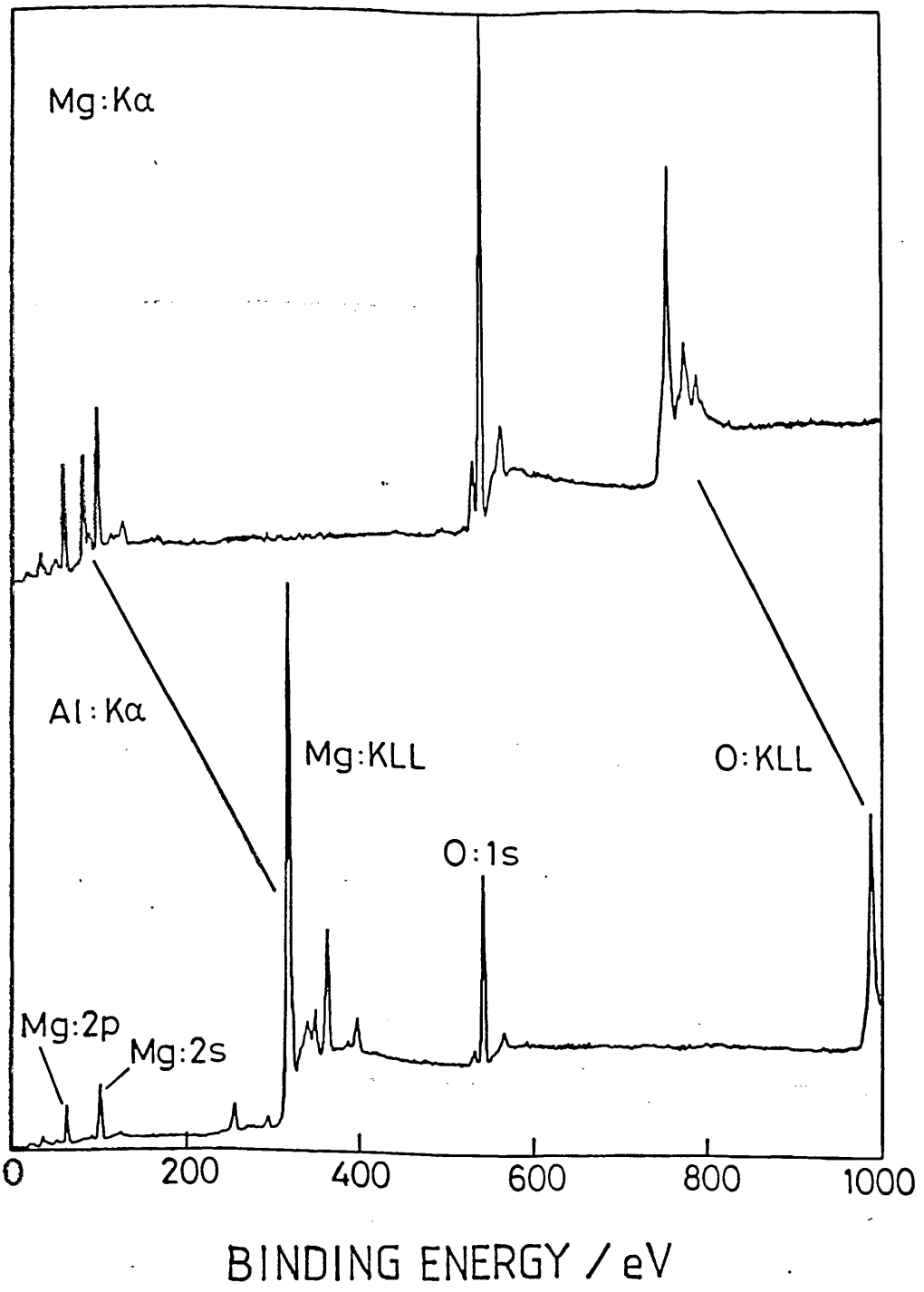


Figure 1.3 XPS spectra of MgO(001). Note the core level identification and the binding energy shift of the core levels with the use of different exciting radiation.

than s-levels results in a splitting of the XPS photoemission peak due to the coupling between the unpaired spin in the final state and the orbital angular momentum associated with a single hole. The total angular momentum for the peak is characterised by a quantum number j which is the vectorial sum of the individual electron spin s and angular momenta l. The intensity corresponding to the individual j and s values for two photoelectron peaks is given by:

$$\frac{I_a}{I_b} = \frac{2j_a + 1}{2j_b + 1} \qquad \ldots 1.3$$

For example the ratio of $Zr{:}3p_{3/2}$ and $Zr{:}3p_{1/2}$ is 2:1. The photoelectron corresponding to the highest j value in the final state ion has the higher kinetic energy.

The photoionisation cross section

The relative intensity of core-peaks is a function of the photo-ionization cross section α which is proportional to the square of the transition dipole matrix.

$$\sigma_{v(i)} \propto |M_{if}|^2 = \sum_{if} |\langle f| \sum_{\mu} r_{\mu} |i\rangle|^2 \qquad .... 1.4$$

where $\sigma_{v(i)}$ is the photoionisation cross section with exciting radiation of frequency v

$|i\rangle$ is the wave function for the initial state

$|f\rangle$ is the wave function for the final state

r_μ is the dipole moment operator

With XPS the final state of the electron is in the continuum. However a useful approximation[16] is to assume that the electron ejected from an inner shell has a free-electron-like wave function with a phase shift determined by the final state angular momentum and internal dynamics of the atom. Equation 1.4 then allows us to see how σ varies with electron kinetic energy as the matrix element between initial and final states alters. For example figure 1.4 shows the 1s orbital wave function and its overlap with a free-electron-like sine function, showing the resultant cross section beside.

Values of σ have been calculated and tabulated by Scofield[23] amongst others. Evans[24] et al have compiled empirical values of cross sections from studies on a wide range of compounds. These generally agree with Scofield's values.

Peak Widths

The measured peak width at half maximum (FWHM)[11] in XPS has several contributions: the natural line width of the core level, the X-ray line width and the analyser resolution. If we assume a Gaussian line-shape these contributions equate to the total width such that:

$$\Delta E = (\Delta E_n^2 + \Delta E_p^2 + \Delta E_a^2)^{1/2} \quad .... \ 1.5$$

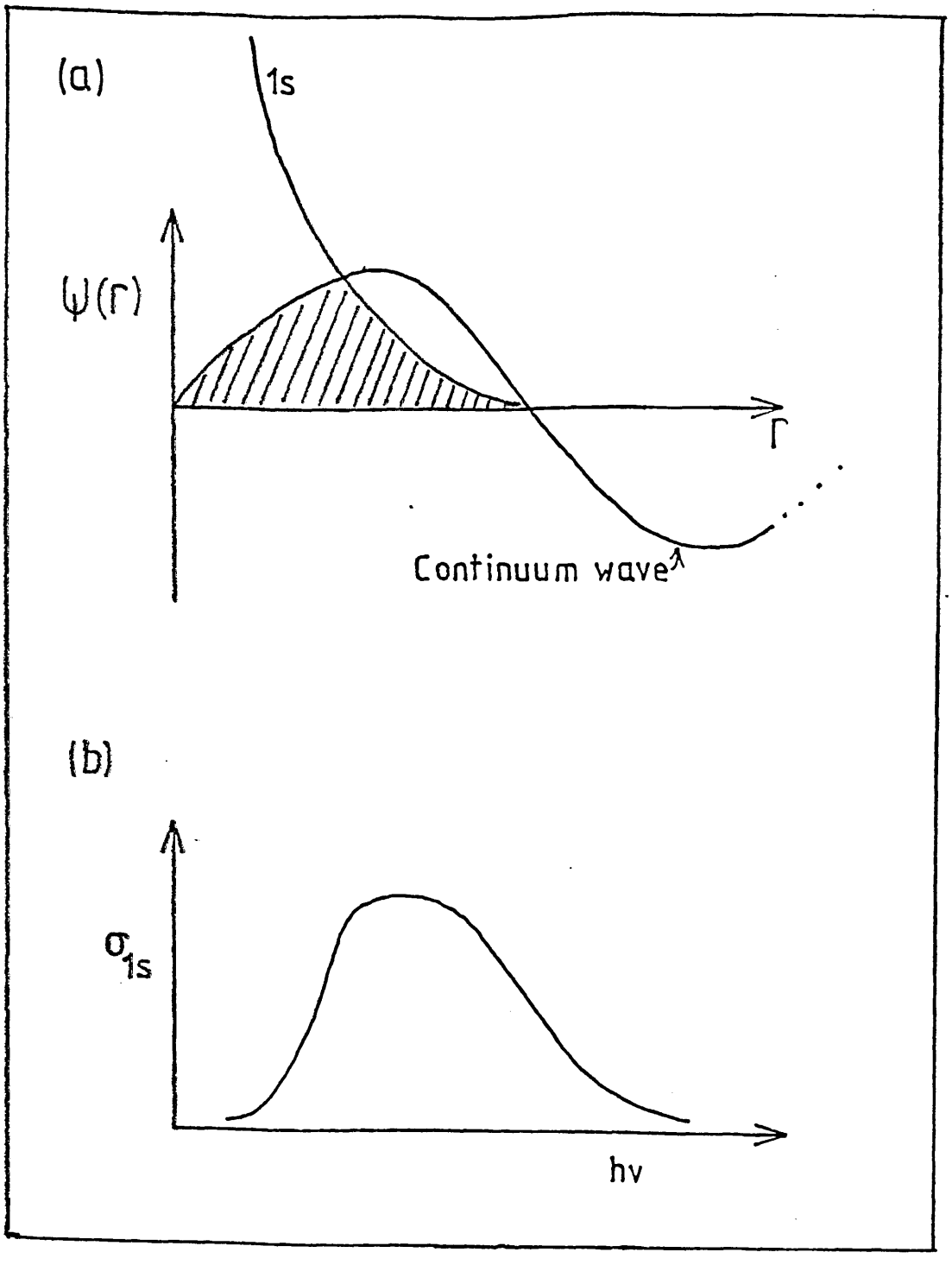


Figure 1.4 (a) The overlap of the 1s orbital with the continuum wave function represented as a sine function or free electron like. (b) The resultant ionisation cross section as a result of (a). The area under the curve would drastically change with the frequency of the sine function, the energy of the exciting radiation and the core level radial wave function.

Where: ΔF_n is the natural line width of the core level(see below)

ΔF_p is the width of the photon source

ΔF_a is the analyser resolution

The natural linewidth of Mg:Kα is less than Al:Kα and is therefore the preferred excitation as this results in a smaller FWHM of the peak. Al:Kα has the advantage that it can excite more tightly bound core-levels as it is higher in energy.

The uncertainty principle determines the natural linewidth of the core level (which is a function of the time taken for the core hole to decay) such that the lifetime τ is defined as:

$$\tau = h / 2\pi \Gamma \quad .... \ 1.6$$

Where Γ is the natural linewidth. For example the peak of Mg:1s only lasts for about 10^{-14} — 10^{-15} seconds.

It was recognised some time ago[17][18] that for metal oxides the peak widths are larger than that found for corresponding metals and it was shown that phonon broadening must be included in the calculations of the FWHM. Further calculations associated with the peaks for MgO(100) are found in chapter 4.

Core-hole decay

Final state effects play a vital role in XPS. The

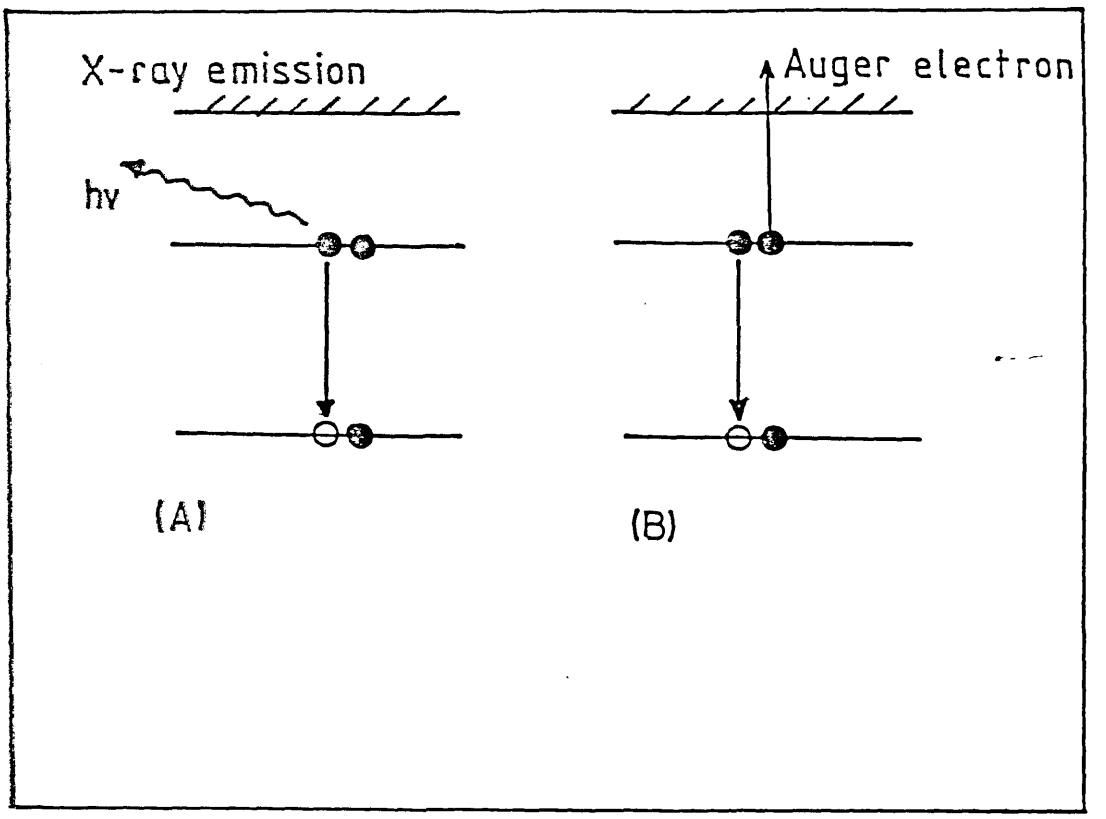


Figure 1.5 X-ray electron emission and Auger electron emission associated with core hole decay.

decay of the core hole or valence state has two mechanisms[11], Auger electron emission and X-ray emission. The Auger process involves the simultaneous emission of an electron into the vacuum and the decay of an electron into a hole (see figure 1.5), and X-ray emission the filling of the hole by an electron with the release of an X-ray photon. Although both processes occur simultaneously Auger decay is more probable for the lighter elements. There is a gradual switchover around atomic number 35 and for the heavier elements X-ray emission predominates.

Auger electrons can give rise to strong peaks in the XPS spectrum exemplified by the Mg:KLL excitation in the spectrum of AlKα excited MgO. The kinetic energy of Auger peaks is independent of the energy exciting radiation and the use of both Al:Kα and Mg:Kα X-rays is a standard technique for distinguishing Auger peaks from the XPS peaks which shift with incident photon energy.

1.2.5 Satellite structure in XPS

X-ray satellites

X-ray satellites[8] due to $K\alpha_3$ and $K\alpha_4$ components in Al and Mg X-ray radiation arise from 2p ⟶ 1s transitions in doubly ionized atoms. They produce a series of lines in experimental spectra of lower intensity that mirror the main peaks. These must be subtracted off the spectra using a suitable computer routine when they intefere with analysis. For example as shown in Chapter 5 Ba:$3d_{3/2}$ X-ray

satellites overlap with the Ba:$3d_{5/2}$ peak and use of the satellite subtraction routine was necessary to obtain an accurate peak area analysis.

Shake-up and shake-off

Shake-up transitions are a result of the synchronous excitation of a valence electron, accompanying the primary photoemission, to a level below the vacuum energy. The respective loss of energy of the primary photoelectron corresponds to the energy of the shake-up transition. In a solid metal unfilled one electron levels exist above the fermi level that are free electron like and are readily available for shake-up excitationss. The high DOS at the fermi level in metals manifests itself in characteristic asymmetric peak shapes. This is seen with Ba in Chapter 5 and Zr metal in Chapter 3 and the subsequent loss of the tail on oxidation.

Similarly shake-off transitions are the concomitant excitation of valence electrons above the vacuum level, but are usually not seen in the solid state because they do not give rise to discrete peaks.

1.2.6 Angular variation in XPS[11][9]

There are usually two reasons for changing the angle of emission from the normal:

(1) Angular XPS and surface sensitivity

By changing the angle of emission we modify the escape depth as shown in equation 1.2. A decrease of emission

angle leads to an increase in the intensity of the surface contribution to a spectrum with respect to the bulk. The sensitivity of XPS is thus improved as the surface enhancement allows the study of the particular properties of the surface, such as surface core shifts and overlayers. The major requirements are, however, surface flatness and cleanliness and typically only single crystal studies are feasible.

(2) Photo-electron diffraction[9]

When the angle of emission is changed whilst studying a specific XPS peak in a single crystal material, a fine structure due to the diffraction of photoelectrons from crystal planes can be seen. These XPD patterns have shown epitaxial growth of ZnSe on GaAs[19] and could possibly be used in further studies of BaO overlayers on MgO.

1.2.7 Quantification of XPS

X-rays can penetrate the sample to a depth of 10-20μm, and excite photoelectrons within that depth from core levels of all the elements present. The electrons then have to escape from the solid to pass into the analyser. First of all one can make the assumption that the attenuation comes from the inelastic scattering (the elastic scattering is weak) and is determined by the IMFP which is dependent on the electron energy. The intensity of the photoelectron flux ar ising from atoms of type A from a distance z beneath the surface is $I_A(z)$ where:

$$I_A(z) = o_A(h\nu)D(E_A) \int_{\gamma=0}^{\pi} \int_{\phi=0}^{2\pi} L_A(\gamma) \int_{y=-\infty}^{\infty}\int_{x=-\infty}^{\infty} J_o(xy)T(xy\gamma\phi F_A) \times N_A(xyz) \exp[-z/\lambda F_A \cos\theta] \, dx \, dy \, d\phi \, d\gamma \quad \ldots\ldots 1.7$$

Where: $o_A(h\nu)$ is the photoionisation cross-section for emission of a photo-eelctron from the relevant innner shell per atom of A by photon energy hν, $D(E_A)$ is the detection efficiency for each electron transmitted by the spectrometer, (xyz) is the coordinate system of the atom, θ is the angle between the emergent photoelectron direction and the outward normal, γ is the angle between the X-ray source and the analyser, $L_A(\gamma)$ is the angular asymmetry of

the photo-emission from each atom, $J_o(xy)$ is the X-ray flux, $T(xy\ \gamma\theta\ E_A)$ is the analyser transmission and $N_{A(xyz)}$ is the atom density of the atoms A at (xyz).

Theoretical estimates for cross-sections are available, but a major problem in using them for quantitative analysis is that the instrument functions D and T need to be established. Additionally, close to the threshold as for Mg:1s excited by Al:Kα radiation, the simplified theoretical procedure used to calculate cross-sections may be unreliable.

In the present work the major problem of quantification was one of determining the thickness of overlayers of BaO on MgO. Here we used elemental sensitivity factors determined from measurements on MgO and BaO in our own instrument. This procedure is to be preferred to using published tabulations of sensitivity factors because the various instrument functions in equation 1.7 may vary between spectrometers.

Background subtraction in XPS

Photoelectron peaks are usually situated on a complex background of inelastically scattered electrons with different levels at the high and low kinetic energy portions of the peak. Measuring the peak area is difficult because of the tail at low kinetic energy. The common methods are to subtract a straight line background joining sensible points in the spectrum measuring the peak area above the line or to use a nonlinear iterative background

subtraction as formulated by Shirley.[20]

1.3 LEED

1.3.1 Introduction

A monoenergetic, collimated beam of electrons incident on a clean, well ordered surface can be seen to give a diffraction pattern due to elastic scattering. The penetration of electrons of this energy (0-1kV veering on the low energy side if possible) is small suggesting suitability for surface study as the surface atoms mainly define the diffraction pattern[21].

Low Energy Electron Diffraction (LEED) in fact gives spot patterns that are fingerprint-like to the specific orientation of the crystal surface. Spot positions define dimensions of the 2D unit cell. The obvious use for testing of surface quality and cleanliness as a pre-amble to other studies is apparent. More refined application of the technique involves measurement of spot intensities as a function of beam energy. Analysis of data from these experiments enables one to make a full structural determination.

The electron waves experience the periodic structure of the crystal, and consideration of the de Broglie wavelength

$$\lambda = \frac{12.3}{E^{1/2}} \qquad \ldots. 1.8$$

(where E is the energy in eV)

suggests energies of 10eV or more (up to 1KV) for the beam to have comparability with lattice spacings. From

Bragg theory we obtain:

$$n\lambda = d\sin\theta \quad .... 1.9$$

Where: n is the order of diffraction spot

d is the inter-planar spacing on the surface

θ is the angle between the scattered beam and the surface normal

from which it is possible to deduce the Bravais lattice of the surface.

A plot of $E^{-1/2}$ versus sinθ can be used to obtain the lattice parameter d. The lattice spacing can be calculated from equations 1.8 and 1.9 with allowance for the geometry of the LEED apparatus and the magnification of the photographs of the phosphor screen.

1.3.2 Coherence Length[22]

An ideal beam of electrons used in LEED can be described by a plane wave having wavefunction at point r determined by the wave vector k as:

$$\Psi(r) = A \exp(ik.r) \quad .... 1.10$$

and accordingly an energy $h^2k^2/2m_e$. However, the direction and energy of the LEED beam are not perfectly defined and this results in an uncertainty in the phase of the wave. This phase relationship between different points on the surface becomes progressively less well defined with increasing lateral separation between the points.

One can define a coherence length as the maximum distance between two points on the surface where the phase relationship of the incident electron wave is preserved. Beyond this distance the phase relationship at the two points is arbitrary. If two domains on a surface are separated by a distance greater than the coherence length, the resulting diffraction pattern represents the sum of diffracted beam intensities from the two domains. By contrast if two domains fall within the same coherence area, the resultant diffracted intensity results from the addition of structure factors.

The coherence length for ΔF = 0.2eV with E = 150eV is about 500Å.

1.4 Energy loss Spectoscopy (ELS)

When a beam of mono-energetic electrons is incident on a crystal it is recognized that the emission consists of three different parts: (1) Elastically scattered electrons reflected without loss of energy (2) Inelastically scattered primary electrons with reduced energy (3) Electrons, with low velocities, which are produced from the target by collision processes. These are the so-called secondary electrons with an energy distribution depending on the density of empty electronic states above the vacuum level, and is not strongly dependent on the incident electron energy.

From energy conservation in ELS the energy of the inelastic primaries is given by:

$$E_S = E_I - \hbar\omega \quad \ldots\ldots 1.11$$

Where E^S is the reflected energy, E^I the incident energy and $\hbar\omega$ the excitation causing the energy loss.

The general form of the ELS spectrum from an insulator is shown in figure 1.6. A is the very intense primary peak due to elastically scattered electrons, B is the gap between A and the onset of the interband transitions at C. Phonon losses have energies of the order of 4-50 meV and are only seen if a monochromated electron beam is used to excite the spectrum. Interband electronic losses may occur within the band gap(B)due to surface electronic states.

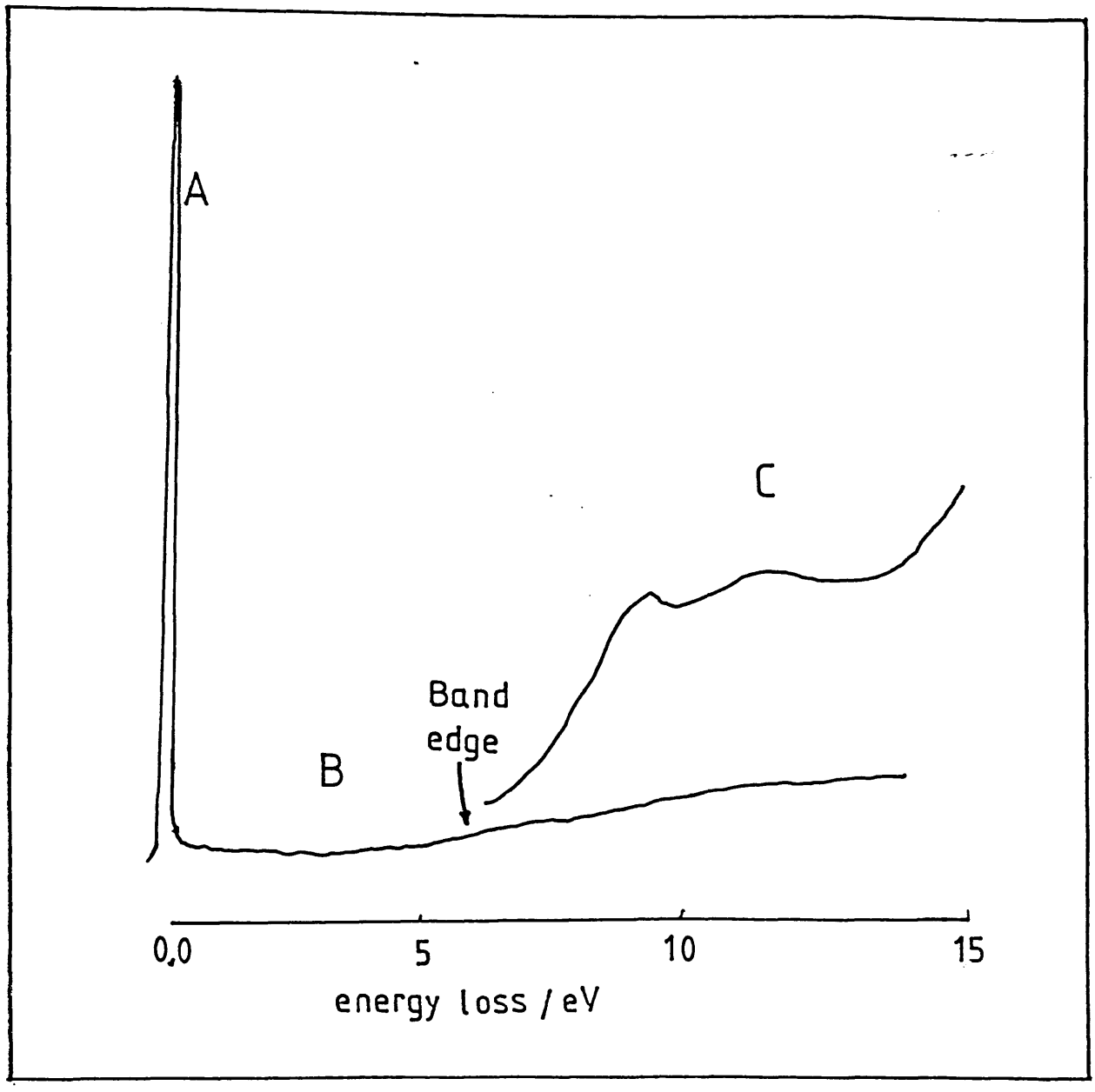


Figure 1.6 A typical ELS spectrum.

Thus polaronic and excitonic excitations are present in ELS spectra of chapters 3, 4 and 5. After the band edge, bulk and surface plasmon modes characteristic of the crystal can be excited.

Chapter 2. Experimental

2.1 Introduction

All electron spectroscopic and LEED experiments were performed in an ESCALAB MarkII spectrometer. (VG Scientific, East Grinstead, Sussex). The layout of the spectrometer is shown in figure 2.1 . The main body of the machine consists of two chambers, one for sample preparation and the other for analysis.

The analysis chamber is fitted with several of the techniques for surface analysis, based around an electron detection system consisting of a lens leading to a hemispherical analyser. In particular, electron spectra can be excited by X-ray or ultraviolet photon irradiation (XPS and UPS) and electron bombardment (ELS and Auger). There is also a quadrupole mass spectrometer which was only used for residual gas analysis.

The preparation chamber contains equipment for sample cleaning, including an ion gun and various arrangements for heating and annealing during experimentation. It has the LEED system situated on one end together with an xyz manipulator for aligning the sample with the LEED beam. It was also fitted with a shrouded getter source for the deposition of barium onto the surface of MgO described in chapters 5 and 6.

A fast entry lock is attached to the preparation chamber via a gate valve and is used for introduction of samples without breaking ultra-high-vacuum (UHV) conditions ($< 10^{-10}$ torr). The preparation and analyser

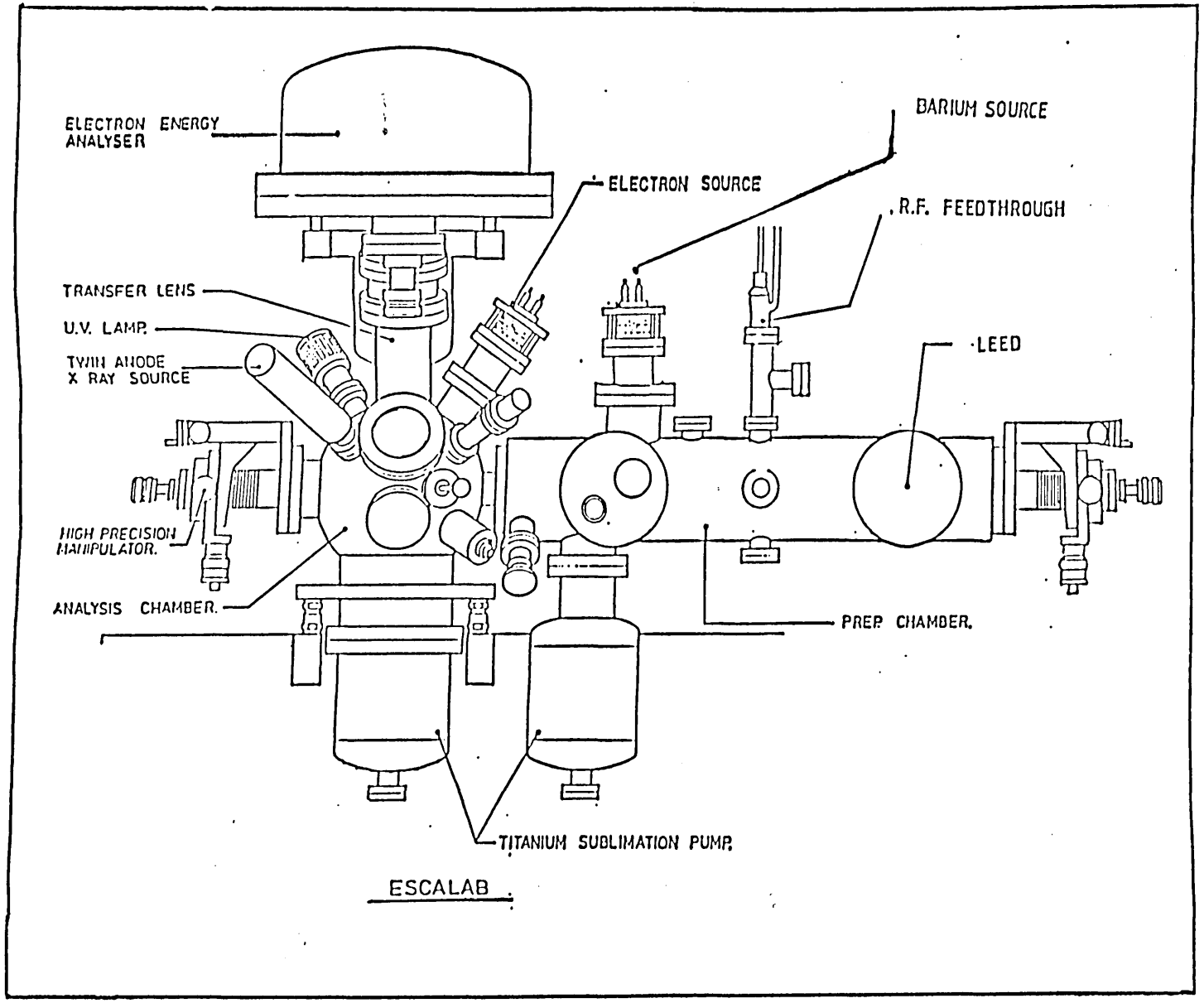


Fig 2.1 The VG ESCALAB

chambers are separated by a gate valve to allow an individual chamber to be isolated from the other.

2.2 The pumping system

The bulk of the spectrometer is made from stainless steel which has the favourable properties of low outgassing rates and the ability to sustain repeated bakeouts at temperatures of about 150 °C. To provide magnetic shielding the analysis chamber and analyser system are constructed of mu-metal. Flange connections sealed with stainless steel knife edges biting into copper gaskets are used throughout the system, apart from the large flange on the analyser dome which has a softened copper-wire seal. The vacuum seals on the gate-valves are based on viton o-rings as is the seal on the fast entry lock.

Each of the main chambers is pumped separately by means of an Edwards E04 diffusion pump, charged with polyphenyl ether pumping fluid, and a titanium sublimation pump. The diffusion pumps are both trapped by CCT100 liquid nitrogen cold traps and are backed separately by Edwards rotary vacuum pumps.

A small ion pump is incorporated in the system to pump the X-ray gun when in use, allowing outgassing of this assembly without a large increase of pressure in the analyser chamber. The nitrogen traps prevent back diffusion of pump oil, as well as providing rapid pumping for condensible vapours. Thus, if the nitrogen is allowed to boil off, the diffusion pumps should be closed and the

system pumped with the ion pump. To achieve pumpdown from ambient pressures the following procedure is adopted: a rotary roughing pump reduces the pressure to around 10^{-2} torr, the diffusion pumps are then opened in series with their respective backing pumps and the roughing line is isolated. If the UHV system is clean, pressures of around 10^{-9} torr may be achieved by judicious use of the titanium sublimation pumps, but after breaking the UHV it is usually necessary to bake the system to obtain pressures below 10^{-9} torr. The bakeout procedure involves about nine hours baking at 150°C; followed by cooling, filling the nitrogen traps and outgassing gun filaments (whilst the spectrometer is still warm) for a further three hours. The spectrometer will come to room temperature after twenty four hours, so the whole process of machine preparation takes about one and a half days.

2.3 Sample manipulation

Samples are mounted on small male stubs which fit into female holders in appropriate positions around the spectrometer. A locking device on the female xyz manipulators enables one to rotate the sample to obtain the correct orientation for the specific technique in question. There is a small 'railway line' separating the preparation and analysis chambers operated by a linear rotary drive. Wobble sticks are present in both chambers for lifting samples on and off the carrier.

Carefully balanced mounting is usually needed as transference via the wobble sticks is by no means facile.

There is also a linear drive between the fast entry lock and the preparation chamber used for transfer of samples to and from the spectrometer.

2.4 The gas line and gas dosing

The gas line allows controlled gas admission via leak valves to both of the main chambers and the fast entry lock. All gases were of nominally high purity. Their purity was checked with the quadrupole mass spectrometer before experiments began.

2.5 Introducing a new sample

The fast entry lock is carefully filled with dry nitrogen or argon up to room pressure. The use of these gases prevents water vapour getting into the fast entry lock which increases subsequent pumpdown time. The sample is then placed on a carousel and after roughing the fast entry lock for about 30 mins (10^{-2} torr) the sample is then quickly transferred to the preparation chamber after the roughing line has been isolated.

2.6 Radiation sources

2.6.1 X-ray source

The twin anode X-ray source shown in figure 2.2 is based on a water-cooled copper cylinder terminating in a V-shaped endpiece. One side of the `V` is coated with aluminium and the other with magnesium. Independently heated filaments are placed on either side of the anode, allowing the production of two X-ray lines, one at 1253.6 eV due to MgKα radiation and the other at 1486.6 eV due to AlKα, from the same power source.

The source was typically run with a potential of 10 KeV between the filament and the anode, with a 20mA emission current. Due to the large current needed, a lot of heat was generated and attention to adequate water cooling was always necessary. Careful outgassing at various stages up to maximum gun power was also necessary when the machine had been let up to air. However with the small ion pump switched on, the gun could be run at base pressures lower than 10^{-10}torr. There were also some problems with impurity radiation which are discussed in the next section.

2.6.2 Impurity radiation in XPS

Three different impurity radiations were encountered in the X-ray source:

(1) CuLα

Due to loss of aluminium and magnesium metal from the anodes after prolonged use the underlying copper metal can

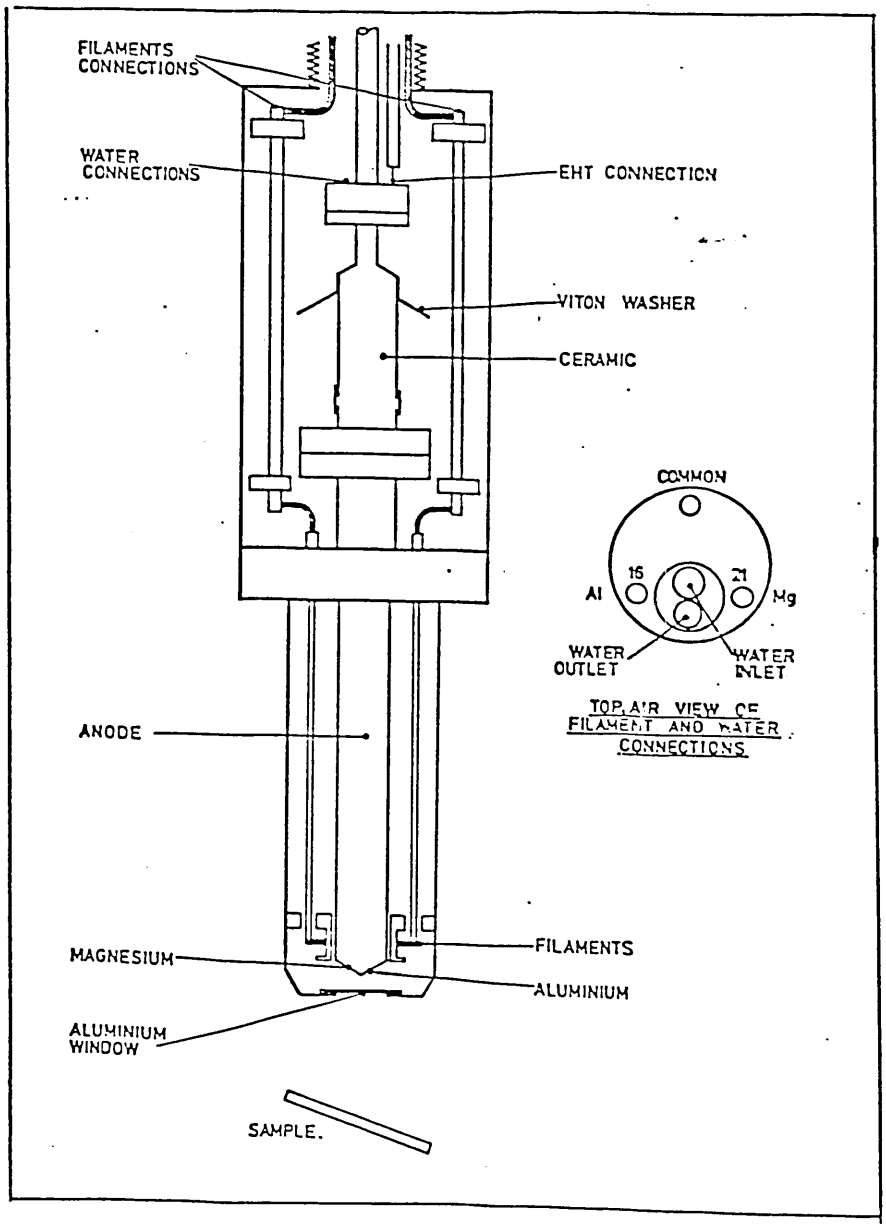


Fig 2.2 The X-ray source

become exposed resulting in CuLα radiation (hv = 929.7eV), identified by the fact that it gives a shadow of each photoelectron peak at 324eV higher binding energy of Mg Kα peaks as in figure 2.3(b).

(2) Mg/Al crossover

Due to misalignment of the filament, or crossover of anode coatings, stray electrons can hit the Mg anode under Al Kα operation. Some spurious peaks in the AlKα spectra were thus attributable to MgKα radiation as can be seen for example in figure 2.3(b).

Note also that some AlKα radiation is always present when using the magnesium source. This arises in part from the thin aluminium window separating the anode from the spectrometer chamber. Together with high energy background Bremsstrahlung radiation, this allows excitation of Mg:1s core-hole states when using the magnesium anode and the unexpected appearance of the Mg:KLL Auger peak (which is very strong) in MgKα excited spectra of MgO (chapter 4).

(3) OKα

As a result of oxidation of the magnesium anode excitation of OKα radiation (hv = 524.9 eV) was possible. Due to this radiation, shadow peaks at 728eV higher binding energy, could be found in the spectrum as in figure 2.4. This radiation proved to be of positive value as a soft X-ray source and was used in the XPS studies of YSCZ (chapter 3).

All the above features were due to anode degradation,

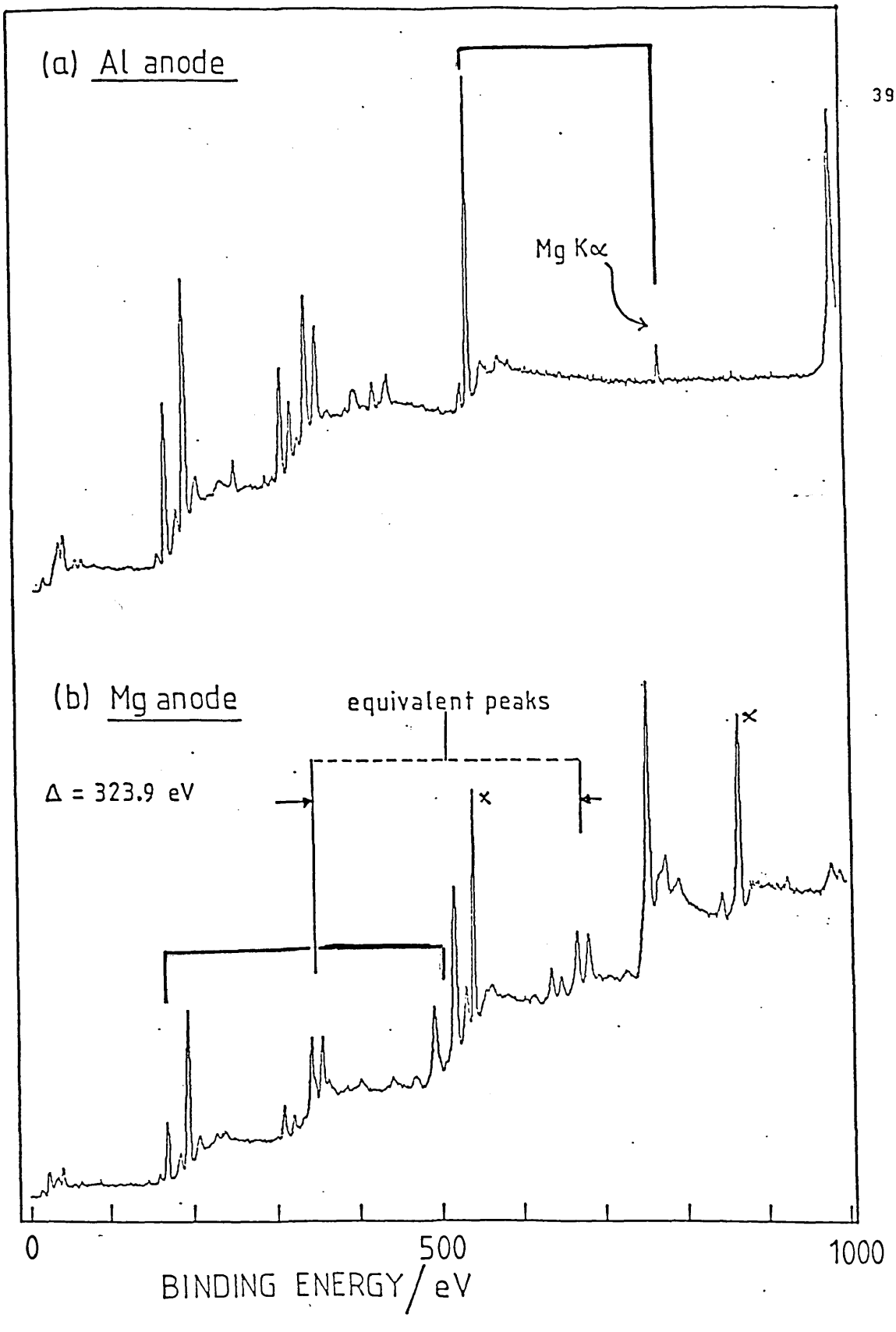


Fig 2.3 (a) AlKα spectra of YSCZ showing MgKα crossover

Fig 2.3 (b) CuLα impurity radiation in the MgKα spectrum of YSCZ. Note the shadow peaks at 324 eV higher binding energy.

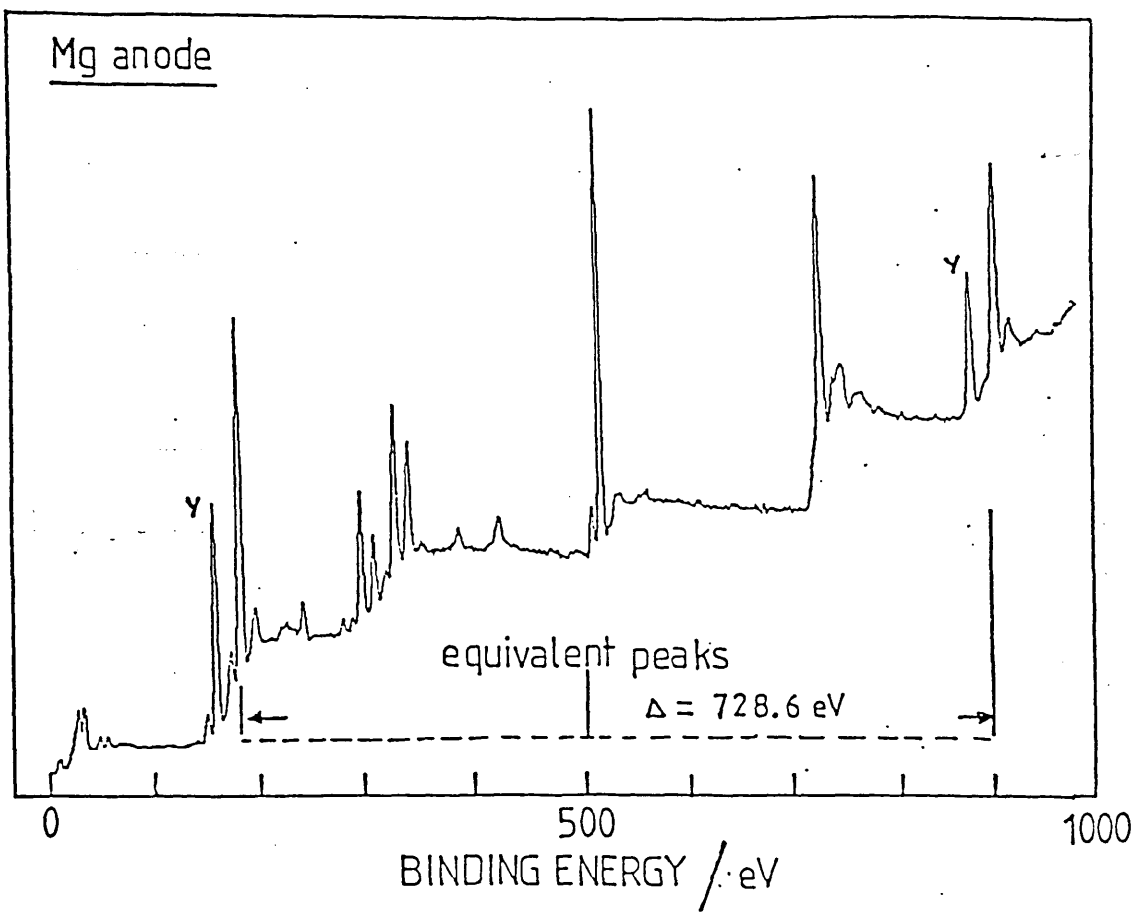


Fig 2.4 OKα impurity radiation in the MgKα spectrum of YSCZ. Note the shadow peaks at 728 eV higher binding energy.

and proved most problematic with older anodes. However a new anode was used for most of the work in this thesis.

2.6.3 The ELS electron source

Figure 2.5 shows the LEG31 electron source. The electrons are produced by thermionic emission from a tantalum/barium hairpin filament. Three electrostatic lenses are employed which determine the focusing and spot size of the beam. X and Y plates at the end of the gun allow directional variation within the spectrometer. Single crystal MgO(100) and YSCZ are fluorescent under electron bombardment. Therefore optimization of sample position and beam profile (which is by no means facile for the ELS technique) was made easier by first turning to high currents (100μA) and then back down to normal currents (1μA) when aligned.

2.7 The analyser and lens system

The path of the photoelectrons produced in XPS and those reflected in ELS is shown in figure 2.6. Electrons emitted or scattered in XPS and ELS first pass through an electrostatic lens (a mu-metal shielded double Einzel lens) and are retarded by an amount -R before entering the analyser through narrow slits. The 150° spherical sector analyser acts as a narrow pass filter letting through only electrons with an energy HV known as the pass energy, where V is the potential difference between the

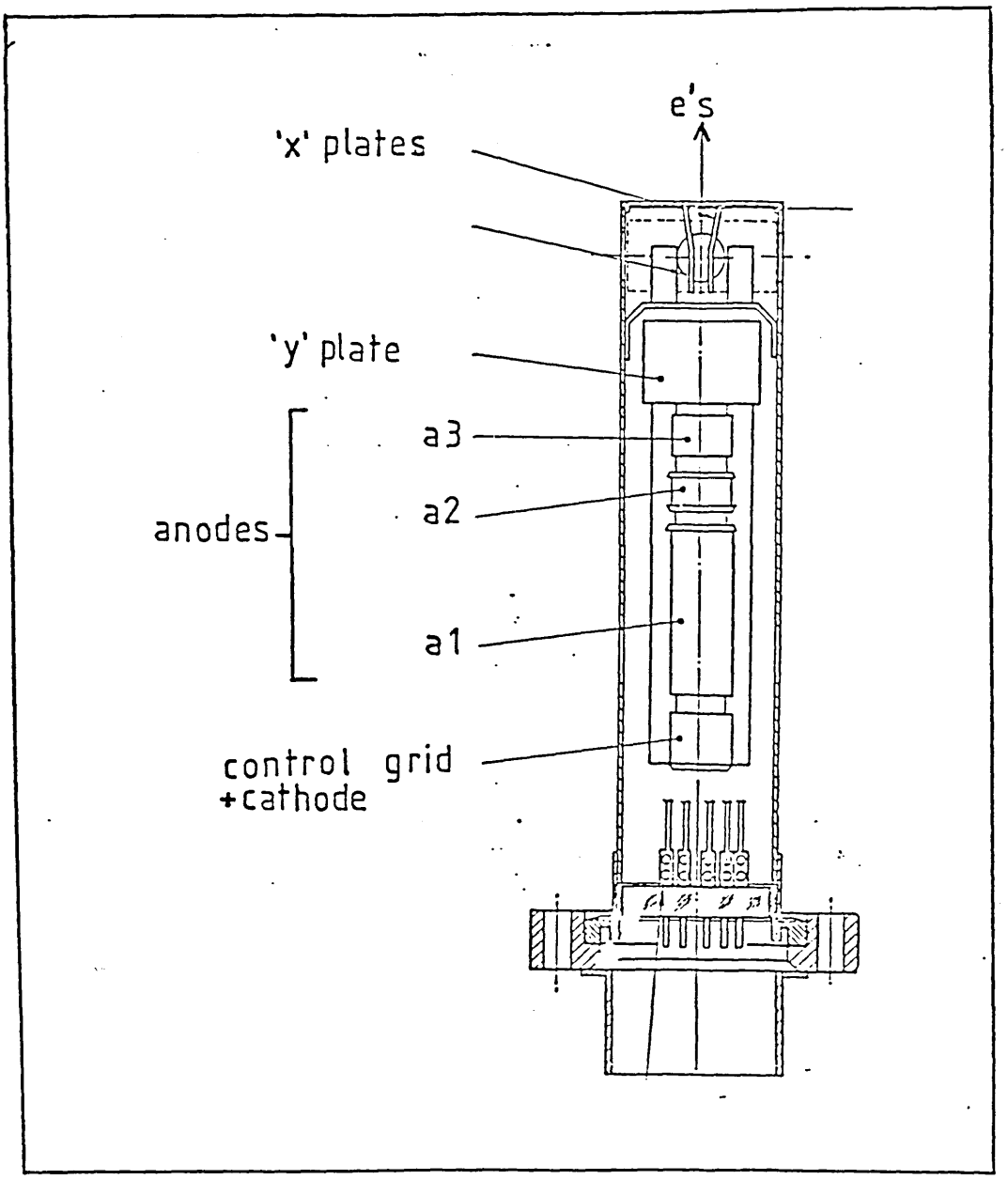


Fig 2.5 The LEG31 electron gun used for ELS

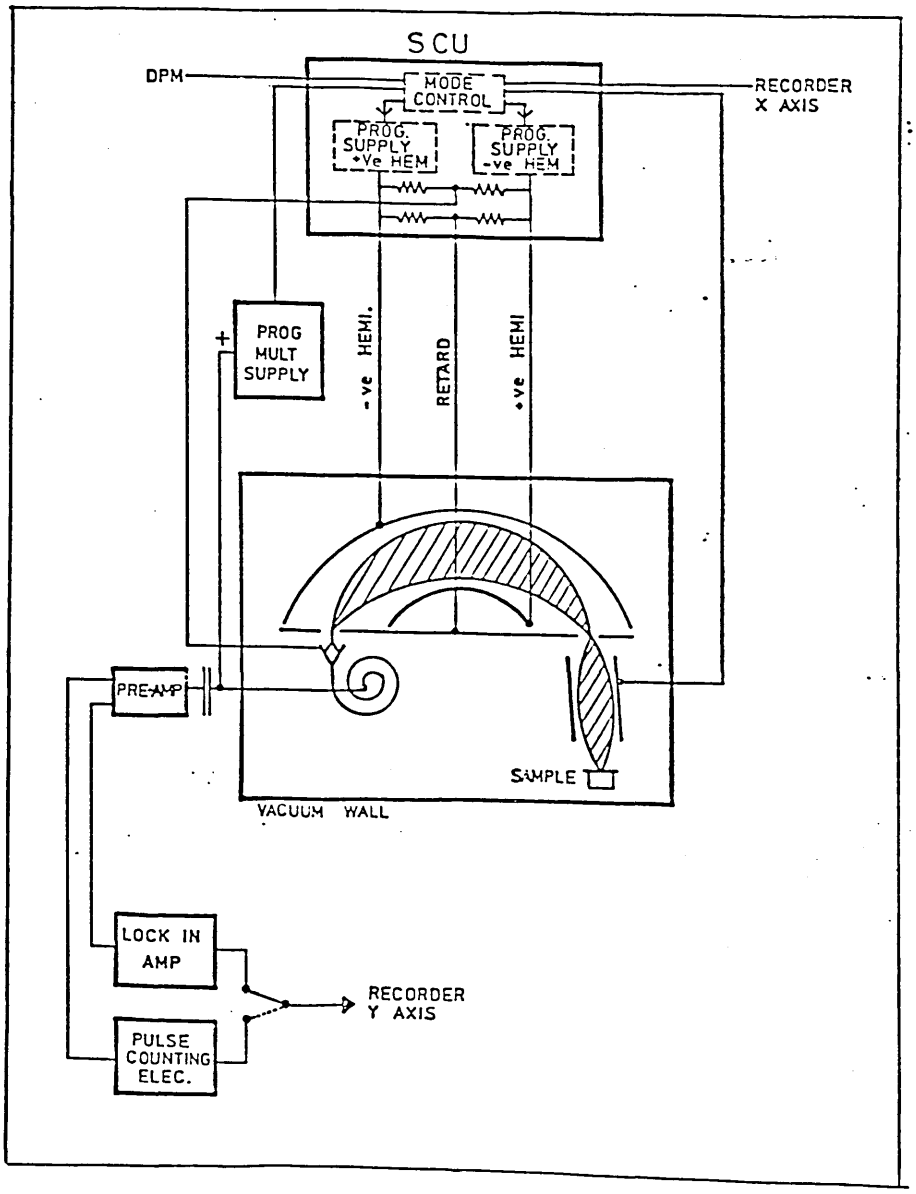


Figure 2.6 Schematic showing the path of photoelectrons in the vacuum and also the subsequent counting electronics.

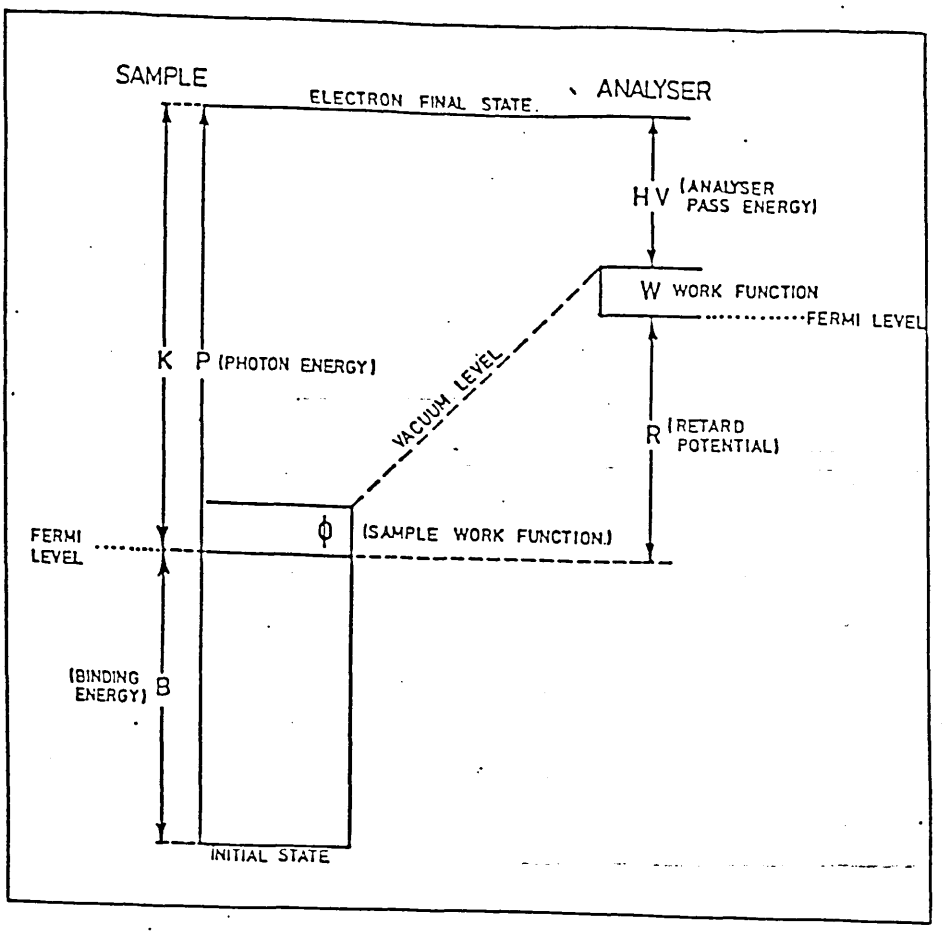


Fig 2.7 Energy level schematic (XPS)

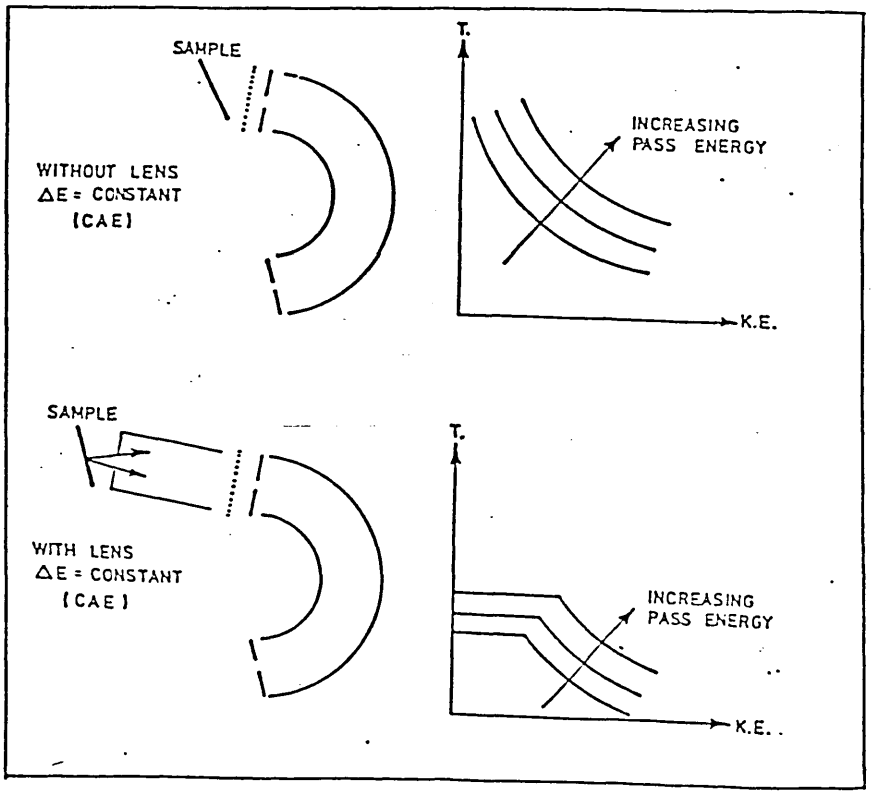


Fig 2.8 Analyser transmission characteristics for CAE

inner and outer hemispheres and H is a constant of the analyser. The sample is usually grounded and the retarding potential -R is, in effect, the electrical centre point of the analyser as shown in figure 2.7.

A kinetic energy K, of the emerging electrons can therefore be equated to :

$$K = R + HV + W \quad \ldots\ldots \quad 2.1$$

Where W is the work function of the spectrometer.

2.7.1 The effect of pass energy and analyser slit width on analyser resolution

It can be shown that the following relationship holds :

$$\frac{\Delta E}{HV} = \frac{\Delta r}{2r} + \alpha^2 \quad \ldots\ldots \quad 2.2$$

Where :

HV is the pass energy

ΔE is the contribution to the full width at half height of a recorded peak

α is the half angle of admission in the plane of electrons

r is the mean radius of the hemispheres

Δr is the slit width of the analyser

The contribution to broadening of α^2 is usually small and the smaller the contribution from the HV or Δr terms, the better the spectrometer resolution. The inlet and exit

slits of the analyser can be changed by operating a rotary drive coupled to a slit plate under the analyser housing. Two sets of slits were used in this work; C1 for XPS and C3 for ELS. The dimensions are shown below.

Type	Inlet / mm	Exit / mm
C1	15 x 6	15 x 6
C3	15 x 1.5	15 x 1.5

It was necessary in ELS to use C1 first, in order to obtain the primary elastic beam, and then to turn to C3. The area on the surface from which electrons enter the analyser is conjugate with the analyser entrance slit. Hence another advantage of the smaller slit width setting is that it reduces the sample area being investigated making it easier to eradicate stray photoelectrons from the sample mount.

2.7.2 Modes of Analyser operation

The analyser can be operated in two modes:

(a) Constant analyser energy CAE

In this mode the analyser pass energy is constant and the retard voltage is ramped to allow electrons of different kinetic energy to enter the analyser. The lens potential is also ramped to maintain the focus. Therefore

there is a fixed resolution at all kinetic energies, the magnitude of which is set by the pass energy. See figure 2.9 for nominal transmission characteristics in this mode.

For techniques which need especially good resolution a relatively high pass energy is used at first to optimize the signal, and then a lower one is selected to record spectra with improved resolution. Changing the pass energy to a lower value, however, lowers the photoelectron count rate. Optimum peak definition is usually a balance between lowering the pass energy and having a reasonable count rate.

The CAE mode was used throughout this work.

(b) Constant retard ratio CRR

In this mode the ratio of the kinetic energy to the pass energy is constant ie :

$$RR = \frac{K - W}{HV} \qquad \ldots\ldots 2.3$$

The lens voltage and the pass energy are all swept during the scan. In this mode the pass energy decreases with electron kinetic energy and thus resolution improves as we scan to lower kinetic energy. Moreover, sensitivity decreases across a scan and this mode is useful for the suppression of the strong background of inelastically scattered electrons at low energy, as needed in electron beam excited Auger spectroscopy.

2.8 Electron counting

Figure 2.9 shows a schematic of the electron counting apparatus. The small photoelectron current of about 10^{-14}A reaching the analyser slits is too small to be measured by conventional methods and therefore pulse counting electronics are used here.

The electrons are detected by a channeltron which is a high gain device consisting of a lead impregnated glass tube of conical bore coiled into a spiral. A high voltage of around +3KV is applied to one end of the spiral with the other end held close to earth potential. When an electron hits the inside wall of the channeltron it causes an avalanche of secondary electrons down the spiral which, in turn, are accelerated down the potential gradient. The gain in signal is about 10^{+7}, producing charge pulses of the order of 0.1 pC in 10nsec.

Raw pulses from the channeltron pass first through a preamplifier mounted on the spectrometer which amplifies and also decouples the signal from the high potential on the channeltron. The pulse is then shaped, filtered and further amplified to produce voltage pulses with 5V amplitude and 500nsec width. These can be counted directly by an Apple II microcomputer or fed into a ratemeter to produce an anologue signal that can be output to an X-Y recorder.

Repeated scans will improve signal to noise such that :

$$\frac{S}{N} \propto n^{1/2} \qquad \ldots\ 2.4$$

Where S is the signal, N the noise and n the number of scans.

2.9 Data storage and manipulation

VG hardware and software were used for data handling with spectra being stored on magnetic floppy discs. The various aspects of background subtraction, satellite subtraction, expansions in the X or Y directions and peak integration are well documented in VG manuals.

2.10 The LEED gun and grid system

2.10.1 The LEED system

The preparation chamber is fitted with a 120 degrees, three grid LEED system (see figure 2.1).
Sample alignment was achieved by careful stub mounting and positioning of the xyz manipulator. LEED spots from MgO(100) are very sharp and were used to check that the subtended angle of the grids was in agreement with its nominal value when the sample was at its normal position, and that the grid system was well aligned.

The thoriated tungsten hairpin filament and the focussing lenses of the electron gun are not dissimilar from

those used in ELS. Beam energies could be varied from 0 to 1.2 KV, but best surface sensitivity is found for lower beam energies. The beam is usually about 0.1 cm in diameter (at 100eV), stable to about 0.1μA at 10 μA gun current, and is parallel to within about one degree. Energy distributions in the beam are broadened by ± 0.15 eV due to thermal spread of the electrons emerging from the hot cathode. For insulating samples there is a sudden extinction of LEED patterns at a lower critical beam energy determined by sample charging. This energy is determined by the energy at which the coefficient of secondary electron emission falls below unity.

In the Imperial college ESCALAB there is a specific problem with the outgassing of the bellows of the xyz manipulator which positions the sample in front of the LEED screen. A number of hours of careful heating is needed for outgassing the bellows after the instrument has been let up to air before experimentation commences. This is a design fault with the spectrometer resulting from inadequate bakeout of the LEED manipulator.

2.10.2 LEED detection

LEED patterns were photographed with a Pentax ME Super camera mounted on the preparation chamber LEED viewing port. Photographs were catalogued with the aid of a data back. Aperture size and exposure time were optimized for intensity and the sharpness of spots. ASA 400 black and white film was used throughout. The diffraction angles of

spots were easily calculated from photographs by reference to the diameter on the photograph of the LEED screen.

2.11 Internal sample preparation

2.11.1 Crystal annealing and heating

Three techniques of surface annealing / heating were used :

(1) Resistive heating

A commercially available P8 probe in the sample preparation chamber is fitted with a resistive heater capable of maximum temperatures of about 600°C, giving a sample temperature of at most 500°C. This temperature was generally inadequate for annealing oxide surfaces in the present work.

(2) Electron bombardment

Electrons emitted from a heated tungsten hairpin filament can be used to bombard the sample, provided a high potential is maintained between the sample and the filament. Typical emission currents of 25mA at approximately 2KeV give temperatures in excess of 1000°C. Electron bombardment has the advantage of being able to ' flash ' the crystal up to high temperatures very quickly but has a number of disadvantages :

(i) It is very hard to shield the chamber wall from stray electrons even when the filament is enshrouded by a tantalum tube and the sample held at positive potentials. The gases subsequently desorbed from the walls can adsorb

on the sample causing impurity problems.

(ii) The positioning of the filament, relative to the sample, is not facile and together with stub mounting makes it difficult to obtain reproducible heating.

(iii) The filament may evaporate metal onto the sample.

(iv) For oxides of lower thermal conductivity " spot heating " occurs which can result in fracturing of the crystal.

(v) The electrons can reduce the sample. This actually formed the basis of some experiments on YSCZ.

Electron bombardment is more useful for high temperature annealing of metal crystals where temperatures in excess of 2500°C are needed.

(3) Radio frequency (RF) heating

This method of heating proved the most useful for annealing crystals in this work. (See figure 2.11)

The ESCALAB was fitted with a coaxial RF feedthrough, see figure 2.11, supplied by Leybold Heraeus Ltd. On the UHV side there is a water cooled copper work coil, dimensioned to allow for the insertion of a stub and sample via a z shift feedthrough (see figures 2.11 and 2.12). The samples are insulated from the feedthrough on which they sit by means of a carefully machined piece of high temperature ceramic thus minimizing any loss of heat by conduction. The copper work coil is coupled to a Radyne 1.5kW, 500KHz generator .Water cooling of the coil was necessary, because of radiative heating of the coil as the

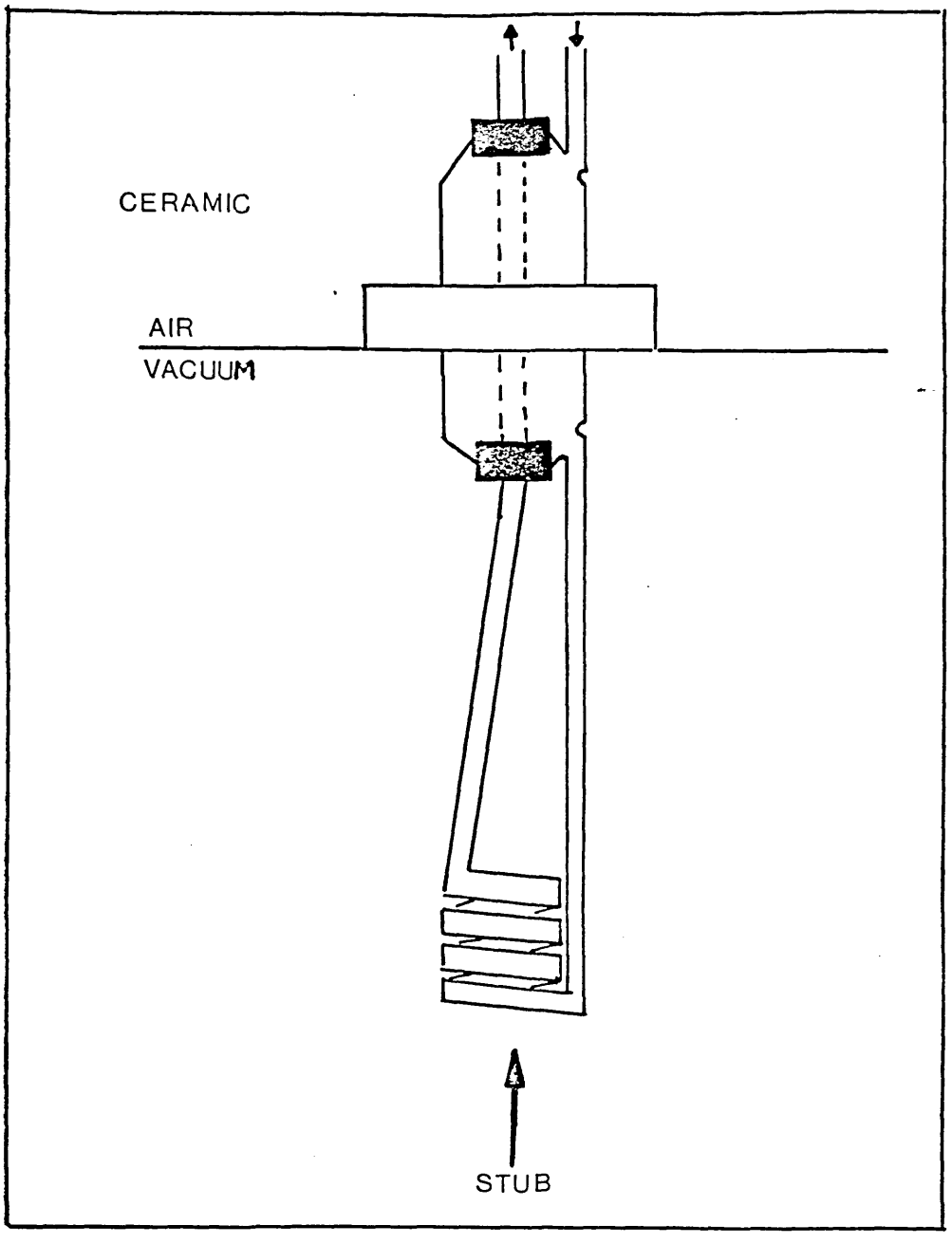


Figure 2.9 A schematic of the RF feedthrough

sample temperature was increased.

Heating is very dependent on the coupling of the sample with the RF power as with most induction techniques. For this reason samples were placed on tantalum foil which was spot welded to molybdenum stubs, both of which couple nicely. Temperatures up to 1500°C were easily achieved although not always needed. YSCZ is an ionic conductor at high temperatures and can itself couple with the RF power directly. However heating, via the tantalum foil, is necessary at first to initiate coupling. Sample temperatures were estimated using an optical pyrometer viewing through port as in the photograph in figure 2.12.

An advantage of RF heating is that it can be used to anneal samples in an appreciable pressure of oxygen. This option was needed at some stages in YSCZ annealing.

A word of warning about RF power. It disturbs all electrical appliances including radios, ratemeters, oscilloscopes, telephones etc. even up to tens of metres away. It is also quite dangerous and the external copper feedthroughs should be carefully insulated and all experiments performed with due care.

2.11.2 Argon etching

The preparation chamber is fitted with a Penning-type AG 2 argon ion source used for sputtering off surface layers and contaminants. It was usually operated at 10^{-6} torr of argon and at 2.5 KV for a number of minutes. The samples gave off a blue fluorescence when hit by the

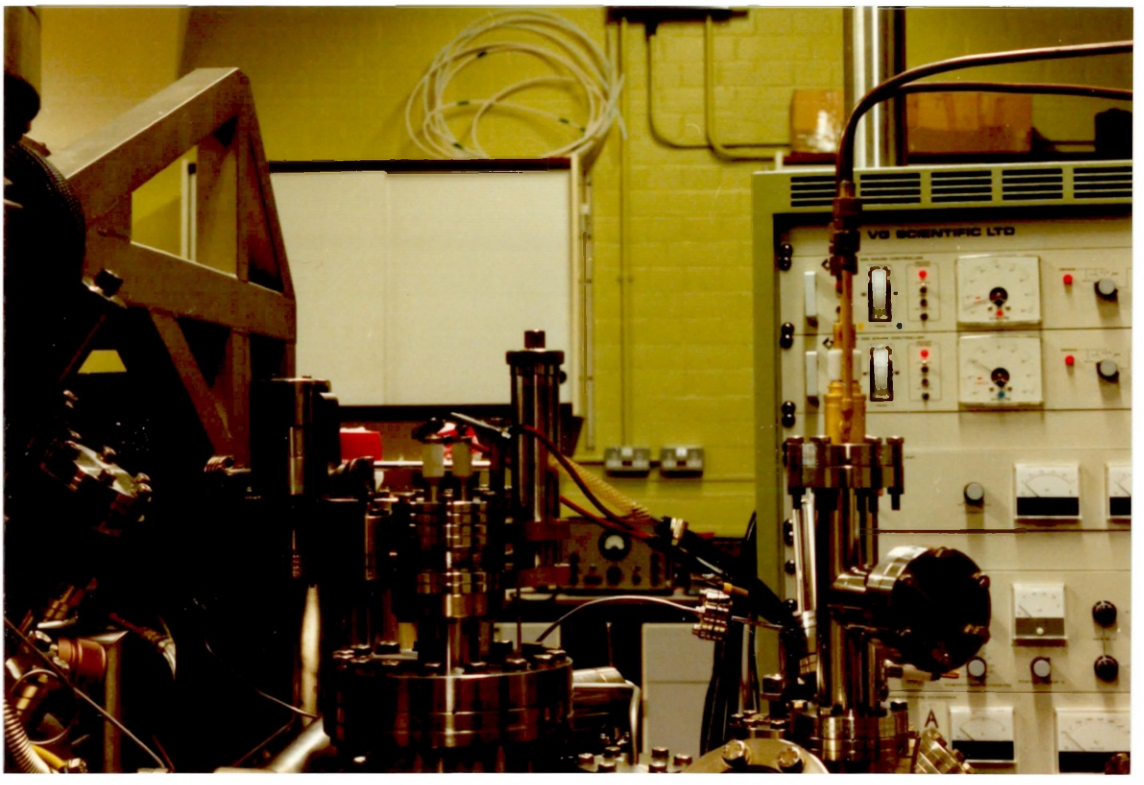


Figure 2.10 Photograph of the RF feedthrough on the ESCALAB

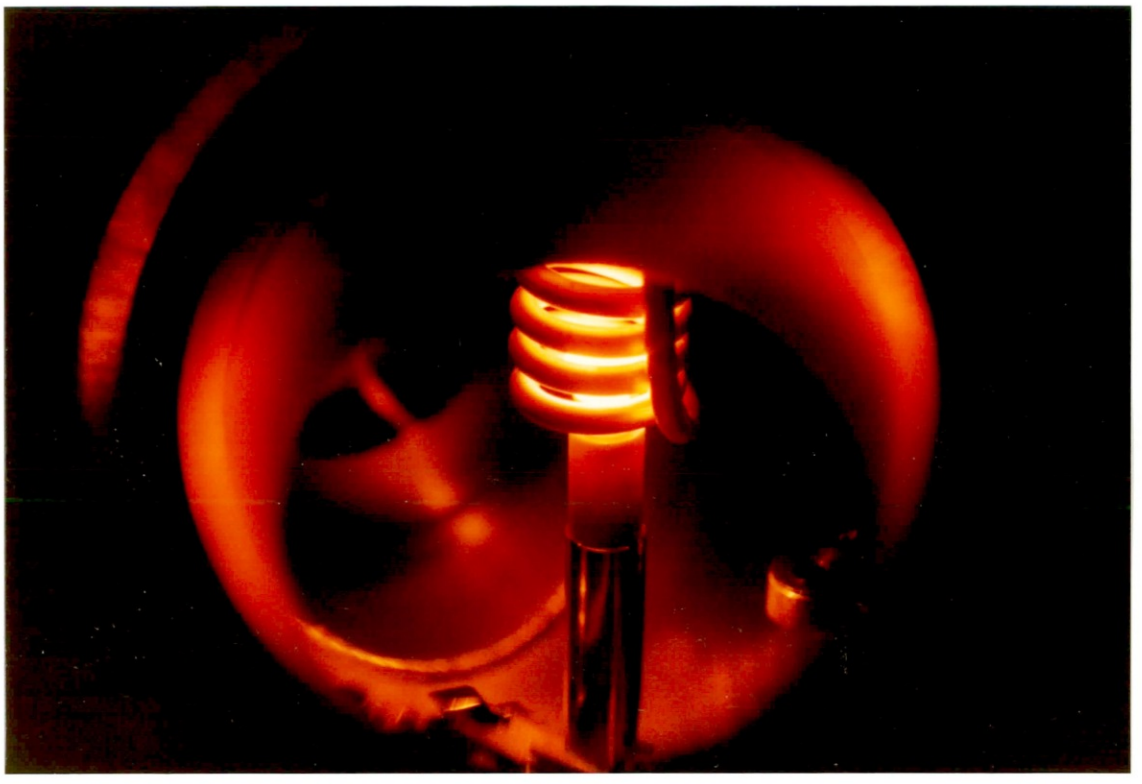


Figure 2.11 Photograph of YSCZ being heated to white heat within the RF coil

argon ion beam.

For insulators, the induced sample current cannot be measured directly, but general experience with similar ion guns suggests typical ion fluxes would have been of the order 10-20μA / cm^2.

Chapter 3. Electron Spectroscopy of Yttrium stabilised Cubic Zirconia (YSCZ)

3.1 Introduction

ZrO_2 adopts a low-symmetry monoclinic structure based on 7-coordinate Zr^{4+} at room temperature, but undergoes a phase change to a tetragonal form at 1000°C. A cubic fluorite phase can be stabilized at room temperature by the addition of large cations such as Y^{3+}, Gd^{3+}, Sc^{3+} or Sm^{3+}. Stubican et al[1] and Duwez et al[2] have shown that the cubic phase $(ZrO_2)_{1-m}(Y_2O_3)_m$ is stable when the mole fraction m is between 0.07 and 0.45, and that the lattice parameter can be varied from 5.14Å (m = 0.09) to 5.23Å (m = 0.40).

YSCZ is a high temperature ceramic with a number of potentially useful technological properties. The cubic form has high mechanical toughness for a ceramic, and even better mechanical properties are obtained with material close to the cubic/tetragonal phase boundary[3] which is intimately dependent on a grain structure incorporating both cubic and lower symmetry crystallites. Because of its hardness and also its high refractive index, YSCZ is also used in the jewelery trade.

Incorporation of Y_2O_3 leads to oxygen ion vacancies and the high resulting oxygen ion conductivity makes it potentially useful as an electrolyte in electrochemical sensors[4], high temperature fuel cells and oxygen seperation membranes. The parameters which determine the usefulness of oxides in such devices are the oxygen self-diffusion coefficient, which determines the rate of mass

transport in the material, and the surface exchange coefficient which determines the kinetics of exchange between lattice oxygen and oxygen in the gas phase. YSCZ is known to have a high self-diffusion coefficient but slow surface kinetics at low temperatures (< 500°C, unfortunately the ideal temperature range) and considerable effort has been devoted to improvement of surface exchange rates by suitable surface pretreatments[5]. In quite a different context YSCZ (100) has been suggested as an optimal substrate[6] for epitaxial growth of silicon on insulator layers, the lattice match (which can be tuned by varying the stoichiometry) being much better than with the more conventional Al_2O_3 substrates.

In assessing the mechanical properties, kinetics of phase transformations and electrical conduction of YSCZ due consideration must be given to Y^{3+} segregation to grain boundaries. Winnbust et al[7] studying the polycrystalline system $(ZrO_2)_{1-m}(Y_2O_3)_m$, { m = 0.14 to 0.21 }, show that grain boundary enrichment with Y^{3+} was observed using derivative mode AES. They concluded that the difference in activation energy of the ionic conductivity at the grain boundary, compared with that of the bulk, is due to this observed enrichment. They also noted a decrease of the yttrium signal in AES and ELS as a function of argon ion sputtering time, which indicates segregation. Solomon et al[8] working on single crystal YSCZ quantified the concentration of Y^{3+} at the surface using EELS and AES

showing that the atom ratio Y/Zr in the bulk is smaller than at the surface, also indicating segregation.

In order to study segregation in this work, normal and grazing emission XPS (indeed as Solomon[8] suggests) and light argon ion etching have been used. Comparisons of observed stoichiometries with bulk X-ray values showed segregation extending over a length range that is large compared with the XPS pathlengths. Also reported in this chapter is the striking feature that electron bombardment leads to selective reduction of host Zr(IV) to Zr(0) without comco mitant reduction of the Y(III) dopant until all the Zr(IV) has been reduced.

The shake-up satellites of the 3d peaks of Y^{3+} and Zr^{4+} in YSCZ, ZrO_2 and Y_2O_3 are also of interest and are therefore reported and analysed. Comparison of the satellite energies suggests that the mechanism involves polarization of ligand electron density induced by the core hole formed during photoionisation. ELS studies have been useful as a qualitative tool in the reduction of YSCZ and in the analysis of shake-up phenomena.

3.2 Sample preparation

3.2.1 External

YSCZ

The two YSCZ crystals with (100) orientation were obtained from Ceres Inc. USA and have the general

stoichiometry ($ZrO_2)_{1-m}(Y_2O_3)_m$ m = 0.09 and 0.16, giving 'x' values in $Zr_{1-2x}Y_{2x}O_{2-x}$ of 0.14 for m = 0.16 and 0.083 for m = 0.09.

Stoichiometry of the m = 0.16 crystal was confirmed by accurate determination of the lattice parameter from a small chip of crystal ($0.1mm^3$) on a Nicolet R3M four circle single crystal x-ray diffractometer using CuKα radiation. Lattice parameter measurements were made with sixteen independent reflections with 2θ between 94° and 102°. The value of m (and x) was worked out from a plot of m versus the lattice parameter characterising the YSCZ system. The lattice parameter from the bulk analysis above was 5.196Å which proved to be 16% YSCZ as the distributers suggested. The 9% crystal was therefore also taken to have the appropriate stoichiometry. We are grateful to Dr.D.J.Williams for the X-ray measurement.

YSCZ does not cleave easily and was therefore polished with successively finer diamond paste down to 1μ. The mirror finished crystals were annealed at 1360°C for 48 hours to burn off any residue from polishing.

Both the crystals have the fluorite structure and are oriented in the (100) plane which was checked with Laue back reflection prior to experimentation and was accurate to within one degree. The crystals were then individually mounted on tantalum foil spot welded to a molybdenum stub, cleaned in isopropanol in an ultra-sonic bath and introduced into the spectrometer.

Powders

The Y_2O_3 and ZrO_2 powders (Johnson Matthey LtD) were of specpure grade (99.999% Y_2O_3 , 99.99% ZrO_2). Each sample was pressed into 13mm pellet form, mounted on tantalum foil spot welded to a molybdenum stub and introduced into the spectrometer.

Zirconium foil

Zirconium foil (Goodfellows, 99.99% pure) (1X1X0.1 cm^3) was polished down to 1μ and mounted similarly to the powders after washing in isopropanol in an ultrasonic bath.

3.2.2 Internal

The four heating and annealing methods discussed in chapter 2 were all applied to YSCZ (100) and compared for cleanliness of the surface and for ordering in the surface layers. Thermal heating the crystal on the ESCALAB P8 probe was found to be inadequate in itself for removing surface carbon and very slow at re-annealing the surface after a light argon etch. No LEED patterns could be observed with P8 heating only. Electron bombardment (2.0KeV with 5mA target current) was used to flash the crystals up to white heat but this reduced, and disrupted the surface, and no LEED patterns could be observed. RF heating was the method most frequently used, apart from in the reduction experiments, as it did not reduce the crystal if carried out in oxygen. Even without oxygen, a LEED pattern was still seen after RF heating. A special advantage of RF

heating in its application to YSCZ was that the tantalum foil thermally heated the crystal to temperatures where oxygen ion mobility was possible, and therefore the crystal coupled itself to the RF power making annealing easier. Temperatures in excess of 1200°C were easily obtainable in a matter of seconds. The photograph in figure 2.11 shows the technique in action with a base pressure in the low 10^{-9} torr region, emphasising the in situ compatability of RF heating.

The ZrO_2 and Y_2O_3 powders could be heated by electron bombardment of the underlying Ta foil as they are nonconducting and did not reduce. This method proved very satisfactory for outgassing and cleaning after argon bombardment.

The Zr foil was argon bombarded then electron bombarded until free from carbon contaminants.Oxygen contamination remained after this treatment. However since we were interested in subsequent oxidation of the foil no concerted effort was made to remove the oxygen contamination.

3.3 LEED studies of YSCZ 16Z

The photograph of figure 3.1(a) shows the LFED spot pattern obtained at normal incidence from a clean YSCZ (100) surface following RF annealing to 1200°C for ten minutes. No impurities were observed in XPS.

In addition to the (20) spots, additional half-order spots were observed which can only arise from a (2X2)

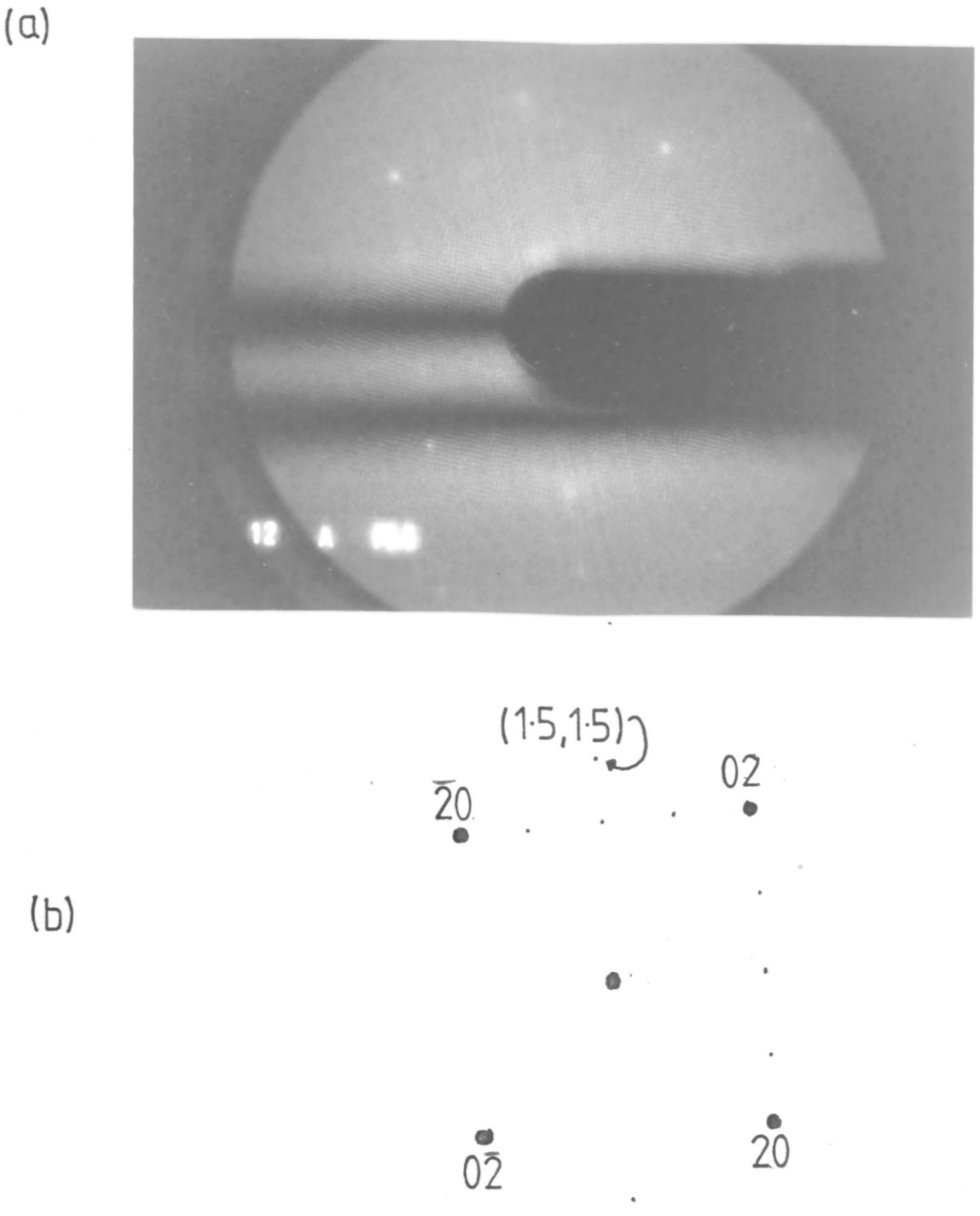
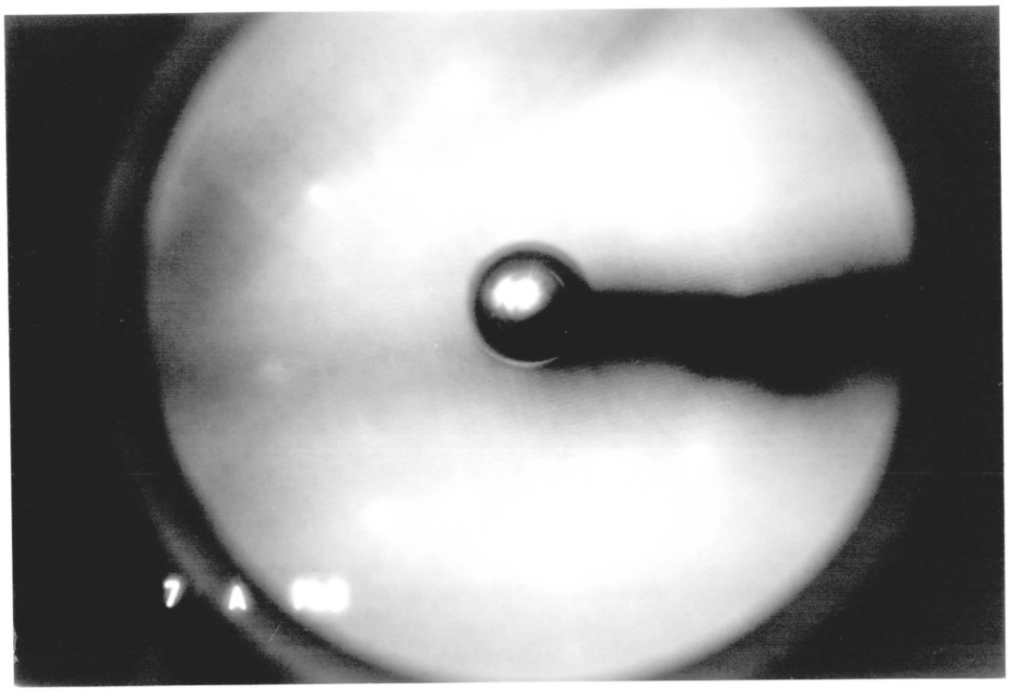


Figure 3.1 LEED of 16% YSCZ at 106eV beam energy. The lattice parameter obtained from the {20} spots was equivalent to that obtained from X-ray diffraction data (see Fig. 3.3). Note the very faint spots corresponding to n(1/2) orders shown more brightly in figure 3.2.

(a)



(b)

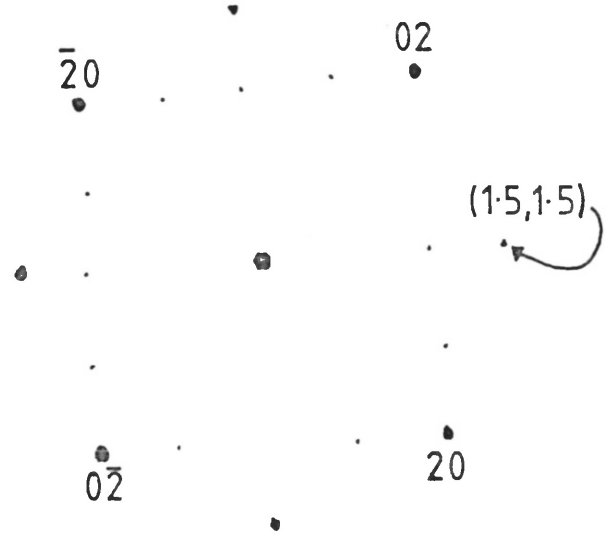


Figure 3.2 LEED as Figure 3.1 but after 30 mins exposure to the LEED beam. The background energy has increased (no contamination shown in XPS) and the {1.5, 1.5 } spots appear more brightly. A 2x2 structure is observed.

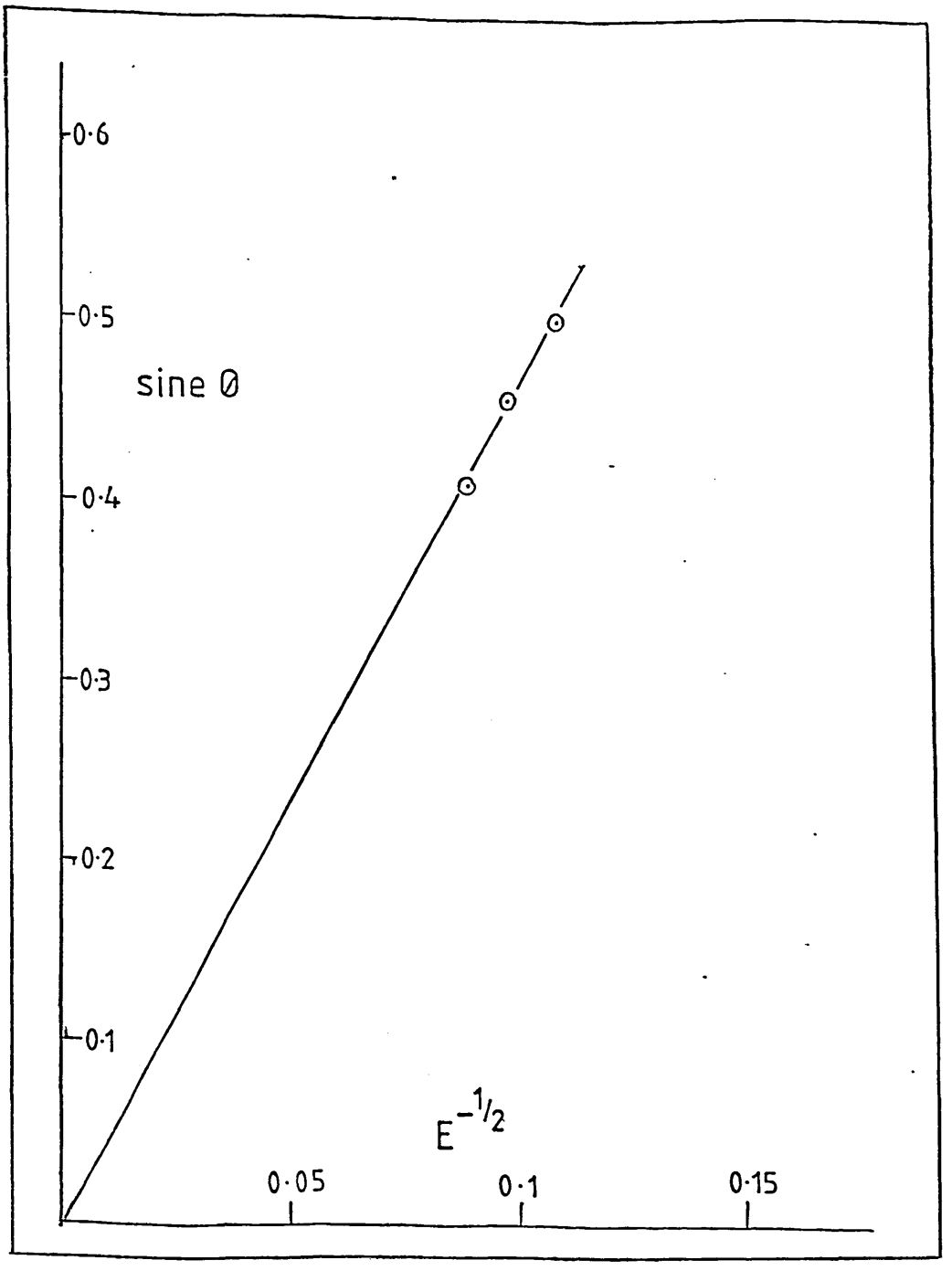


Figure 3.3 Plot of sinθ against $E^{-1/2}$ for YSCZ. The slope is proportional to the literature value for the interplanar distance of YSCZ. Note the three calculated values coincide exactly. Further points could not be taken due to charging problems.

superstructure (see figure 3.1(b)). Note in particular that there are both diagonal { 1.5, 1.5 } spots and non-diagonal { 1.5, 0.5 } half-order spots. The (2X2) spot array was analysed for various electron beam energies (from the lowest available because of charging problems) to obtain the surface lattice parameter from a plot of sinθ versus $E^{-1/2}$ [9] (see figure 3.3). The value of 5.20 ± 0.05Å obtained is in agreement with the above bulk X-ray values.

The patterns were generally of a poor quality (compared with for example the patterns from MgO see chapters 4,5) which could be due to the disruption caused by the reduction of the surface and the loss of oxygen by the LEED beam itself, or may reflect disorder of Zr^{4+} and Y^{3+} (and associated oxygen vacancies)in the surface region. Because of the poor quality of patterns it was impossible to locate {1,0} or {1,1} spots, although the overall symmetry of the patterns leads us to believe they should not be absent.

3.3.1 Polar surfaces

Surfaces of ionic crystals can usually be classified by considering the crystal as a stack of planes[10]. The total sum of the electrostatic forces over all the planes can then enable one to calculate surface energies and the most likely configuration of the relaxed surface.

Tasker[10] has classified surfaces of ionic solids into

three main types with special reference to the repeat unit of a particular structure (see figure 3.4(a)). Type I surfaces have neutral planes due to equal numbers of oppositely charged ions in the single plane repeat unit. Type II have charged planes but are sequenced in a symmetrical fashion so that the dipoles perpendicular to the surface cancel. Type III, and the most relevant here, are polar surfaces having planes of alternating charge and the repeat unit has a non-zero perpendicular dipole.

When there is a dipole moment in the repeat unit perpendicular to the surface in an ionic crystal, lattice sums in the electrostatic energy diverge[10]. Fields due to the dipoles cancel except those due to the surface plane which extend an infinite distance into the crystal and the potential at any one ion site never reaches a constant bulk value. The calculated surface energy, which is related to the internal potential, is therefore infinite. Such surfaces should not exist and the apparent natural occurence of these crystal faces has been associated with the adsorption of foreign atoms or surface roughening. If, as in figure 3.4(b) it were possible to negate the dipole moment of the 'forbidden' polar surface by introducing a redistribution of charge (brought about by the reconstruction or vacancies) these crystals could be envisaged to have a quadrupolar repeat unit with no dipole perpendicular to the surface and are therefore stable.

Some examples of polar terminations on structures

(a)

Charge	Type I	Charge	TypeII	Charge	TypeIII
neutral	$M^+X^-M^+X^-M^+X^-$	-1	$X^-\ X^-\ X^-\ X^-$	-1	$X^-X^-X^-X^-$
neutral	$M^+X^-M^+X^-M^+X^-$	+2	$M^{2+}M^{2+}M^{2+}M^{2+}$	+1	$M^+M^+M^+M^+$
neutral	$M^+X^-M^+X^-M^+X^-$	-1	$X^-\ X^-\ X^-\ X^-$	-1	$X^-X^-X^-X^-$
neutral	$M^+X^-M^+X^-M^+X^-$	-1	$X^-\ X^-\ X^-\ X^-$	+1	$M^+M^+M^+M^+$
neutral	$M^+X^-M^+X^-M^+X^-$	+2	$M^{2+}M^{2+}M^{2+}M^{2+}$	-1	$X^-X^-X^-X^-$
neutral	$M^+X^-M^+X^-M^+X^-$	-1	$X^-\ X^-\ X^-\ X^-$	+1	$M^+M^+M^+M^+$
	$\mu = 0$		$\mu = 0$		$\mu \neq 0$

(b)

X^-X^-

$M^+M^+M^+M^+$ Quadrupole

$X^-X^-X^-X^-$

$M^+M^+M^+M^+$

$X^-X^-X^-X^-$

~~~~~~~~etc

$X^-X^-X^-X^-$

$M^+M^+M^+M^+$

X^-X^-

$\mu = 0$

(c)

O O O

Zr Zr Zr

O O O O O O

Zr Zr Zr

O O O O O O

~~~~~~~~~~~~etc

O O O O O O

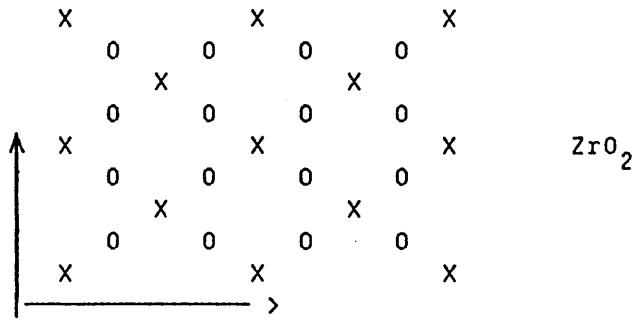
Zr Zr Zr

O O O

$\mu = 0$

Figure 3.4 (a) The three types of crystal termination as denoted by Tasker[9]. (b) The surface for type(III) that has been 'stabilized' due to only 1/2 monolayer O coverage at the crystal/vacuum interface. (c) The supposed structure of YSCZ which could stabilize the fluorite(100) face. Note only 1/2 the oxygen atoms are present in both surfaces. The charge of the 1st and the 2nd layers together with 1/2 due to the third layer can be thought of as a quadrupole and hence the dipole in the repeat unit is effectively cancelled.

(a)



(b)

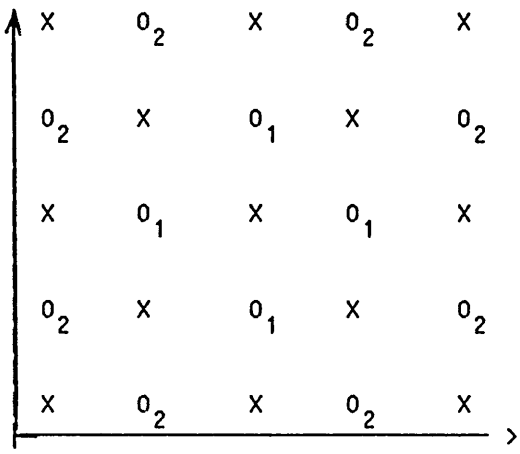


Fig 3.5(a) The original fluorite structure, note that the atoms X or O are not in the same plane.

Fig 3.5 (b) The half monolayer of O atoms (see text) giving a 2 x 2 pattern with the larger unit cell.

commonly adopted by simple ionic compounds are NaCl(111), CsCl(100), fluorite(100) (as here),zinc blende(111) and (100) and wurtzite (0001) and (1011). The surface must however exist in a reconstructed form of the simple termination plane so that it can be stable. Reconstruction is often evident from non-integral order beams in LEED. For example UO_2 (100)[11] has a c(2X2) LEED pattern and the CoO (111)[12] surface is also stabilized by a more complex structure. Here YSCZ (fluorite 100) also shows a (2X2) LEED pattern indicative of restructuring and follows the general trend of polar surfaces.

With regard to the thermal stability of these surfaces, facetting can occur at elevated temperatures. For both MgO (110) and (111), faceting occurs after annealing above 900K via electron bombardment, to form the more stable MgO(100). This is beautifully demonstrated[13] by scanning electron micrographs showing little pyramids of MgO(100) as much as 1μm across growing out of the Mg(111) surface.

In the present case no facetting was observed after the routine annealing at 1360°C outside the spectrometer.In a further experiment a 16% YSCZ crystal slice was annealed in air at 1600°C for 48 hours. An unaffected LEED pattern was still observed after this treatment. Thus we believe the stability of Y-doped ZrO_2(100) is genuinely thermodynamic.

3.3.2 Discussion of possible structures for YSCZ

UO_2 (100) is similar to YSCZ (100) in that it has a

polar fluorite structure. Taylor and Ellis[14] have reported LEED and ISS studies of UO_2 which we can use here for comparison. They report that the UO_2(100) surface did not facet at temperatures up to 950°C and that a well ordered clean UO_2(100) surface gave a c(2X2) spot pattern where the (± n/2, ± n/2) spots, n odd, are on average much weaker than the other half order features. Together with ISS measurements (showing a double cut off) and Laser Transform modelling techniques they come to the conclusion that the surface consisted of a monolayer of oxygen atoms in zig-zag distorted chains. Tasker[15] has also performed a theoretical analysis of the UO_2(100) system with the same conclusions.

This zig-zag monolayer structure allows the crystal to be stable in terms of the above mentioned electrostatic considerations because the top oxygen ion layer only has half of the opposite charge of the underlying uranium layer. The repeat unit can be considered to be quadrupolar in nature (see figure 3.4 (c)) and has no dipole moment perpendicular to the surface, due to a cancellation from the half charge surface layer.

The qualitative difference for YSCZ is that diagonal half order spots are not weak, as shown in figure 3.1(a)and in figure 3.2(a). Hence the structure is likely to be similar to that of UO_2(100) in that we have a half monolayer of oxygen atoms at the surface but in a different orientation. Figure 3.5(a) shows the two dimensional surface structure of the fluorite structure which would

give a c(1X1) pattern. Figure 3.5(b) shows one possible structure giving a (2X2) pattern which can be compared with the structure in figure 3.4(c). The oxygen atoms in positions O_1 and O_2 must be slightly differentiated by lateral or outward displacements.

The problems with LEED analysis of YSCZ are threefold. Firstly the crystal charges up as it is an insulator at room temperatures and obtaining a pattern below 86eV beam energy proved to be impossible. Therefore the lower order spots were not visible. This was also reported by Ellis[11] for UO_2. Secondly the patterns were a strong function of electron beam exposure because of reduction and the resultant disruption of the surface. Thirdly a reasonably high percentage of Y^{3+} ions are present in the surface layers (see below) and this apparently random distribution of Y^{3+} and Zr^{4+} adds to the background intensity of the LEED patterns.

The detailed structure could be determined in the future using ISS, dynamic LEED analysis and perhaps some theoretical calculations.

3.4 XPS Studies of YSCZ

3.4.1 The quantification of Y^{3+} segregation

Figure 3.6 shows XPS spectra in the 3d region of both the crystals used . A wide scan spectrum of the 16% YSCZ can be seen in figure 3.7(a) with the respective 3d, 3p,

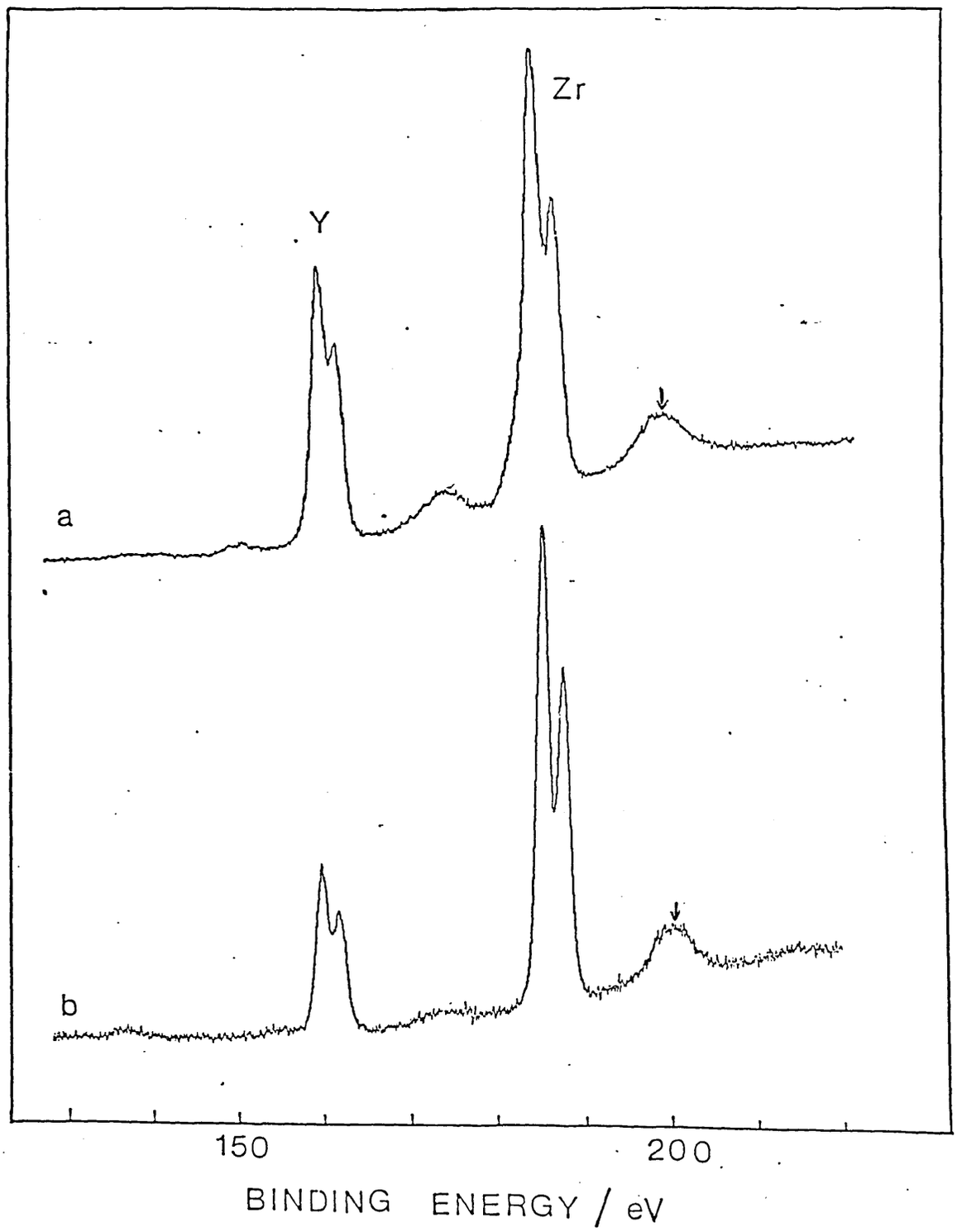


Figure 3.6 (a) Al:Kα XPS of the 3d region of YSCZ(16%) (b) Mg:Kα XPS of the 3d region of YSCZ (9%). See table 3.1 for Y/Zr ratios for comparison with stoichiometries from X-ray diffraction data. Note also that the shake up peaks at higher binding energy.

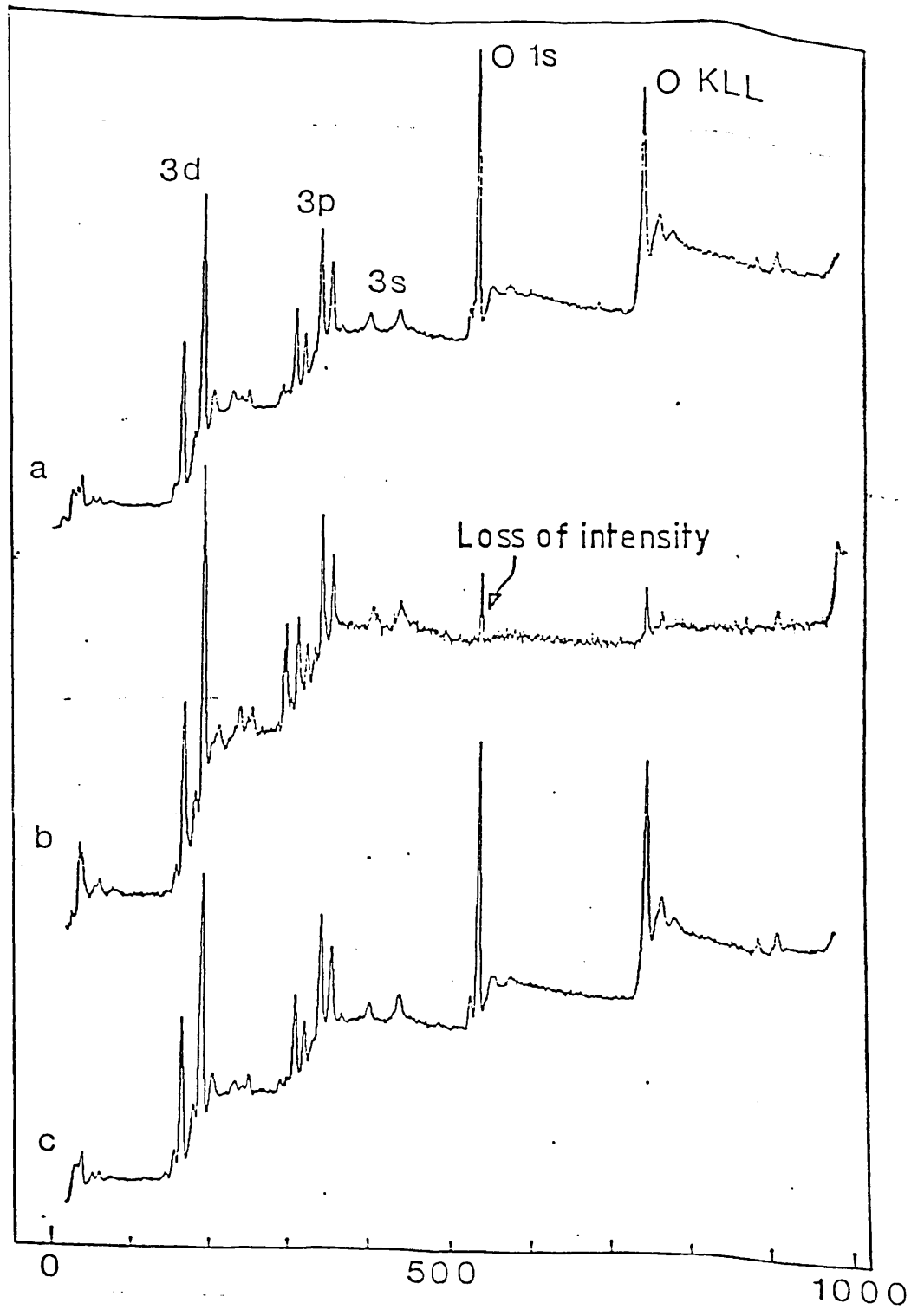


Figure 3.7 Mg Kα wide scan spectra of 16% YSCZ. (a) Resistively annealed sample (b) Electron bombarded sample (2.5 KeV, 5mA/cm^2 for 1000 seconds) (c) Argon ion etched sample (2.5 KeV, 20μA sample current for 1200 seconds) There is a drastic loss of O:1s intensity after electron reduction and a return to the previous stoichiometry after argon ion etching.

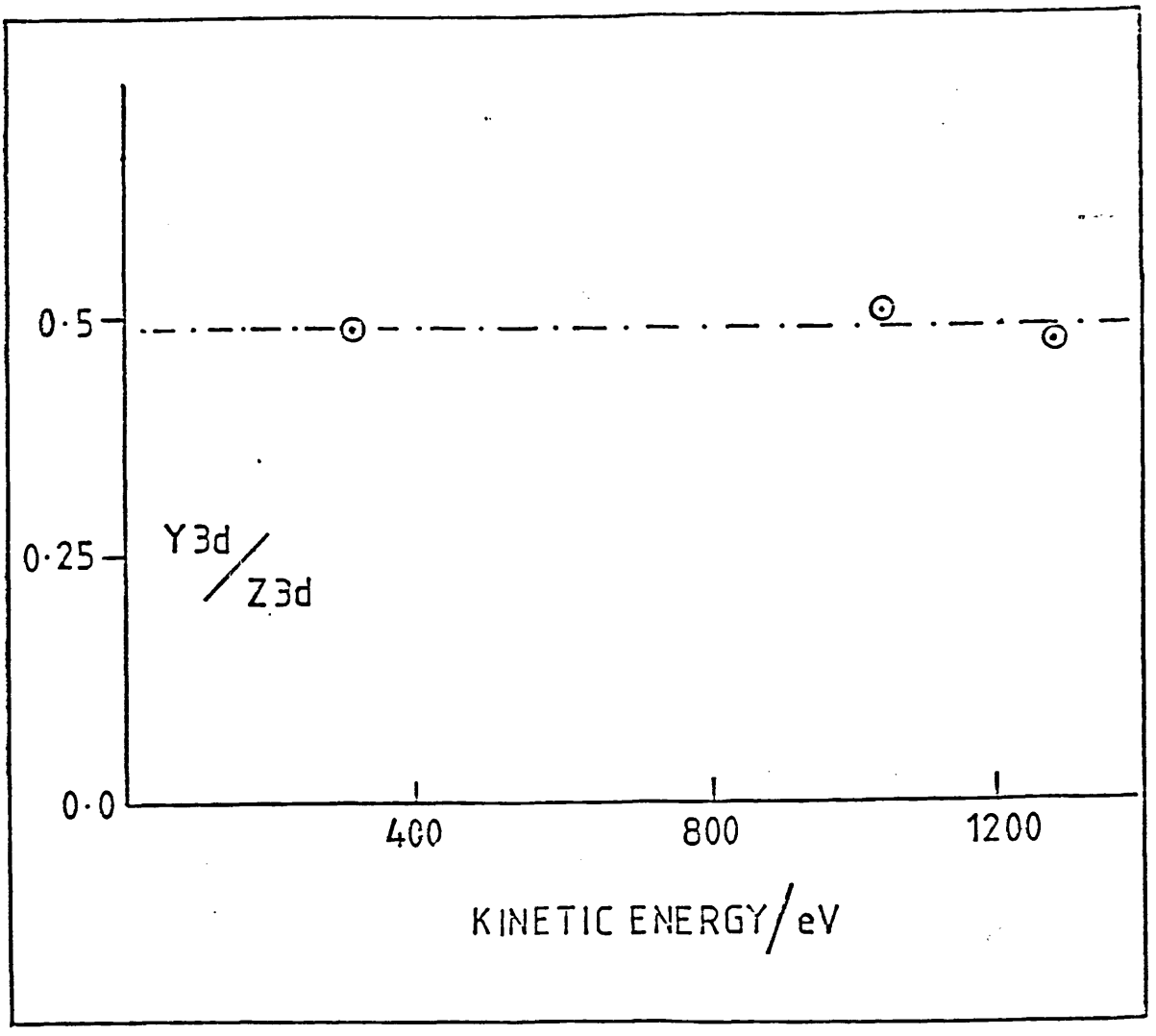


Figure 3.8 Variation of Y/Zr ratio region versus kinetic energy for 16% YSCZ. The three exciting radiations used were MgKα, OKα (impurity) and AlKα. The constant value is indicative of segregation of Y^{3+} over a large distance compared with XPS pathlengths.

and 3s regions. A summary of peak intensity ratios of the XPS peaks, corrected for cross sections, and with emphasis on the Y/Zr ratios can be found in Table 3.1 .

The ratios show obvious segregation of Y^{3+} to the surface. Together with the fact that when the crystal was lightly argon ion etched there was no change in the ratio, the conclusion is that segregation occurs over several monolayers and is not restricted to the topmost ionic plane.

Figure 3.8 shows the variation of the Y/Zr ratio in the 3d region (not corrected for cross section) with changing electron kinetic energy corresponding to excitation by MgKα, AlKα and the impurity OKα X-ray radiation. Altering the exciting radiation source alters the electron pathlengths thus the constant ratio also suggests that segregation occurs over a number of monolayers.

Angular resolved XPS

With reference to the segregation of Y^{3+} to the surface, we can assume that changing the angle of emission would increase the relative intensity of the segregant provided that the segregation is over a distance less than the sampling depth of XPS. Table 3.2 shows that there is no change in the Y/Zr ratio going from normal to 20° emission or even to very grazing emission at 5°. This result is in accord with the normal XPS experiments.

Table 3.1

(a) XPS of 16% YSCZ excited by MgKα radiation

corrected for cross section (Schofield)

Peak Ratio	1	2	3	4
Y $3p_{3/2}$ / Zr $3p_{3/2}$	0.66	0.71	0.63	0.38
Y 3d / Zr 3d	0.68	0.63	0.57	0.38
Y $3p_{3/2}$ / O 1s	0.20	1.23	0.31	0.15
Y 3d / O1s	0.21	1.27	0.33	0.15

Where: (1) Is the initially cleaned sample with light argon ion sputtering only

(2) Electron bombarded (with total reduction of the Zr(IV) species see Figure 3.7) for 17 minutes at 2keV.

(3) Argon etched sample after (2) until no reduced peak is present.

(4) Assumed ratio from the crystal stoichiometry.

(b) XPS of Y3d/Zr3d 16% YSCZ excited by various radiation.

Okα = 0.49 AlKα = 0.48

MgKα = 0.51 (values not corrected for cross section)

(c) XPS OF 9% YSCZ excited by MgKα radiation.

Peak ratio	1	2
Y3d/Zr3d	0.42	0.19

Where: (1) Measured ratio (2) Ratio from the bulk crystal stoichiometry

Table 3.2 Angle resolved XPS of 9% YSCZ

Emission angle	Y3d / Zr3d
Normal	0.42
20°	0.41
10°	0.40

Table 3.3 Spin Orbit splittings in XPS of YSCZ

Peaks	Δ so / eV
Y3p	12.0
Zr3p	13.6
Y3d	2.0
Zr3d	2.4

Table 3.4 XPS shake-up 'energies'

Compound	Peak of satellite	Δ_s/eV
YSCZ	Y3d	13.6
	Zr3d	14.5
ZrO_2	Zr3d	14.5
Y_2O_3	Y3d	13.6

Note that $\Delta Zr^s > \Delta_s Y$ and that for the parent oxides Δ_s is the same as in YSCZ.

Discussion

Our experiments demonstrate significant surface enrichment by Y for both 9% and 16% YSCZ. In a general way we can understand the segregation in terms of the large ionic size of Y^{3+} as compared with Zr^{4+}, and the relief of elastic strain by accomodating Y^{3+} at the surface. However segregation appears not to be restricted to the topmost ionic layer but takes place over a length range which is large when compared with XPS pathlengths. This observation is somewhat suprising because model simulations of ionic crystals usually suggest that although the Madelung potential may differ significantly from that of the bulk, there is an abrupt return essentially to the bulk level in the next ionic layer (see also chapter 4). Thus segregation is expected to be restricted to the topmost layer.

YSCZ(100) has proven to be a difficult system for lattice simulation studies (W.C. Macrodt, personal communication), owing to both the high concentration of oxygen vacancies and high bulk Y^{3+} doping level; and to the general problems of achieving convergence of lattice summations when dealing with polar surfaces. Conceivably the large depth range of segregation may be connected with the long range forces present at polar surfaces, but more theoretical work is needed to explore this idea further.

3.4.2 XPS shake-up structure of YSCZ and comparison with Y_2O_3 and ZrO_2

For YSCZ, strong and well-defined shake-up satellites[16] are observed on the higher binding energy side of the parent 3d peaks as in figures 3.6(a) and (b) (shown by arrows). Similar shake-up satellites were observed for ZrO_2 and Y_2O_3 depicted in figure 3.9(a) and (b) respectively.

The satellite energies are shown in Table 3.4 , the magnitudes of which, are taken from the peak of the $3d_{5/2}$ to the maximum of the shake-up. The magnitude of the shake up energy was all that was important for analysis, because the shake-up peaks were not resolved into the two 3d spin orbit components.

Discussion

The energy distribution of the photoelectrons corresponding to the shakeup peaks is determined by the (N-1) electron eigenstates left behind on the core hole site. It is the excitations of these states that give rise to the shake-up phenomena. It is postulated[17] that two main mechanisms exist for screening the core hole formed by ionisation of the metal centre in an ionic solid.

(1)Polarisation (exciton satellites)

A mechanism for screening of the core hole is polarisation of the ligands, where the electrostatic field

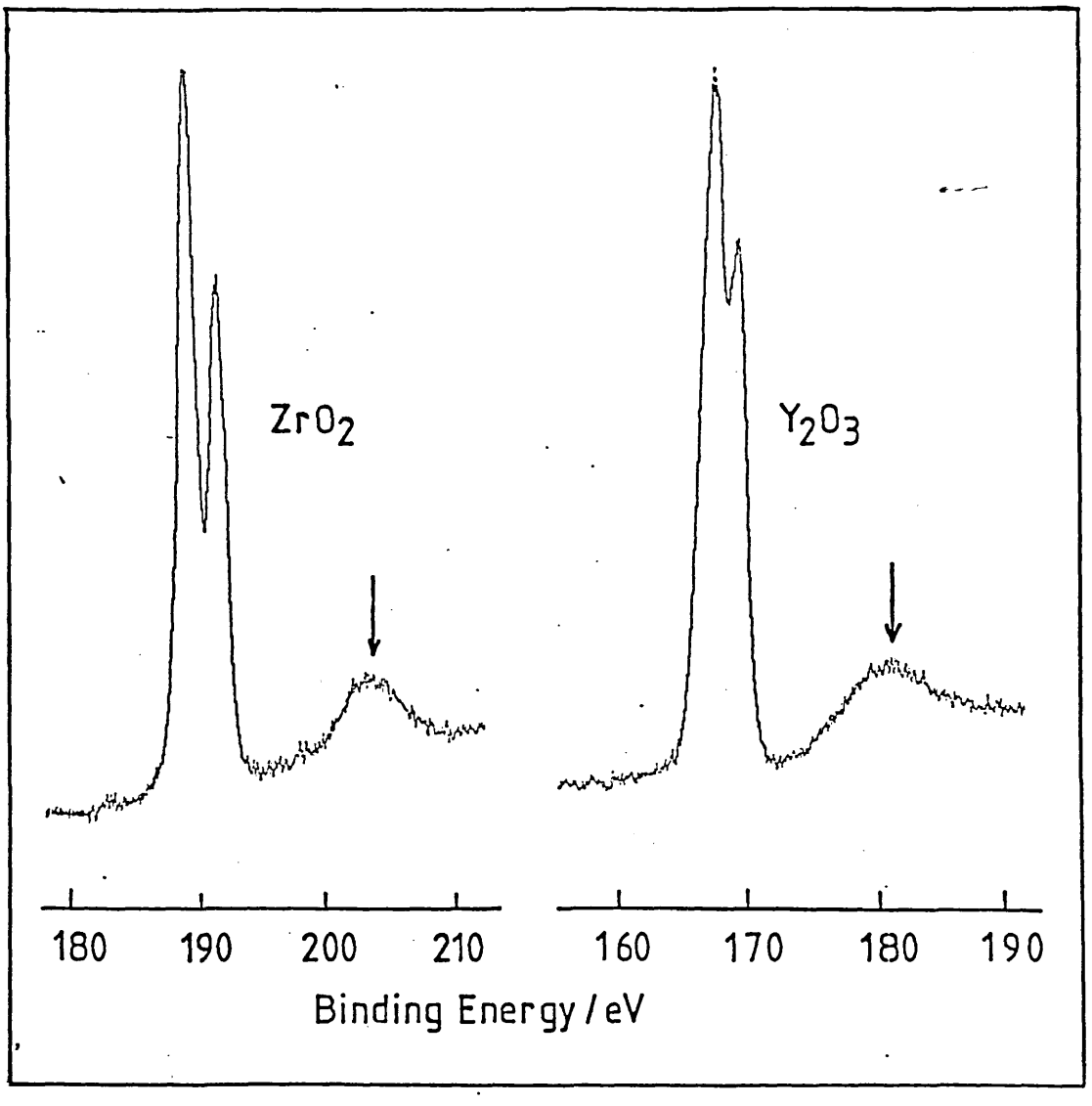


Figure 3.9 (a) Mg:Kα XPS of the 3d region of ZrO_2 (b) Al:Kα XPS of the 3d region of Y_2O_3. Note the shake up peaks at higher binding energy from the main 3d lines and the similarity to figure 3.6

caused by the core-hole pulls the electron density toward the ionized centre. This corresponds to a mixing between the ligand 2p level and the higher virtual 3s and 3d levels. A simple picture of this process is shown in figure 3.10(a). The core-hole polarises the anion, and the initially orthogonal filled, and virtual ligand levels are mixed together and pushed apart in energy, being displaced down and up by respective energies of ±Ep. There are two final states F(0) and F(1) resulting from the two sp hybrids, depicted by the change in shape of the electron wave function in figure 3.10. The shake-up energy is the energy ΔE, required to excite an electron on the ligand from F(0) to F(1). The total energy of the shake-up process is therefore the initial core-hole excitation energy plus ΔE.

(2) Charge transfer satellites

This process involves the mixing of an empty d orbital on the metal ion with a ligand valence orbital e.g 2p (and is therefore dependent on their overlap/separation) and is shown in figure 3.9(b). The field induced by the core-hole pulls the d orbital down in energy an amount Q causing a change in the hybridisation of the metal d orbital and the ligand 2p valence orbital. Again two final states arise, F(0) and F(1), and the excitation of an electron between the two gives rise to the shake-up energy. If Q > A, where A is the original energy level separation, the electron in

the lower orbital is dominantly on the metal ion. Thus in the lower energy, screened final state an electron has effectively been transferred from the ligand to the metal. To excite the F(0) state to the F(1) state the electron must be transferred back to the ligand orbital. If A > Q this situation is reversed (see figure 3.10(b)), the lower energy final state still has dominant electron density on the ligand, and the higher energy satellite involves ligand to metal charge transfer.

As both mechanisms can occur together we must consider competition between charge-transfer and exciton satellites. For smaller A and larger Q there is more d-p overlap and therefore stronger charge-transfer satellites. This process dominates in compounds of later transition elements where the band gap is small due to d orbital stabilization and there is strong metal-ligand covalency. Earlier literature[19][21] suggested that shake-up satellites were always due to charge transfer from ligand to metal. However if charge transfer is the prevalent mechanism the satellite distance is expected to decrease in the series CaO, Sc_2O_3 and TiO_2 as the bandgap decreases. In fact it increases[17] and another explanation is needed.

For the polarisation mechanism one can formulate[17]:

$$Ep = 1/2\ \alpha\ F^2 \qquad .... \quad 3.1$$

Where F is the field induced by the core and α is the polarisability of the ligand. To a first approximation, α

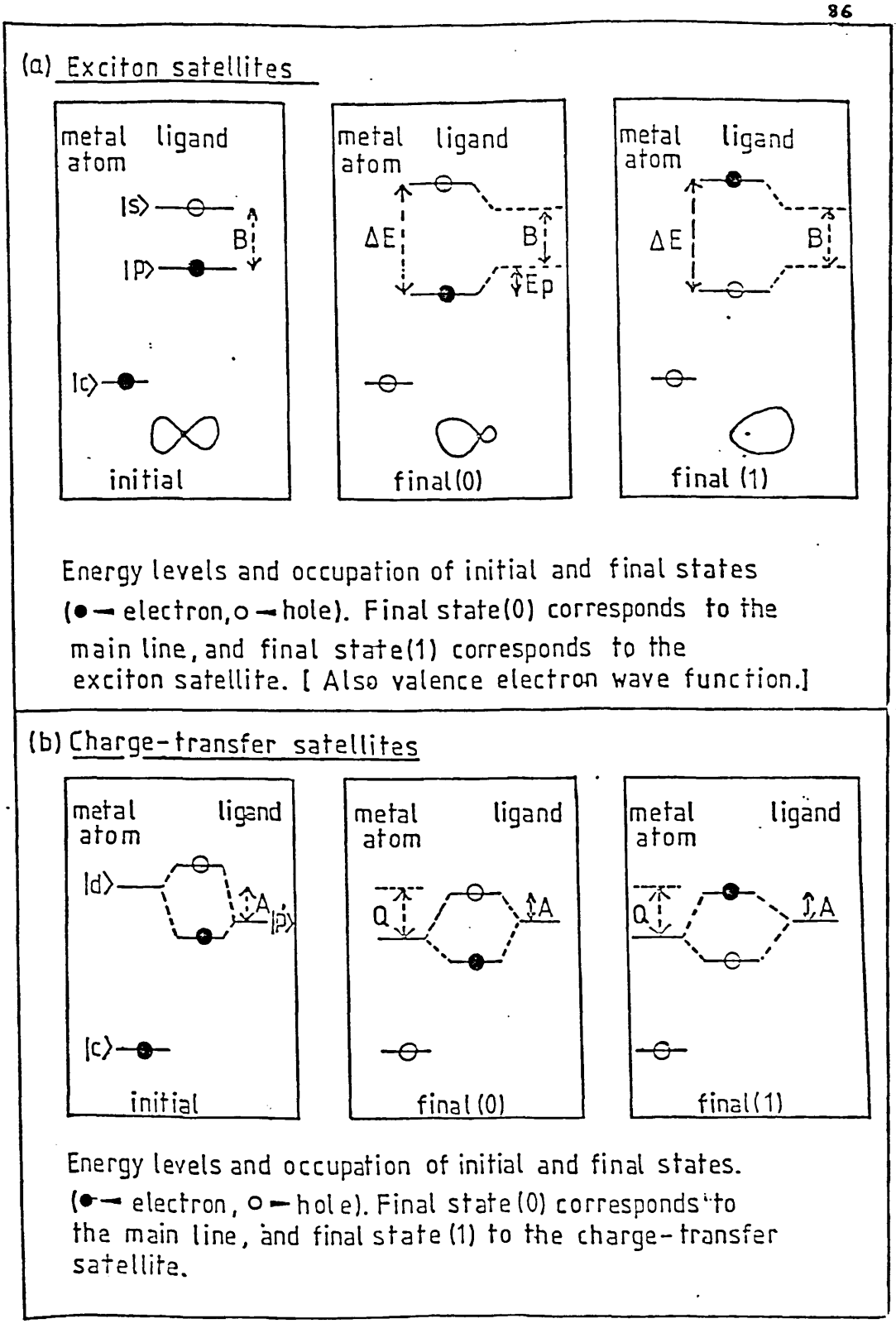


Figure 3.10 A schematic of the two suggested mechanisms for the formation of shake up satellites. Note the shapes of the valence electron wave functions in (a).

is the same for the above compounds as they are all oxides with oxygen in similar chemical environments. Also F is proportional to $1/(R)^2$ as it is a coulombic field; here R is the metal-ligand bond length.

It therefore follows that the smaller R the larger Ep and hence the larger the satellite separation. The bond length decreases for the oxide series CaO, Sc_2O_3, TiO_2 and the satellite energy increases, and we can conclude that the polarisation mechanism prevails.

The Zr-O bond in ZrO_2 is expected to be smaller than the Y-O bond in Y_2O_3 [18] hence the satellite energy for Zr3d should be greater than that of Y3d. This concurs with our findings and therefore we can reasonably conclude that the polarisation exciton mechanism is dominant for ZrO_2, Y_2O_3 and YSCZ. Note also that electron bombardment (see figure 3.13) removes the oxygen from the crystal and at the same time the shake-up peak intensity decreases in intensity, with the onset of the metal plasmon.

It is of further interest that the shake-up energies in YSCZ are identical to those in ZrO_2 and Y_2O_3, perhaps implying that the local M-O bond lengths in the solid solutions are the same as those of the parent oxides.

3.5 Electron beam reduction of YSCZ 16%

In the course of development of procedures for producing a well ordered YSCZ(100) surface, crystal slices that had been cleaned by argon ion bombardment and resistive annealing at temperatures below 600°C, were subject to electron beam heating. Even when the electron flux was directed at the back of the crystal, rapid reduction of the surface through oxygen desorption due to stray electrons occured.

Figure 3.11 shows XPS of 16% YSCZ in the Y3p and Zr3p region before and after stray 2KeV electron bombardment from a tungsten hairpin filament. The fascinating aspect of the spectra is the appearance of a second set of spin-orbit components overlapping the original Zr 3p doublet on the low binding energy (LBE) side. No concomittant changes were found in the Y 3p region until all the Zr^{4+} had been reduced. Figure 3.12(a) and (b) show the narrow scan XPS spectrum in the 3d region before and after the electron bombardment with the presence of another spin orbit doublet on the Zr3d at a lower binding energy of 2.8eV . Evidence for the second set of spin-orbit components being associated with the Zr(0) species is that the separation between the two doublets, which have the same splitting, is the same as that observed for the oxidation of zirconium foil (see section 3.5.2). Note also that quantification of oxygen loss supports this hypothesis. Wide scan spectra in figure 3.7 show the drastic loss of intensity of the O1s

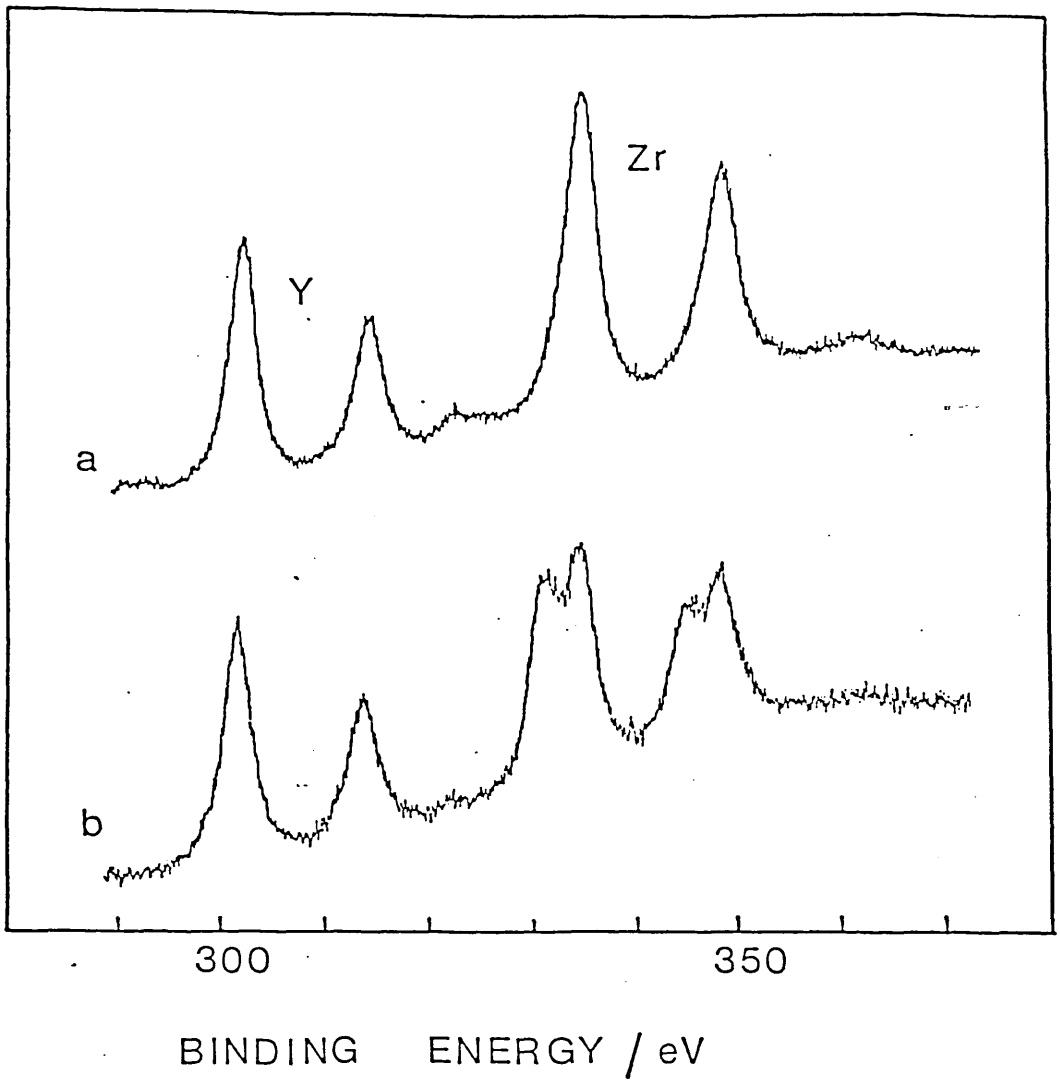


Figure 3.11 Mg Kα XPS spectra of YSCZ (16%) in the 3p region.

(a) Cleaned annealed surface
(b) Electron bombarded surface

Note the additional spin orbit components in the Zr 3p region (and not the Y 3p) to the lower binding side of the original spin orbit components.

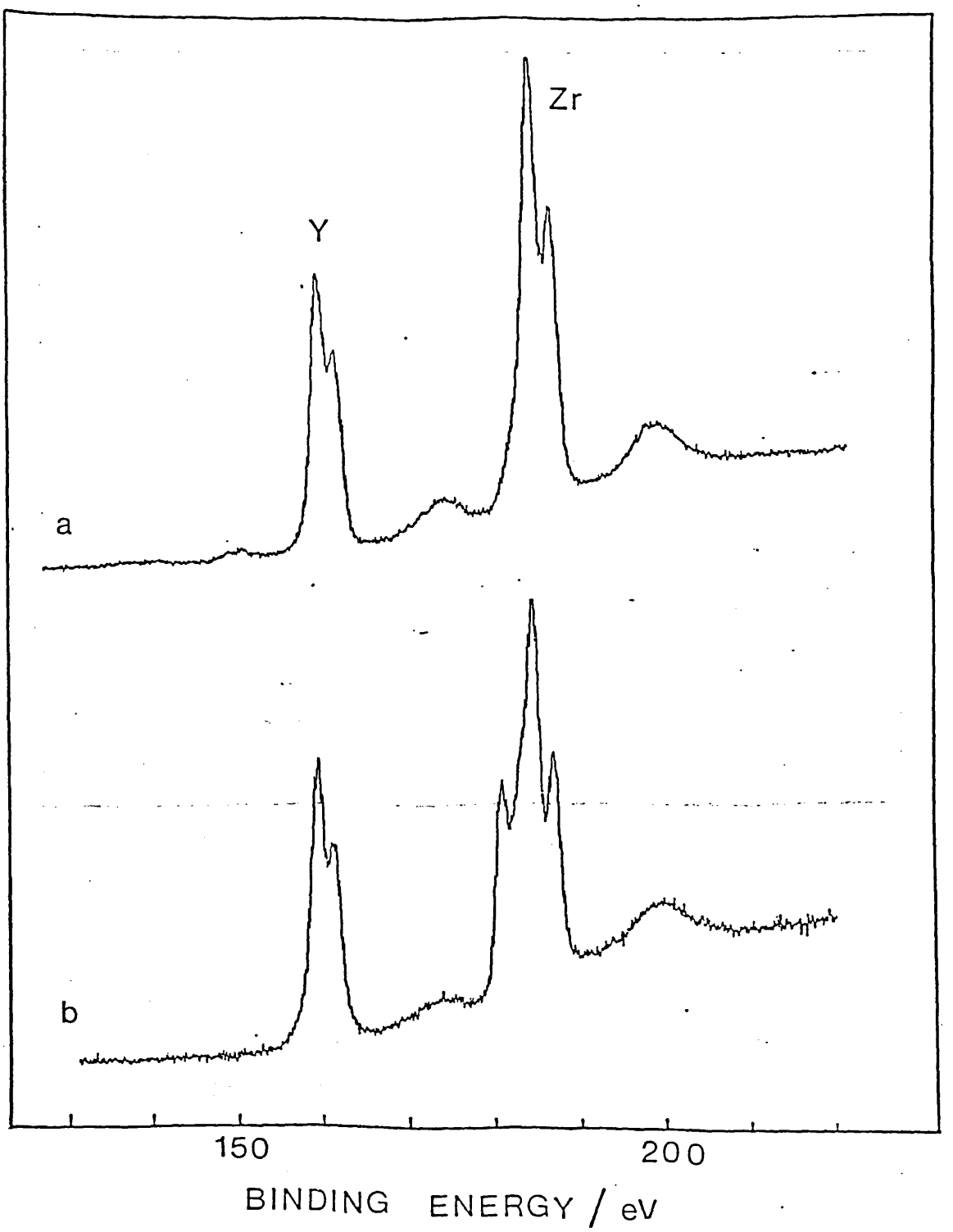


Figure 3.12 Mg:Kα XPS spectra of YSCZ (16%) in the 3d region. (a) Cleaned and annealed surface (b) Electron bombarded surface. Note as in figure 3.11 the additional structure only for the Zr:3d spin orbit doublet and on the lower binding energy side

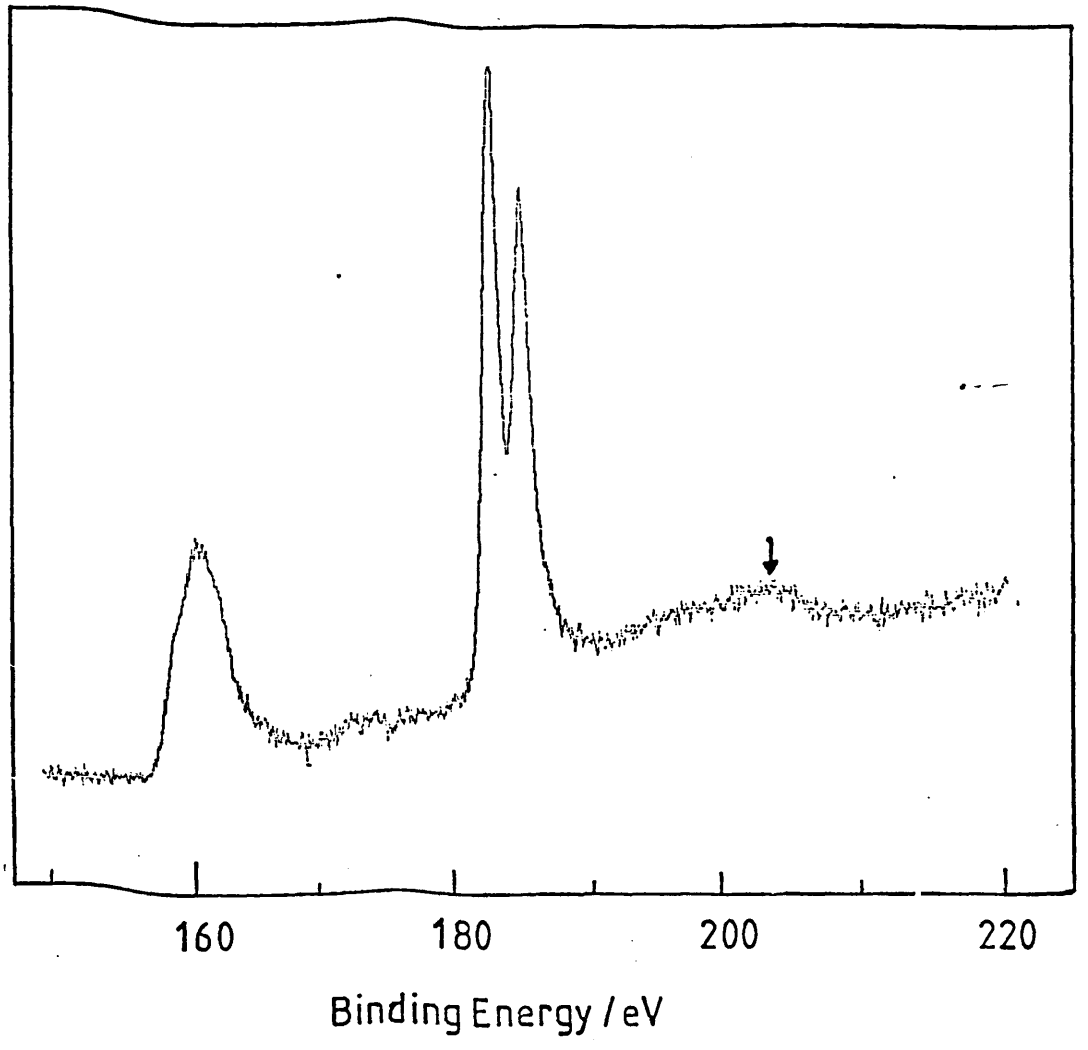


Figure 3.13 XPS of 16% YSCZ after 1000 seconds of electron bombardment at 2.5 KeV and 5mA/cm^2 target current. Note the total reduction of the Zr(IV) has occured and only the metallic 3d peak is seen. The Y3d peak now shows signs of being reduced. Note also the demise of the shake-up peak and the introduction of a peak at +20eV up in binding energy probably due to the metal plasmon.

peak with prolonged front face electron bombardment(17 minutes at 5mA/cm^2).

For these surfaces there is complete conversion into Zr(O) and a simple spin orbit doublet with typically asymmetric metallic lineshapes found in the Zr:3d and 3p regions(figure 3.13). Note also that the shape of the Y3d peak now indicates partial reduction of Y^{3+}. Further experiments revealed that one could regain the surface stoichiometry by argon ion bombardment (see table 3.1) even when the O1s XPS peak had diminished to 20% of its original magnitude.

3.5.1 Quantification of oxygen loss in the electron beam reduction of YSCZ

In order to quantify the reduction behavior under electron bombardment a cleaned annealed sample was subject to 2KeV electron bombardment with, 5mA/cm^2 target current, for various periods up to 500 seconds.

Figure 3.14 shows the growth of the LBE components of the Zr3p peaks and the diminution of the original HBE peaks. There is a constant chemical shift of 2.8eV throughout the reduction; curve fitting was necessary to measure the individual peak areas. Figure 3.15(c) and (b) show the variation of intensity with time of electron bombardment of the HBE and LBE components respectively. They are exactly mirror images as expected.

Also plotted in figure 3.15(a) is the variation of the logarithm of the O1s / Zr $3p_{3/2}$ ratio versus time with the

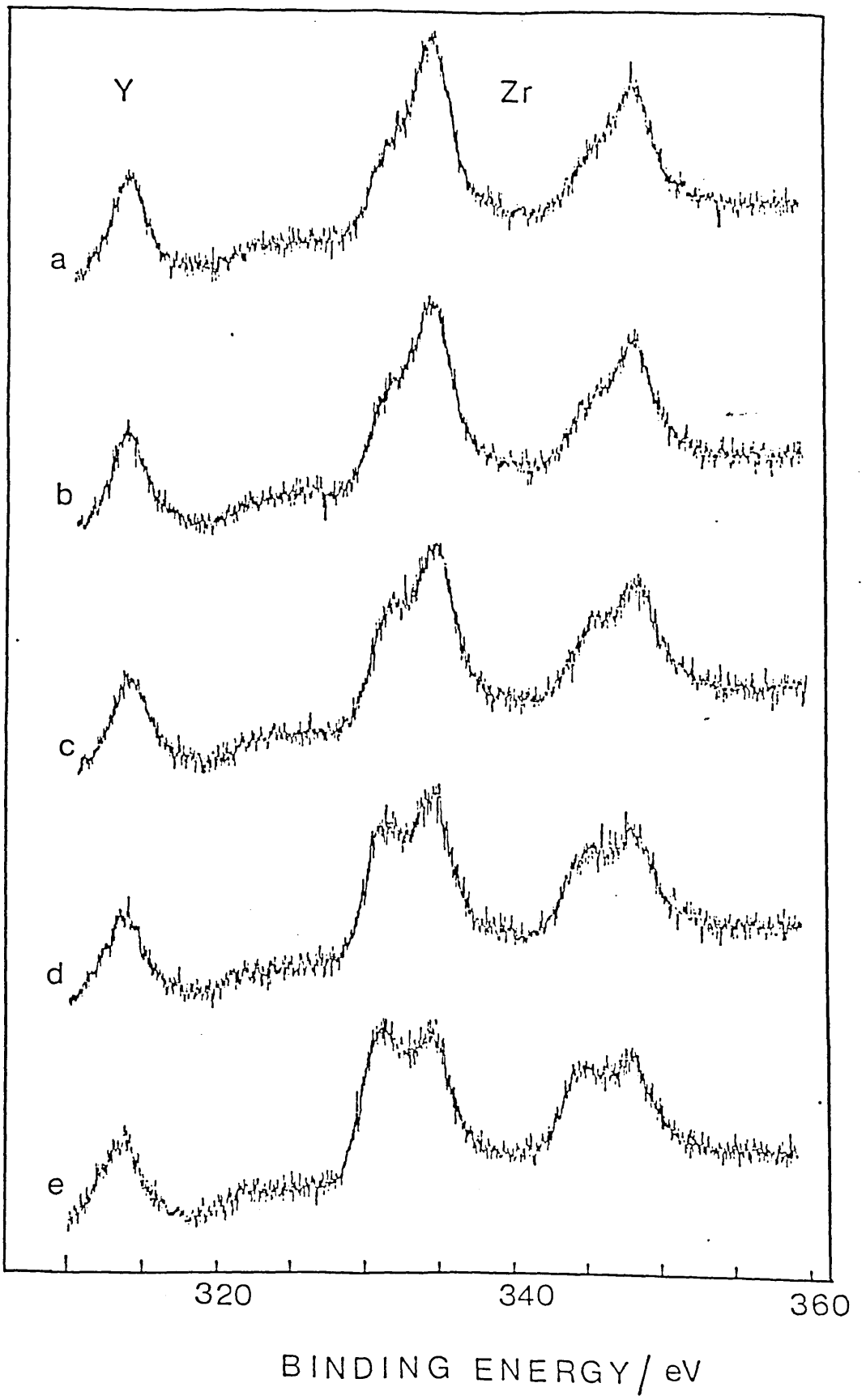


Figure 3.14 Variation with time of the Zr:3p and Y:3p signals in the Mg:Kα excited XPS spectrum of YSCZ under 2 KeV irradiation at 5mA/cm^2 sample current. (a) 82 (b) 140 (c) 200 (d) 300 (e) 460 seconds.

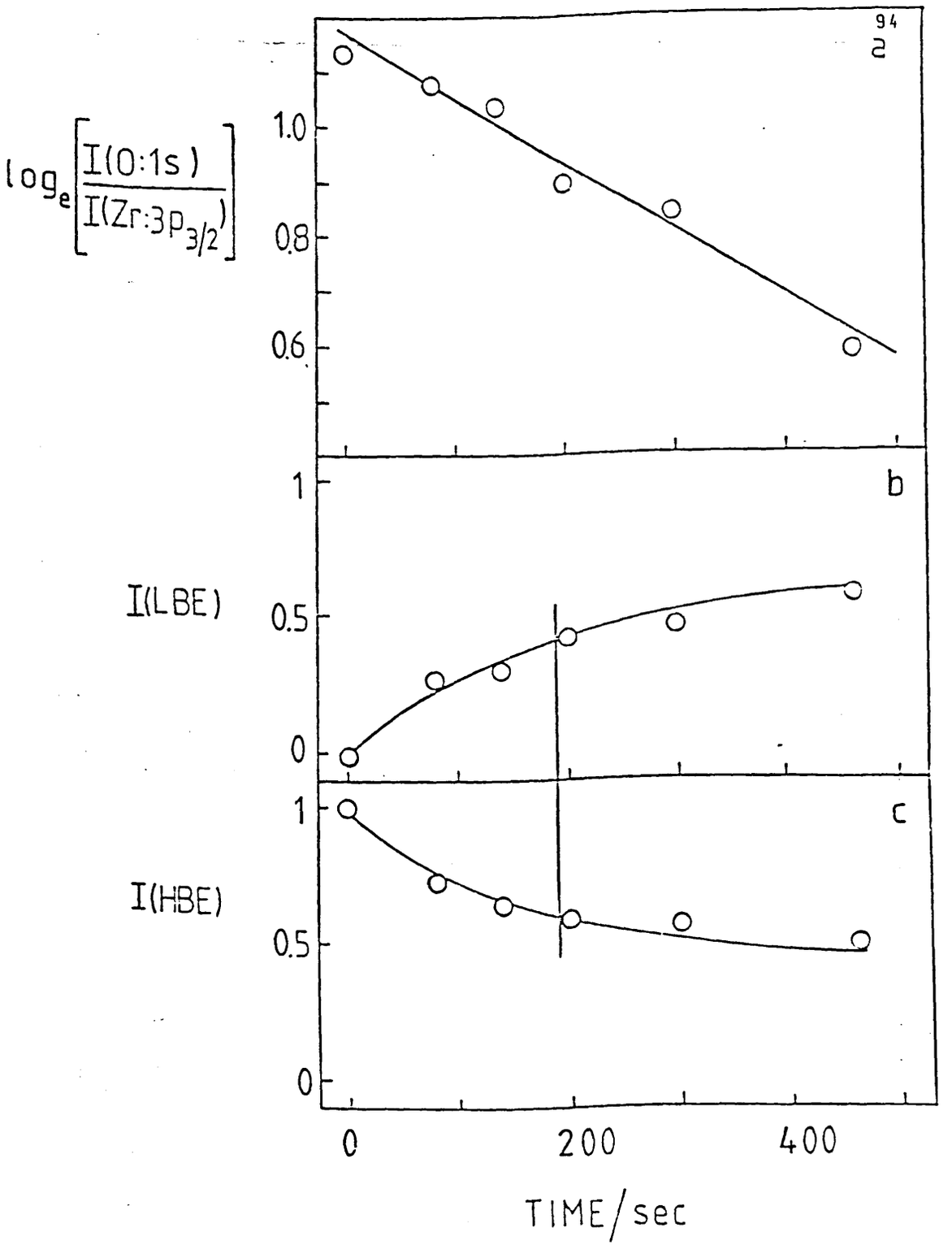


Figure 3.15 (a) The variation with time in the O:1s/Zr:$3p_{3/2}$ intensity ratio under electron irradiation as in figure 3.14 after correction for cross section effects. The decay of the oxygen intensity is seen to conform to first order kinetics. (b) variation with time of the intensity of the low binding energy (LBE) Zr:$3p_{3/2}$ component. (c) The variation with time in the intensity of the high binding energy (HBE) Zr:$3p_{3/2}$ component. In (b) and (c) the vertical line marks the time at which complete conversion to a Zr(III) species might be expected.

total area of the Zr $3p_{3/2}$ peaks taken to normalise the O1s data. The initial decay conforms to first order behavior[19] such that:

$$R(t) = R(o) \exp (-\sigma\psi t / e) \quad .....3.2$$

where:

R(t) is the intensity ratio at time t

R(o) is the initial value

ψ the electron flux (A/cm^2)

e the electron charge (C)

σ the cross section for oxygen desorption cm^2

σ was calculated from the slope to be 3.9×10^{-20} cm^2 The mechanism for the electron stimulated desorption of oxygen from d^o oxides has been formulated by Knotek and Feibelman[20]. Direct transfer of energy from the bombarding electron is insufficient to cause desorption itself but electron stimulated desorption (ESD) can be explained in terms of a mechanism in which there is the loss of three electrons from the 2p valence band of oxygen (see figure 3.16).

The mechanism involves a formation of a shallow metal core-hole and as there are no outer metal valence electrons subsequent filling of this hole is from an electron from the O2p valence band with the release of two more electrons(Auger decay). The resultant cation O^+ is in a anion site and experiences a displacement to an interstitial position due to the site potential being

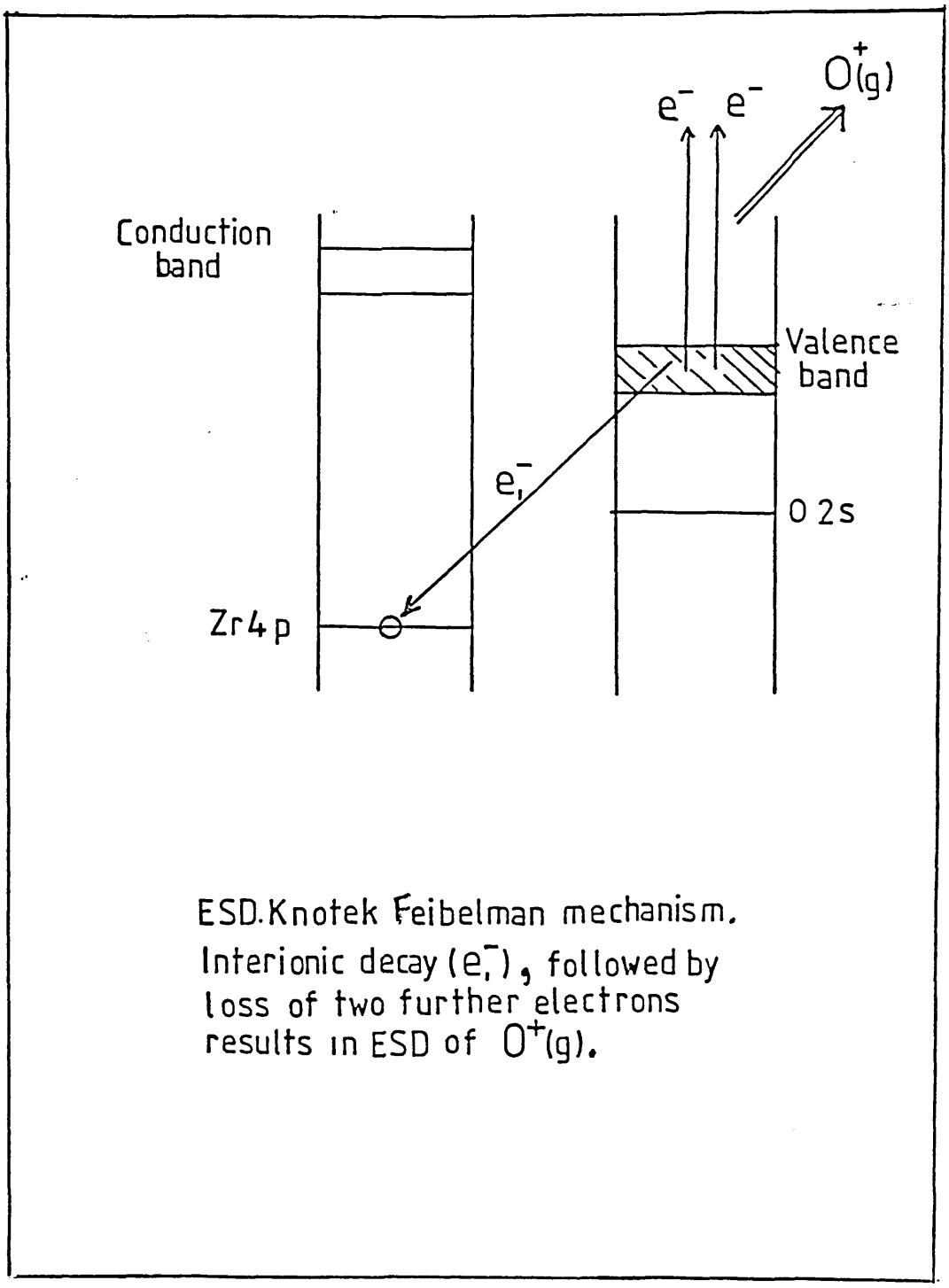


Figure 3.16 schematic showing the mechanism for the electron stimulated desorption in YSCZ.

repulsive. It is then able to desorb from the surface.

It is necessary that the process balances energetically. In oxides the O2s level is insufficiently tightly bound for ESD, and a more efficient process involves the first core hole level ionisation from the cation. Transfer of an electron to the cation occurs only when it has completely empty valence shells, e.g K_2O, CaO, Sc_2O_3, TiO_2 and V_2O_5. NiO which has a $3d^8$ structure decays via an intra-atomic Auger process , which is a direct result of better core-hole / 3d overlap.

The oxygen decay curve also allows us to gain some insight into the oxidation state of the zirconium corresponding to the LBE peaks. The surface stoichiometry worked out from XPS, allowing for the segregation, of the 16% YSCZ is $Zr_{0.63}Y_{0.37}O_{1.81}$. The O/Zr ratio inferred from consideration of O1s and $Zr3p_{3/2}$ (and its spin splitting) peaks is 3.1, in reasonable agreement with our proposed surface stoichiometry where O/Zr = 2.9 (see Table 3.1). Assuming exclusive reduction of Zr(IV) under irradiation it is possible to estimate the diminution in O/Zr intensity ratio necessary to effect complete reduction of the Zr(IV). If the LBE peak corresponded to Zr(III), the oxygen loss curve of figure 3.15 suggests that about 200 second electron bombardment should be sufficient to ensure complete conversion to the LBE species. However it is obvious from figure 3.14(a) and (b) that both the LBE and HBE species coexist after this time, precluding the possibility of Zr(III) as the product of electron

bombardment. In fact our intensity data is consistent only with Zr(0) as the product of electron reduction and electron beam exposures of around 1000 second are necessary for complete reduction of Zr(IV).

Discussion

V.A.Loebs et al[6] report that single crystal YSCZ was chemically reduced when heated in UHV, yellowing and darkening probably through loss of oxygen. Solomon[8] also reports a darkening of single crystal YSCZ at temperatures above 600°C is a result of oxygen loss, which concurs with our work here.

Many d^0 oxides undergo reduction either by ion or electron bombardment where d^1 states are introduced into the lattice and electronic properties similar to the relevant stoichiometries such as TiO_2 going to Ti_2O_3[25] or Ti_4O_7 reduced[21] are observed. The value of σ is smaller in YSCZ than the cross section for the desorption of oxygen from the tungsten (100) surface (oxidised W is WO_3 like) by 2.5KeV electrons[22] which is 1.3×10^{-19} cm^2, but of the correct order for a d^0 oxide. The corresponding cross section for decomposition of the $Na_{0.71}WO_3$ with 3KeV electrons is $6.0 \times 10^{-21} cm^2$ [19]. It has been noted[23] that oxides such as Ta_2O_5 with an energy of formation above 500KJ/mole do not undergo reduction under 400eV argon ion bombardment. ZrO_2 and Y_2O_3 with heats of formation[18] of 1037KJ/mole and 879KJ/mole respectively fall into this

category.

Electron bombardment reduces most oxides including Ta_2O_5, Al_2O_3 and SiO_2[24] and therefore the stability of Y(III) in the present work is quite remarkable. As the enthalpy of formation for the Zr-O(in ZrO_2) bond is greater than that of the Y-O(in Y_2O_3) bond it might be expected that the Y would be reduced first. An explanation might lie in the smaller covalency of the Y-O bonds which will be one factor favouring selective desorption of oxygen ions surrounded by zirconium ions. This is because the proposed Knotek-Feibelman mechanism is dependent on the transference of electrons from the oxygen valence band to a core-hole on the zirconium ions. We can also envisage that electrons left behind after oxygen desorption will be trapped preferentially in Zr4d, rather than Y4d, states. Disproportionation of these Zr^{3+} states must then occur to generate the final Zr^{o} species.

3.5.2 The oxidation of Zirconium foil

Oxidation of Zr foil is known to produce a ZrO_2 overlayer[25], and in the light of our calculations involved with the reduction of YSCZ, it was assumed that some insight into the oxidation state of the reduced species might be obtained from oxidising Zr foil.

Cleaned and annealed zirconium was subject to doses of oxygen gas at 10^{-6}torr for five minute intervals up to 25 minutes with intermediate annealing at 600°C. Figure 3.17 shows the change in the $Zr3p_{3/2}$ peak from a to e

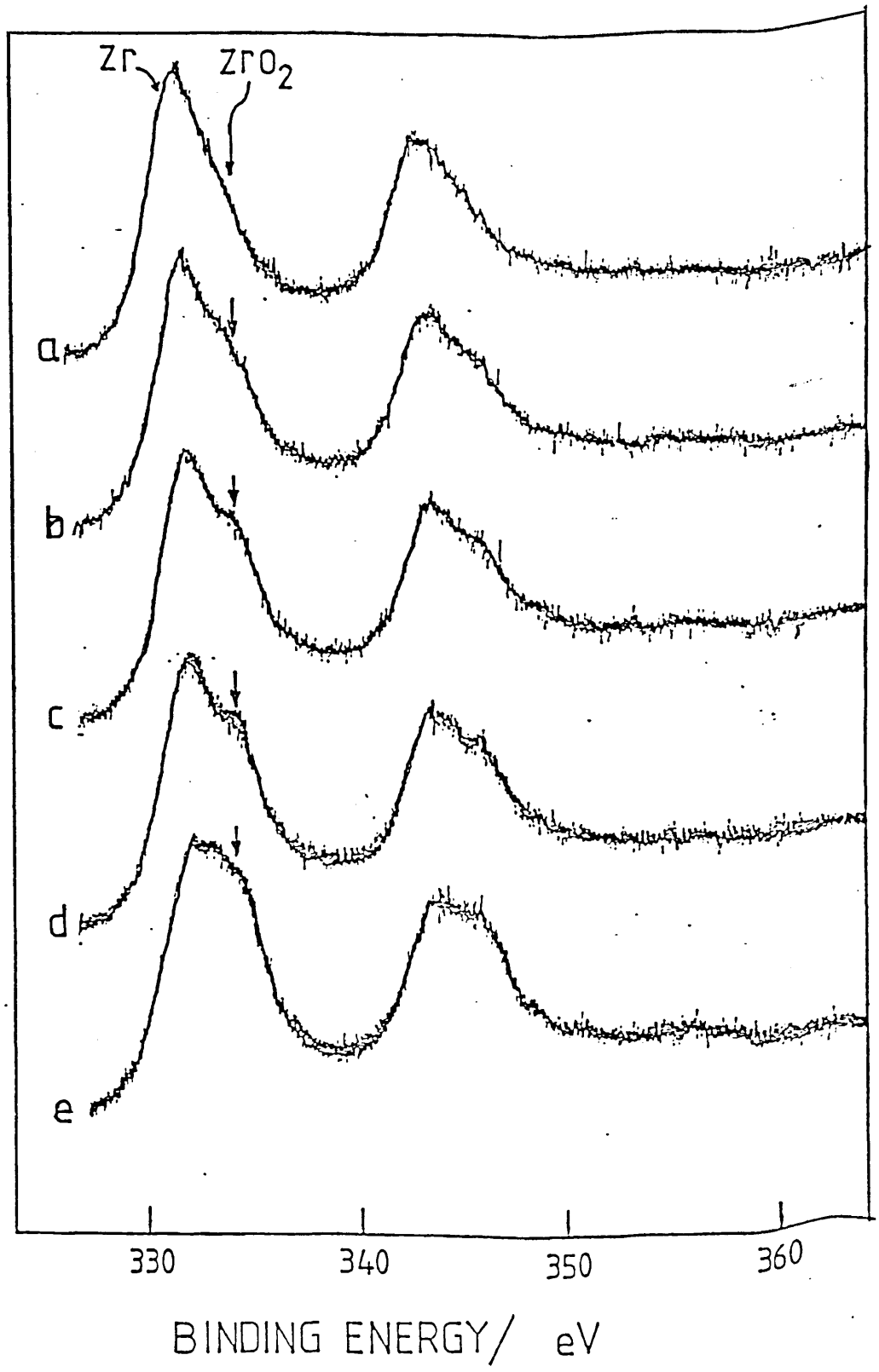


Figure 3.17 The variation of "metallic" Zr:3p with oxygen dosing and the increase of the "oxidic" Zr:3p. The chemical shift of 2.8 eV is identical to that obtained from the reduction of YSCZ by electrons. Dosing increases from (a) to (e).

representative of 5 to 25 minutes exposure respectively. The gradual increase of the HRF peak intensity and the loss of the LBE peak mirrors the reduction of YSCZ. The measured chemical shift had a constant value of 2.6 eV± 0.3eV which is very close to the value observed in the reduction of YSCZ and adds more substance to the argument that Zr(0) is formed in the latter experiment. Curve fitting procedures were necessary to accurately determine this value. The failure to observe reduced oxides other than Zr^{4+} accords with the fact that well defined bulk M_2O_3 and MO oxide phases are unknown for zirconium[26].

3.6 ELS

The ELS spectrum of 9% YSCZ after RF annealing in oxygen is shown in figure 3.18(a). The peak X at 14.5eV is close to that observed for the shake-up in the XPS spectrum in the 3d region. There is also a shoulder Y present at about 10.5eV. We have calculated that the bulk plasmon energy of 9% YSCZ is 24.95eV[27] and hence the surface plasmon at 17.64eV. It is therefore implausible that X or Y are due to these excitations.

One of the purposes of doing ELS on YSCZ was to determine the effect of argon ion bombardment and electron bombardment in conjunction with other methods to clarify defect structure. Figure 3.18(b) shows the ELS spectrum of the electron bombarded crystal. In this case the electron dose was provided by the ELS electron gun at 100μA for 10

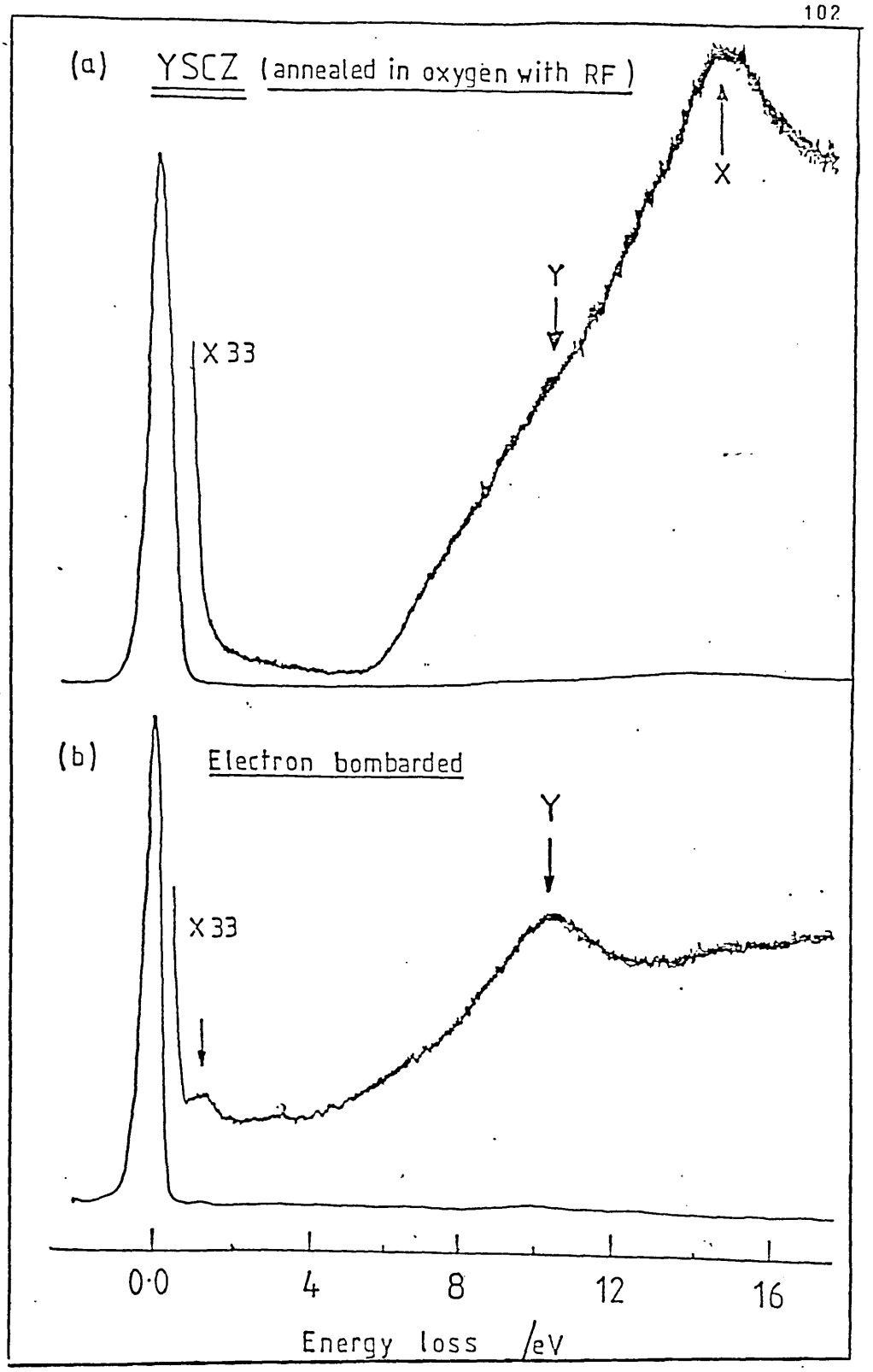


Figure 3.18 (a) ELS spectrum of 9% YSCZ annealed in oxygen with RF heating. (b) ELS spectrum of the same crystal after electron bombardment by the ELS electron gun. Note the addition of a peak at 1-1.5eV, the loss of peak X and the gain of peak Y.

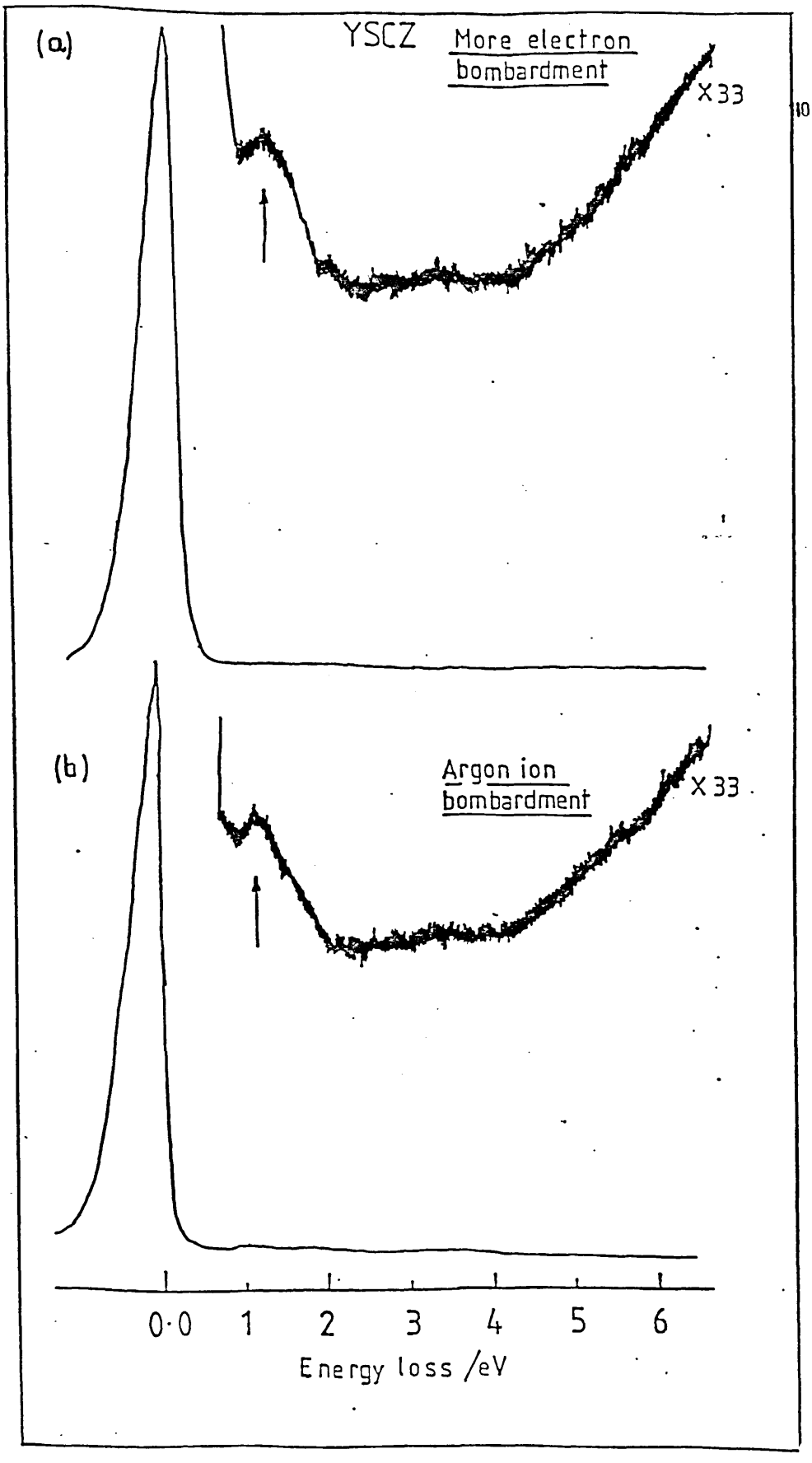


Figure 3.19 (a) ELS of YSCZ after more electron bombardment (b) ELS of YSCZ after argon bombardment of 2 KeV ions at 20μA sample cuurent for 20 minutes of the annealed crystal. Note the similarity of the spectra.

minute. Note the loss of intensity of peak X at 14.3eV. Peak Y is most probably the maximum in the interband excitation intensity and is apparently more pronounced due to the loss in intensity from peak X. There is also a new peak at 1.4eV due to the introduction of states into the band gap. This peak increases in intensity after further bombardment(see figure 3.19(c)).

The argon bombarded crystal, prepared by RF annealing in oxygen, also shows a similar introduction of defect states into the band gap(see figure 3.19(b)). This is an unexpected result as no change is seen in the XPS after argon bombardment. This probably reflects the greater surface sensitivity of ELS compared with XPS.

Discussion

The loss of peak X after electron bombardment concurs with the loss of oxygen and decreased shake-up satellite intensity. Both are due to the relevant electrons being mainly associated with the oxygen ligands. This is also seen in the XPS of the drastically reduced YSCZ(figure 3.13) where only the Zr^{o} 3d oxidation state is seen and the shake-up peak at 14.5 ev is lost. The introduction of interband states at 1.5 eV parallels behaviour of oxides such as TiO_2 [21,22] and WO_3. The darkening of the crystal to a characteristically yellow-brown colour after electron bombardment and annealing in UHV appears not to be directly correlated with the appearance of the low energy interband loss. Optical absorption spectra of darkened crystals

showed a peak at λ = 380 nm corresponding to an energy of 3.3eV . It has been suggested that the darkening is due to Ce^{4+} impurities, which are reduced to Ce^{3+}[28].

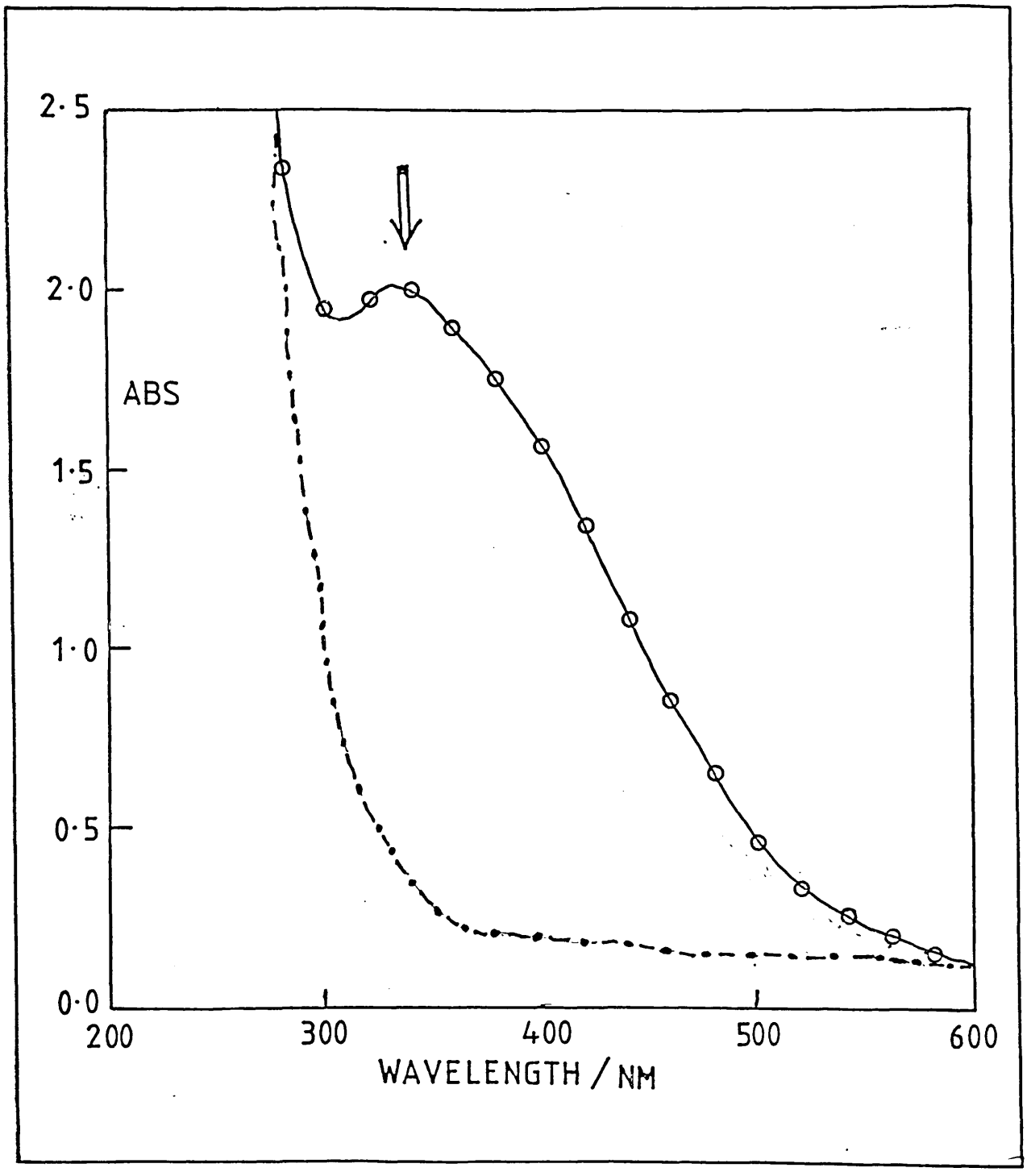


Figure 3.20 The absorption spectrum of electron bombarded YSCZ. The dotted line is absorption before reduction.

Chapter 4. Electron spectroscopy of MgO

4.1 Introduction

A major part of this thesis concerns the study of BaO deposition onto MgO and the Ba segregation in doped MgO. It was therefore necessary to obtain reference spectroscopic data from the MgO substrate and to evaluate methods of preparing clean MgO surfaces. The experimental section of the present chapter contains details of the various cleaning and annealing methods, together with a brief discussion of LEED, XPS and ELS data from MgO(001).

MgO is a highly ionic rocksalt oxide with a face centered cubic lattice, and as with many oxides the anion is somewhat larger than the cation[1]. Theoretical analysis of the electron charge distribution shows that the essentially fully ionic character found for the bulk is maintained at the (100) surface and that the anion deformation is very small[1]. The (100) planes contain equal numbers of anions and cations whereas the (111) planes are alternately composed of similar cations and anions. Thus whereas the calculated (100) surface energy is only 1.2 J/m^2 [2], the (111) surface has infinite surface energy in the simplest model[3]. The (110) surface has an intermediate surface energy of 2.9 J/m^2.

In agreement with these calculations, MgO crystals cleave naturally to expose only (100) planes. (110) and (111) surfaces can be cut from such MgO crystals, but they rearrange under mild annealing conditions to give macroscopic (100), (010) and(001) facets[4]. Careful LEED

I/V measurements for the MgO(001) cleavage surface suggests that this surface represents an almost unrelaxed termination of the bulk structure with experimentally undetectable displacements of ions away from their bulk positions[5][6]. A schematic representation of this ideal arrangement is shown in figure 4.1 . However in the lattice simulation studies a small rumpling is found with a 0.05Å outward displacement of O^{2-} anions relative to the Mg^{2+} ions. This is due to ionic polarisation with the anions moving outward to avoid the overlap with anions in the plane below.

It has long been realised that the site potentials for ions at the surfaces of ionic solids differ significantly from the bulk Madelung potentials[7][8][9][10]. For surface cations, the effect of lowering the number of O^{2-} nearest neighbours should be to increase core level binding energies whereas the surface O^{2-} core levels are expected to be destabilised. There have been few attempts to observe surface-core shifts in photoemission experiments on metal oxides, although both Cord and Courths[11] and Thornton and coworkers[12] found that on $SrTiO_3$(100) surface Ti core levels showed a surprising shift to lower binding energy. By contrast, surface Sr core levels showed the expected upward shift. The SCS for the Sr levels disappeared upon completion of the surface Sr coordination sphere by adsorption of water[12].

The experiments on $SrTiO_3$ employed synchrotron radiation tuned to an energy of around 100 eV above the core

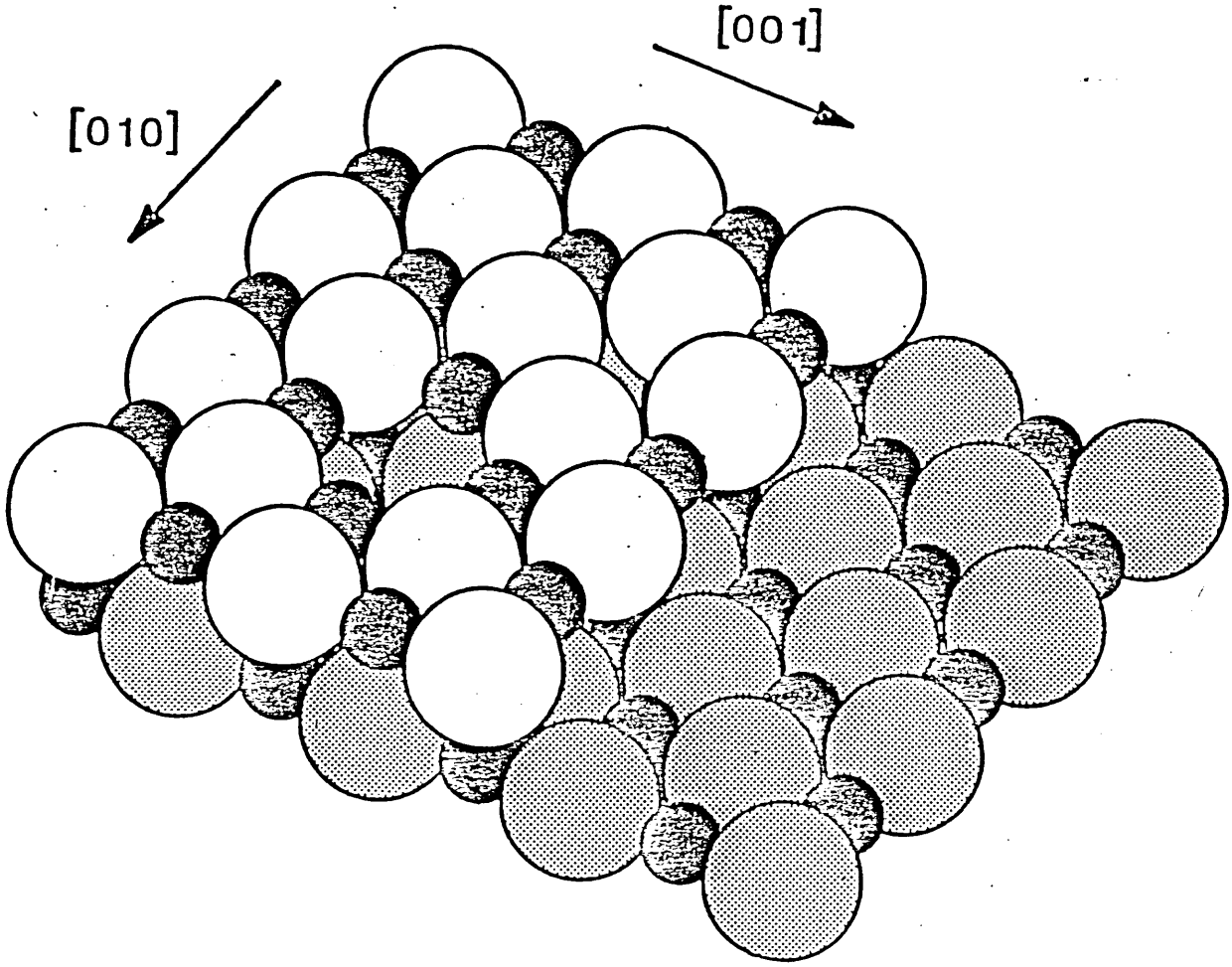


Figure 4.1 Schematic representation of the (100) surface of MgO (NaCl type). An anion vacancy and a step have also been included.

level threshold in order to ensure maximum surface sensitivity. Synchrotron radiation has also been used with good effect for the study of SCS in metallic samples[13-16]. Nonetheless it is possible to observe surface core shifts with conventional Mg or Al soft X-ray excitation, as demonstrated by the pioneering experiments of Citrin and Wertheim [17]. Note that the origin of the surface-core shift for metals is radically different to that for insulating oxides. SCS have been well documented for metals and Citrin and Wertheim present a summary and a model relating the SCS to the DOS at the metal surface. They suggest that a narrowing of a hypothetical surface band due to less bonding interaction lowers the Fermi level with respect to the bulk band Fermi level if the conduction band is more than half full. The resultant charge flow to equalise the two Fermi levels disrupts the core levels resulting in the formation of the SCS. For surfaces of polar solids by contrast the principal contribution to the SCS lies in the different Madelung potential experienced by a surface ion.

In recent experiments with the ESCALAB spectrometer used in the present work, Webber and coworkers have shown that the ESCALAB is capable of resolving the SCS for metallic Cu and related alloy systems[18-19]. This encouraged us to attempt to observe the SCS in MgO. Particular hope was attached to the Mg:1s level excited with Al:kα radiation, where the low electron kinetic energy

(183.6 eV)[20] should give excellent surface sensitivity. It transpires that the Mg:1s level is too broad to allow observation of a shift, and due consideration is given in this chapter to the factors determining widths of core lines in MgO.

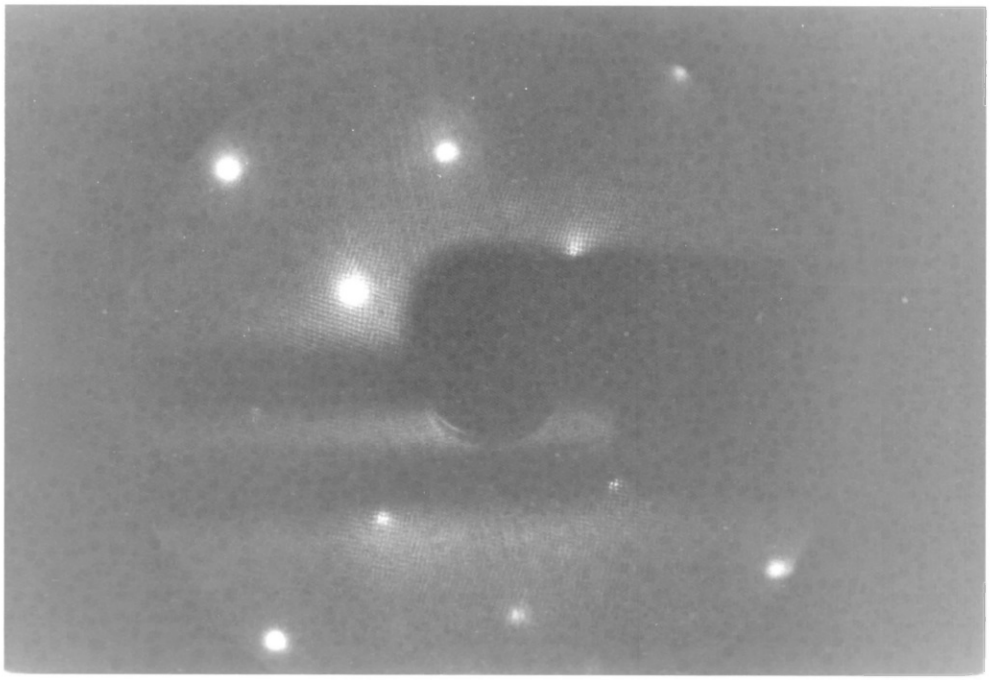
4.2 Experimental

Individual slices of MgO(001) were cleaved from blocks of single crystal material (Goodfellows, Cambridge) mounted on tantalum foil spot welded to a molybdenum stub and quickly introduced into the ESCALAB.

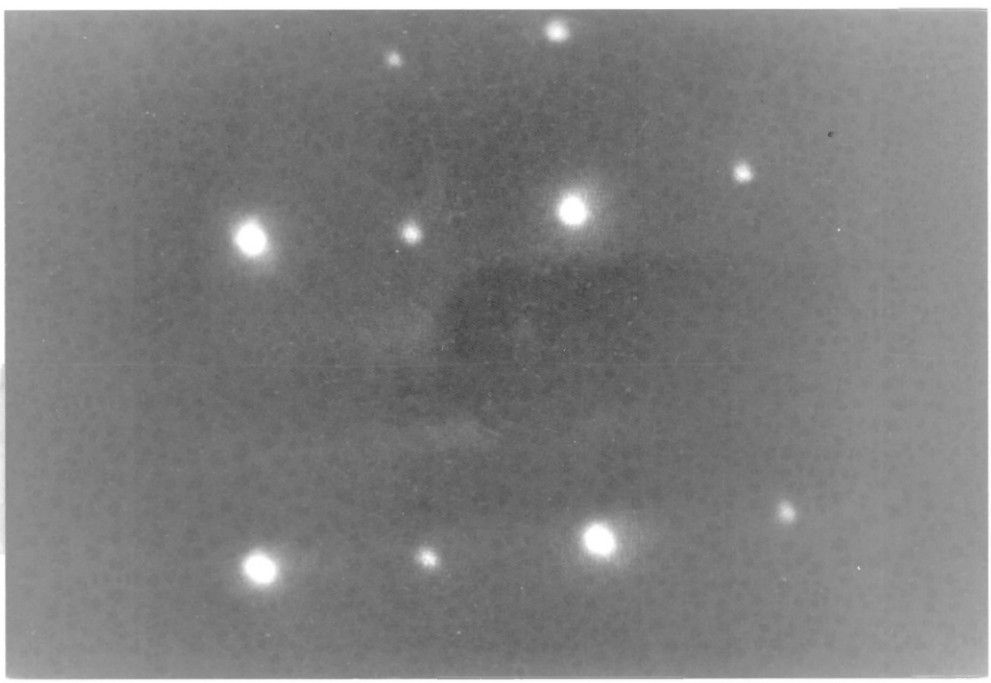
Three methods of in-situ cleaning were used namely; argon-ion etching, electron bombardment and RF heating. All removed contaminants from the surface whilst the latter two were effective in providing sufficient surface order to allow observation of sharp LEED patterns.

Electron beam fluxes of 25mA at 2.5KV flashed the crystal to temperatures in excess of 1200°C, although care had to be taken so as not to fracture the crystal. Typical resultant LEED can be seen in figure 4.2.

The RF method involved the heating of the tantalum holder as MgO is an insulator. Whilst this method is slightly slower in reaching temperatures in excess of 1200°C it has the advantage over the first method of not encouraging chamber outgassing and sample fracture. LEED patterns of the RF annealed crystal of an etched and unetched surface can be seen in figures 4.3 and 4.4.



(a)



(b)

Figure 4.2 LEED MgO(001) with electron bombardment to remove surface contamination. (a) 187eV beam energy (b) 141eV beam energy.

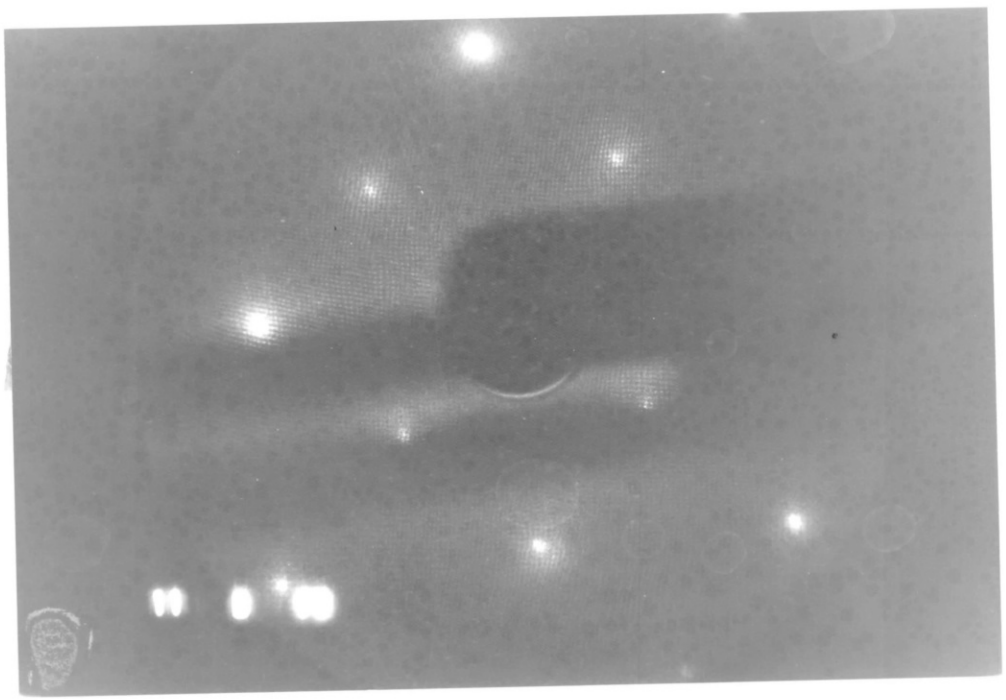
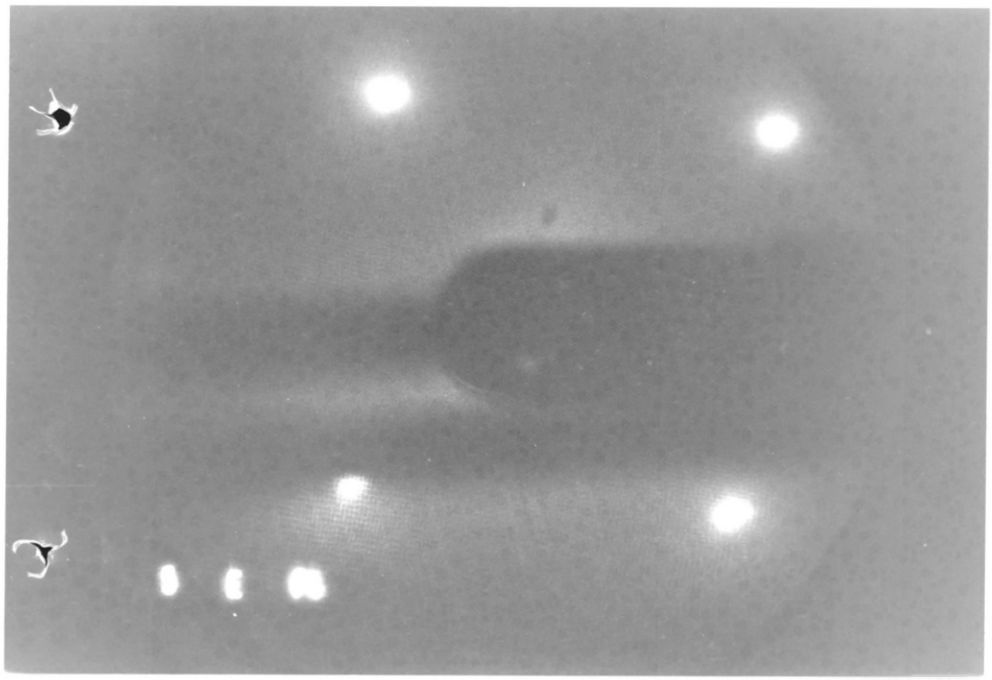
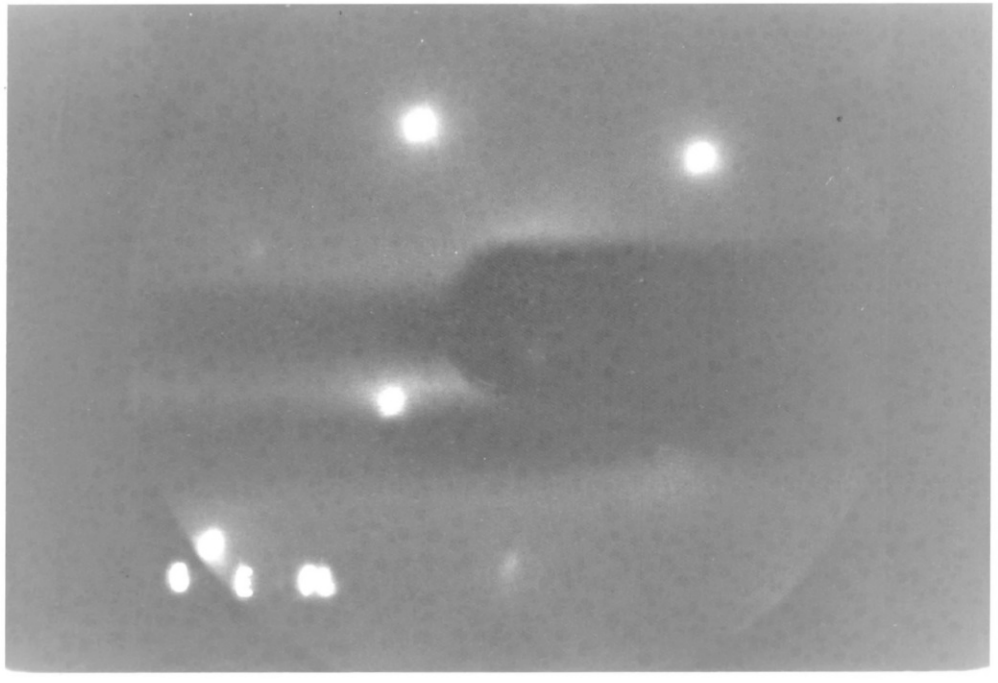


Figure 4.3 LEED MgO(001) with RF annealing after argon ion etching.



(a)



(b)

Figure 4.4 LEED MgO(001) with RF annealing only

(a) 56.8eV beam energy. (b) 100eV beam energy.

In figure 4.3 the crystal has been ion bombarded prior to R.F. annealing. The LEED patterns from both types of surface are of good quality, although the spots are generally sharper after RF heating alone.

Energy loss spectroscopy proved to be a useful adjunct to the other techniques in assessing surface quality. A typical energy loss spectrum is shown in figure 4.5. The spectrum is dominated by a surface exciton feature at 6.1eV, below the bulk bandgap of 7.7eV[21]. In addition our spectra invariably contained broad features at lower energy, extending down into the bulk bandgap. It is generally assumed that these latter features arise from interband processes at step sites where cation and anion coordination is reduced to a lower value (usually the number of near neighbours is 4) than that on Mg(100) terrace sites[22]. Thus ELS gives some indication that the MgO(100) surfaces are not perfect, although it is not possible to determine the step density.

4.3 XPS of MgO

Main features

Wide scan spectra of MgO(001) using both Mg:Kα and Al:Kα excitation can be seen in figure 4.6 .

The Al:Kα spectrum is dominated by the Mg:KLL auger structure which is expected to be absent under Mg:Kα excitation as the latter is insufficiently energetic to ionize the Mg:1s core level. However a well defined but

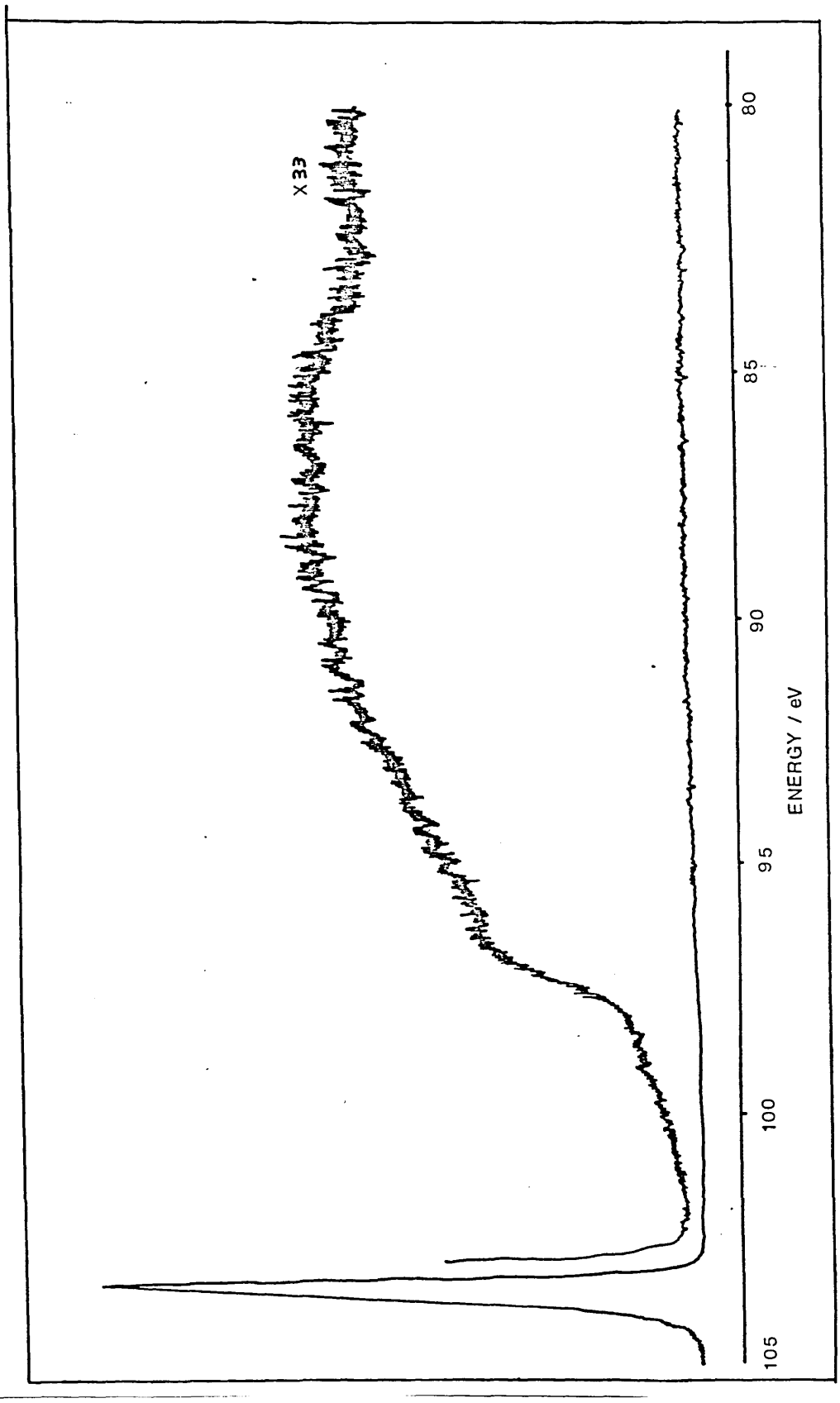


Figure 4.5 ELS spectrum of clean annealed MgO(001) excited at 100eV beam energy. Note the surface exciton feature at 6.1eV, below the bulk band gap of 7.7eV.

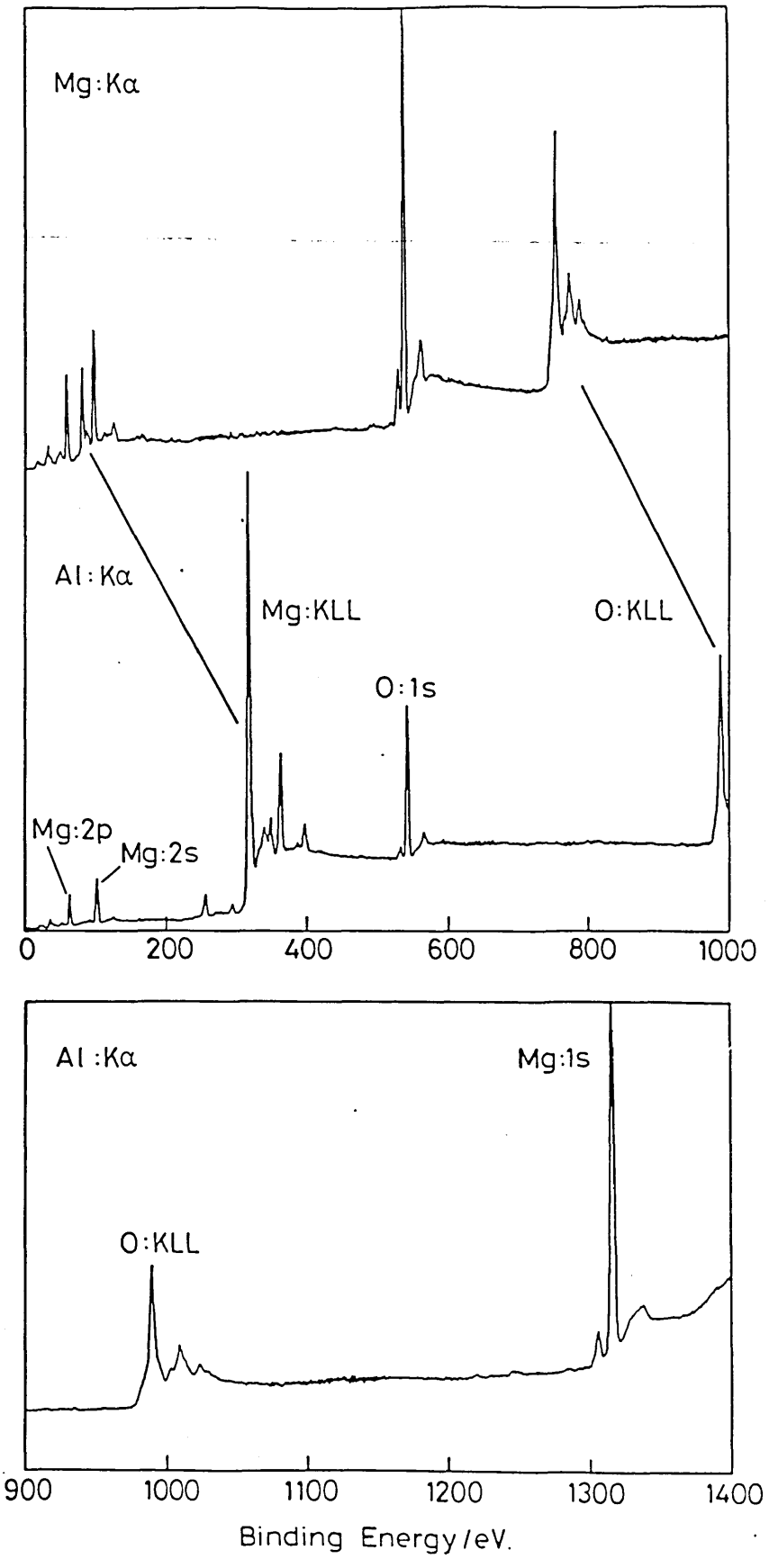


Figure 4.6 Wide scan spectra of MgO(001) using

(a) Mg:Kα and Al:Kα exciting radiation

(b) Al:Kα exciting radiation

weaker Mg:KLL feature is seen in the Mg:Kα spectrum. This must be attributed to the creation of Mg:1s core holes by background bremsstrahlung radiation from the Mg anode or to a small amount of Al:Kα impurity radiation due either to Al/Mg crossover or to the Al window. Expanded scans of the Mg:KLL and O:KLL Auger structure are shown in figure 4.7 .

Finally, figure 4.8 shows scans of the O:1s and Mg:1s core levels and associated satellite structure, whilst figure 4.9 shows expanded scans of the principal Mg core lines (2p, 2s and 1s).

Satellite structure

As can be seen in figure 4.8 , the dominant O:1s and Mg:1s core levels show strong satellite structure to lower binding energy. The main O:1s satellite is 22.8eV below the core peak, overlapped by a broad weaker feature estimated to be centred at about 16eV. The Mg:1s satellite structure shows similar features at 22.1eV and 17.6eV together with an additional feature at a lower energy around 11.7eV .

The satellite structure is strongly reminiscent of that found for Al_2O_3 by Gignac and co-workers[23] . These authors attempted to rationalize XPS satellites and loss structure in ELS mainly in terms of interband excitations, but we prefer an interpretation in terms of plasmon and excitonic features.

With simple expressions of Szajman and Leckey[24] we estimate that, with due allowance for the MgO bandgap, the

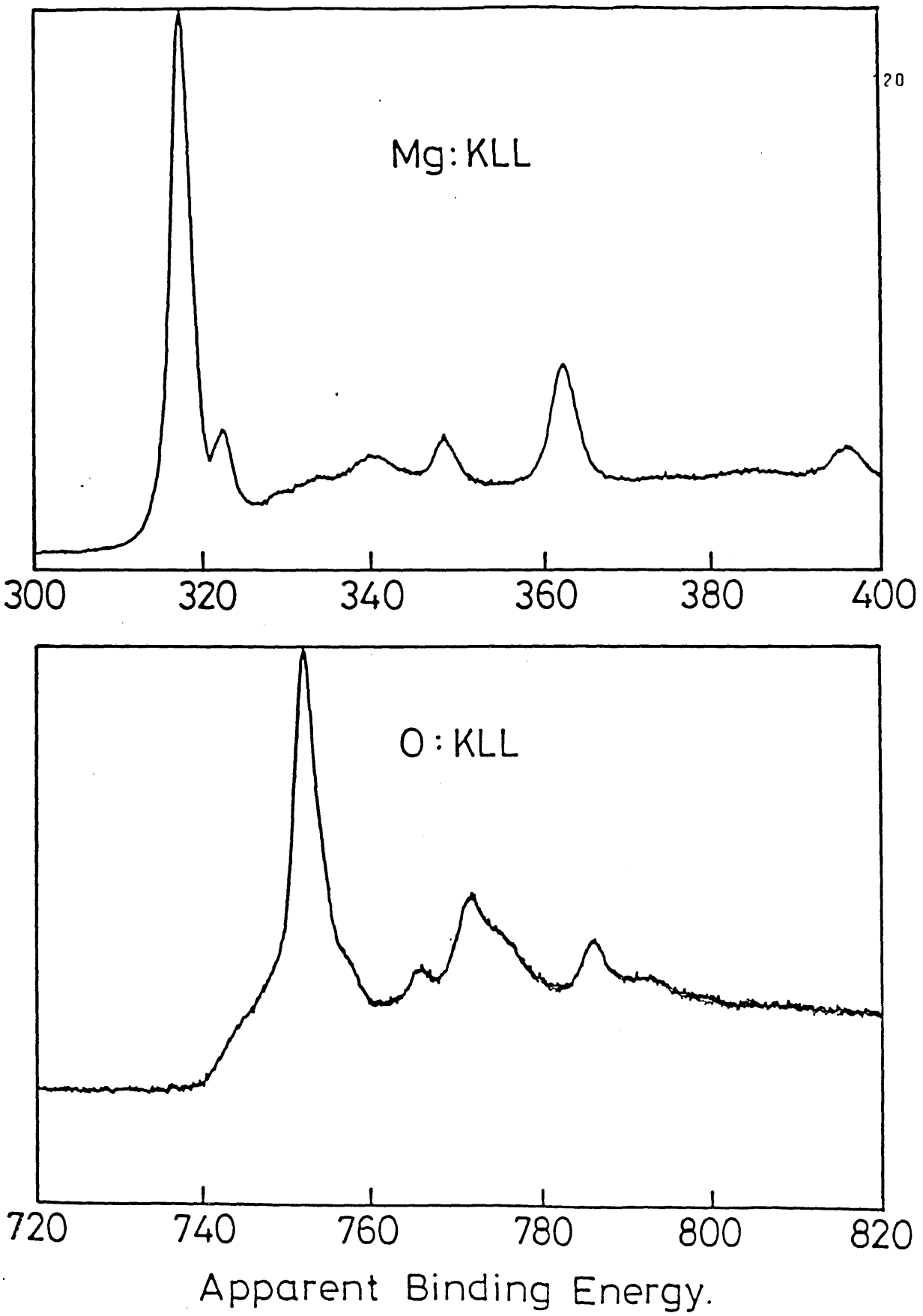


Figure 4.7 Al:Kα excited Auger spectra of MgO(001).

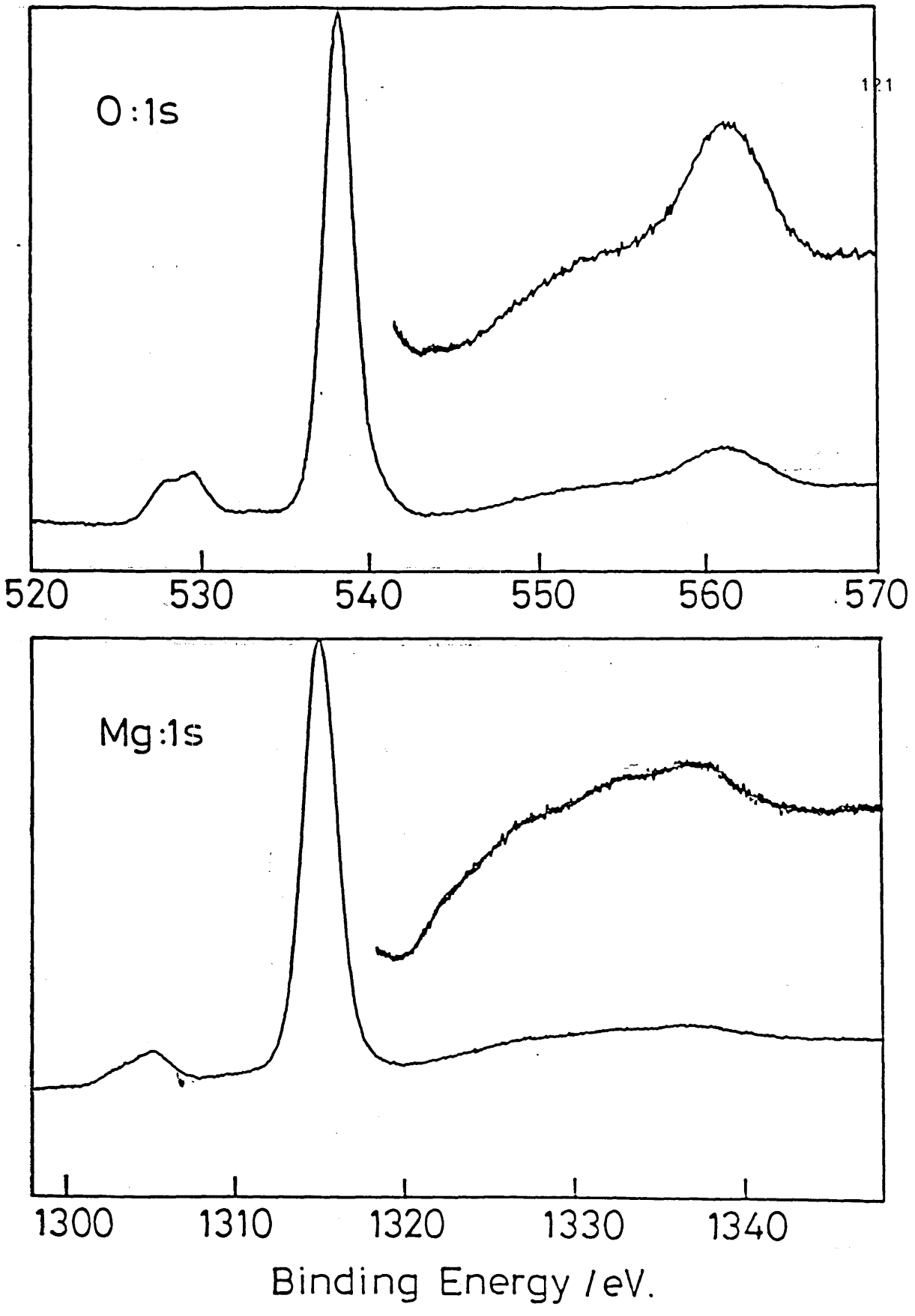


Figure 4.8 Narrow scan XPS spectra of O:1s and Mg:1s core levels and associated satellite structure.

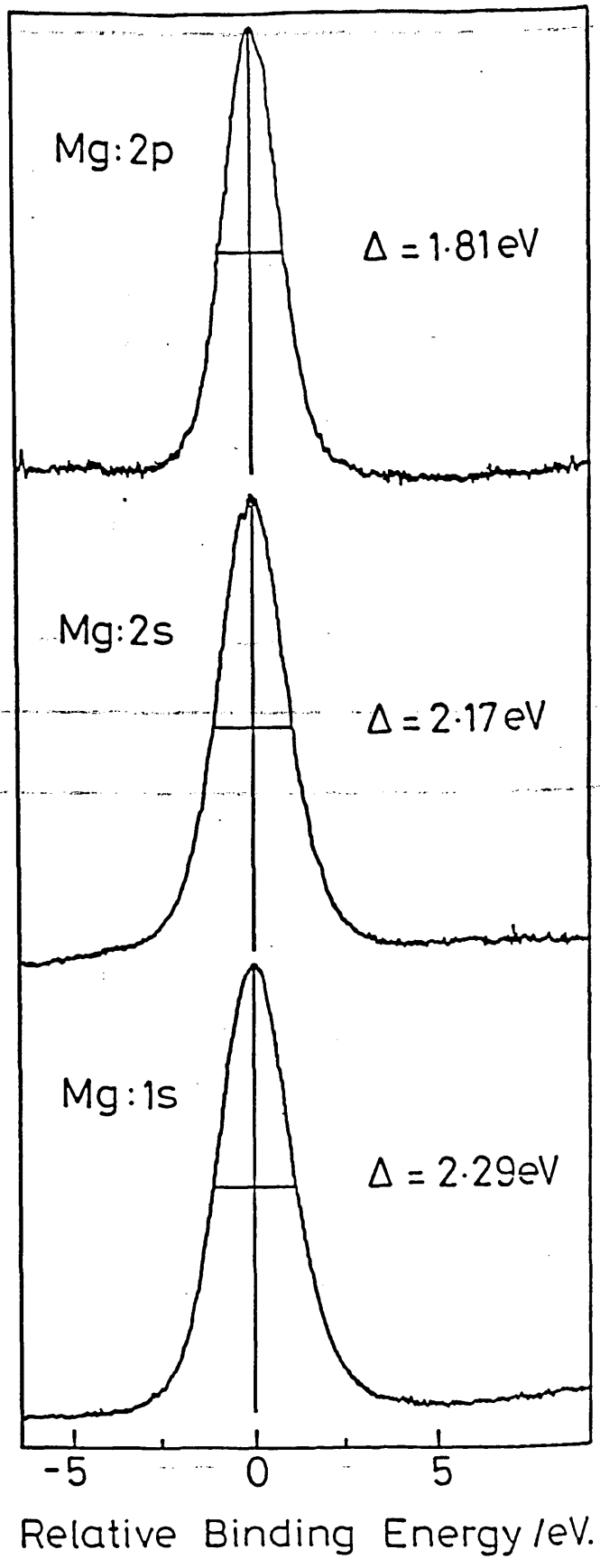


Figure 4.9 Narrow scan XPS spectra of the principal Mg core lines and their FWHM excited with Al:Kα and at 20eV analyser energy.

valence electrons is 22.3eV and the corresponding surface plasmon is 15.8eV. These energies are very close to the O:1s satellite energies mentioned above. The strength of the plasmon loss may be associated with an "intrinsic" mechanism for plasmon excitation associated with the fact that the electron density responsible for the plasma excitation resides predominantly on the oxygen atoms (as we are dealing with an ionic solid). The additional low energy satellite structure associated with the Mg:1s core line is presumed to be similar in origin to satellite structure for ZrO_2 and Y_2O_3 discussed in chapter 3. This depends on polarisation of oxygen valence electron density by the photohole[25]. Owing to the much lower polarisability of Mg^{2+} and the absence of suitably occupied ground state orbitals this mechanism is not available for satellite creation as a result of O:1s photoionization.

The widths of core lines in XPS of MgO

In photoemission experiments the widths of corelines from most compounds of a metal are considerably larger than those of the pure metal. The core lines in figure 4.8 and 4.9 are considerably broader than the corresponding core lines from Mg metal[26]. The widths of core lines in XPS of insulators have been found to conform to a general pattern[27,28,29,30] a major contribution[28] to this broadening coming from phonon effects. It is therefore appropriate here to estimate the likely phonon broadening of

core lines in MgO.

Ionization of a core level in an insulator produces a positively charged defect which initially causes the surrounding ions to be in a state of non-equilibrium. The ions cannot relax their positions on the timescale of the photoemission process, although electronic polarisation of the surrounding medium is possible due to the induced field caused by the creation of the core-hole[31]. In a simple continuum model it is possible to estimate the difference between the vertical and the ionically relaxed configuration as Er, where in atomic units (bohr radii)

$$Er = (6 / \pi V)^{1/3} (1/\varepsilon_\infty - 1/\varepsilon_o) \quad ....4.1$$

Where V is the volume of the primitive unit cell and ε_∞ and ε_o are the high and low frequency dielectric constants.

For MgO , $\varepsilon_\infty = 2.95$, $\varepsilon_o = 9.86$ and $V^{1/3} = 2.106$Å, so that we can estimate Er = 2.014eV.

Alternatively, Mackrodt[32] has calculated the energies of O^- and Mg^{3+} defects in MgO, using the shell model[33] to allow for anion polarizability. In this model differences in electronic and ionic relaxation for the two different types of ionic site are explicitly introduced, and Er appears as the difference between electronically and ionically relaxed energies.

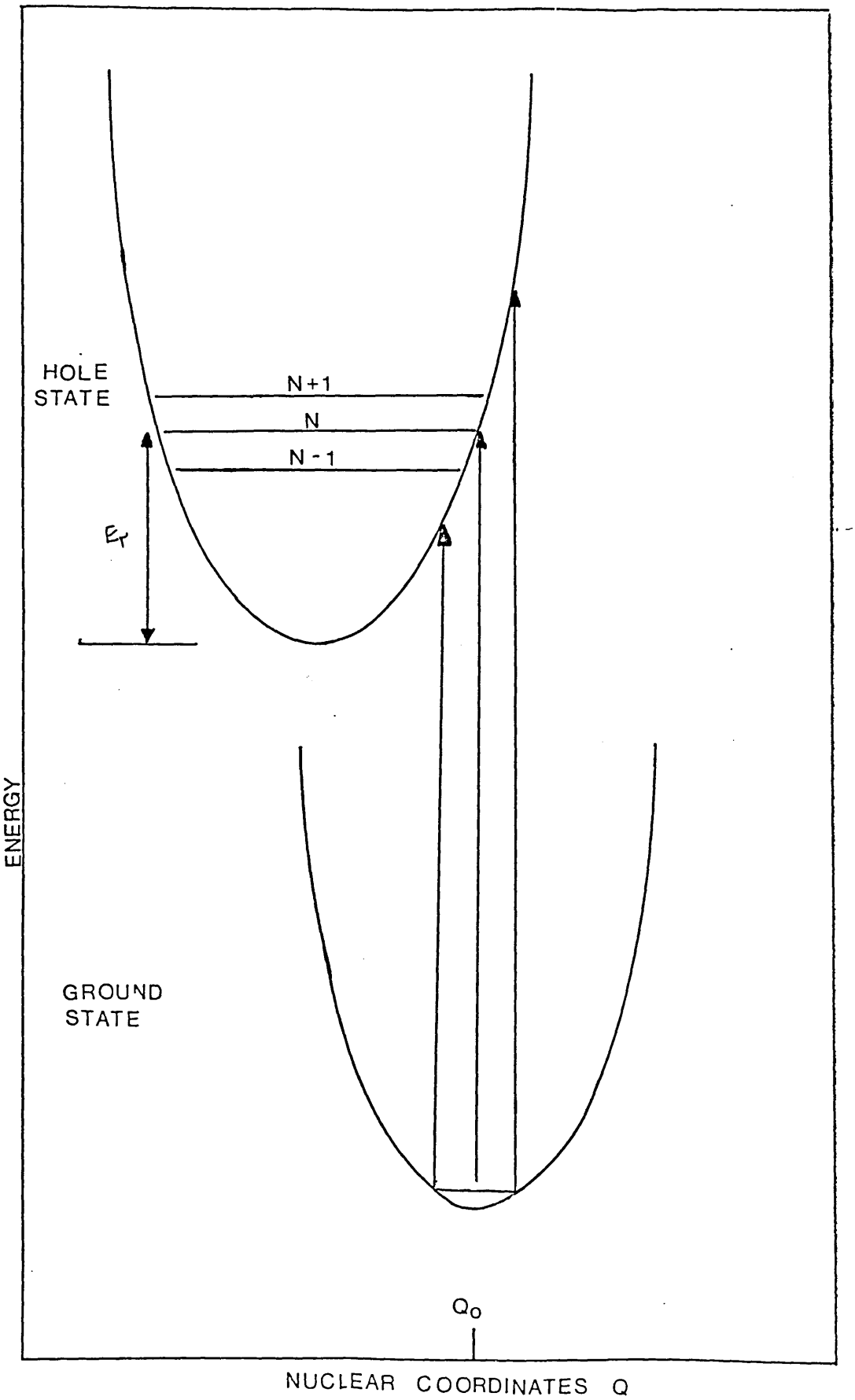


Figure 4.10 Diagram showing the origin of the thermal broadening of core lines. E_r is the vibrational relaxation energy.

3 Defect energies (eV) of O^- and Mg^{3+} in MgO[32]

	Unrelaxed	electronically relaxed	ionically relaxed	Er
O^-	22.7836898	20.8889876	17.9768946	2.192093
Mg^{3+}	-23.56525270	-27.070209	-28.58500266	1.514793

There is a bigger final state relaxation energy associated with ionization of O core levels than Mg core levels. This is due to the larger screening of Mg^{3+} defects by electronic polarisation equal to -3.504957eV, as compared with the screening of O^- defects with only -1.894702eV. This in turn reflects the fact that Mg is surrounded by six highly polarisable O^{2-} ions, whereas O^{2-} is surrounded by non-polarisable Mg^{2+} ions. Note that the average relaxation energy from the macroscopic calculations is 1.853eV, reasonably close to the value from the continuum model.

Since the vertical final state configuration does not represent an equilibrium configuration of the system, figure 4.10, phonons are excited over a wide energy range with intensities determined by Franck-Condon factors. Individual phonon lines are not resolved, but instead one observes a Gaussian broadened core-level line with a phonon broadening Γ given in electron volts[29] by:

$$\Gamma_{phonon} = 2.35(\hbar \omega_{MO} \, Fr \coth(\hbar\omega_{LO} / 2kT))^{1/2} \quad ....4.2$$

(LO is longitudinal optical)

where ω_{LO} is the frequency of LO phonons coupling to the

photohole. $\hbar\omega_{LO}$ may be estimated from the Lyddane-Jachs-Teller relationship[34] :

$$\omega_{LO} / \omega_{TO} = (\varepsilon_o / \varepsilon_\infty)^{1/2} \quad ....4.3$$

with $\hbar\omega_{TO}$ = eV , this gives $\hbar\omega_{LO}$ = 0.088eV

We thus estimate the following phonon broadenings

Γ (continuum) = 1.02eV

Γ (Mg corehole) = 0.885eV

Γ (O core hole) = 1.23eV

Assuming Gaussian contributions to the broadening from the analyser and photon sources we can write:

$$\Gamma_{est}^2 = \Gamma^2_{phonon} + \Gamma^2_{anal} + \Gamma^2_{photon} \quad ....4.4$$

With Al:kα radiation , Γ_{anal} = 0.4eV and Γ_{photon} = 0.85eV, we have:

Γ_{est} (continuum) = 1.39eV

Γ_{est} (O:1s) = 1.55eV

Γ_{est} (Mg core) = 1.29eV

(Experiments were conducted at 20eV pass energy which gives Γ_{anal} = (20x0.6)/(2x150) eV = 0.40 eV.)

With Mg:Kα radiation Γ_{photon} = 0.7 eV giving:

Γ_{est} (continuum) = 1.30eV

Γ_{est} (O:1s) = 1.47eV

Γ_{est} (Mg core) = 1.19eV

The observed O:1s linewidth of 1.65eV with Al:Kα excitation is in remarkedly good agreement with the estimate, showing that lifetime broadening is only of minor importance. By contrast both Mg:1s and Mg:2s core levels are appreciably broader than expected probably due to lifetime broadening effects. The Mg:2p level would not be expected to show marked lifetime broadening as it can decay only by interatomic processes. The fact that its width is greater than that of the O:1s line is probably due to unresolved spin orbit splitting into $2p_{3/2}$ and $2p_{1/2}$ components. Thus we are unable to find direct experimental verification of the prediction that Mg core lines should show less phonon broadening than O core lines.

4.4 The surface-core shift

As discussed in section 4.1, differences between Madelung potentials at bulk and surface sites in MgO might be expected to produce a discernable SCS. Mackrodt has estimated[35] that the Madelung potential in the surface plane of MgO(100) differs by ± 0.876eV from the bulk potential for both cation and anion sites. At the relaxed surface, the O^{2-} ions are displaced outwards relative to Mg^{2+} cations, so screening them slightly from the vacuum.

Hence at the relaxed surface, the SCS for Mg^{2+} cation sites decreases to +0.554eV, but for the anion sites it increases to 1.136eV.

We attempted to observe SCS for both Mg:1s and O:1s core lines, comparing normal and grazing (15°) emission spectra. Initially it was thought that the excellent sensitivity associated with Mg:1s might allow us to see the SCS, but the large lifetime broadening of the Mg:1s line (Γ_{obs} = 2.29eV) works against this possibility. In fact there are no obvious differences between normal and grazing lines despite the fact that the surface/bulk contribution to the Mg:1s emission is expected to change from 2.43 to 33.3 in going from 90° to 15° emission.

The narrower width of the O:1s line led us to treat O:1s data in greater detail. On going from 90° to 15° emission, the surface/bulk contribution is expected to shift from 1.27 to 2.59. We have simulated the change by adding gaussians with Γ_{obs} = 1.65 eV shifted relative to each other by 1.1eV in the relevant proportions for 90° and 15° emission. The photoemission profile at 15° is expected to show a pronounced assymetry to the low BE side; and an overall increase in FWHM. Experimentally a small broadening in the photoemission profile is observed (figure 4.11) but is less pronounced than expected. It is unwise to pursue analysis of our data too far since we are limited by a software determined spacing between data points in XPS of only 0.1eV.

However it does appear that the SCS must be less than

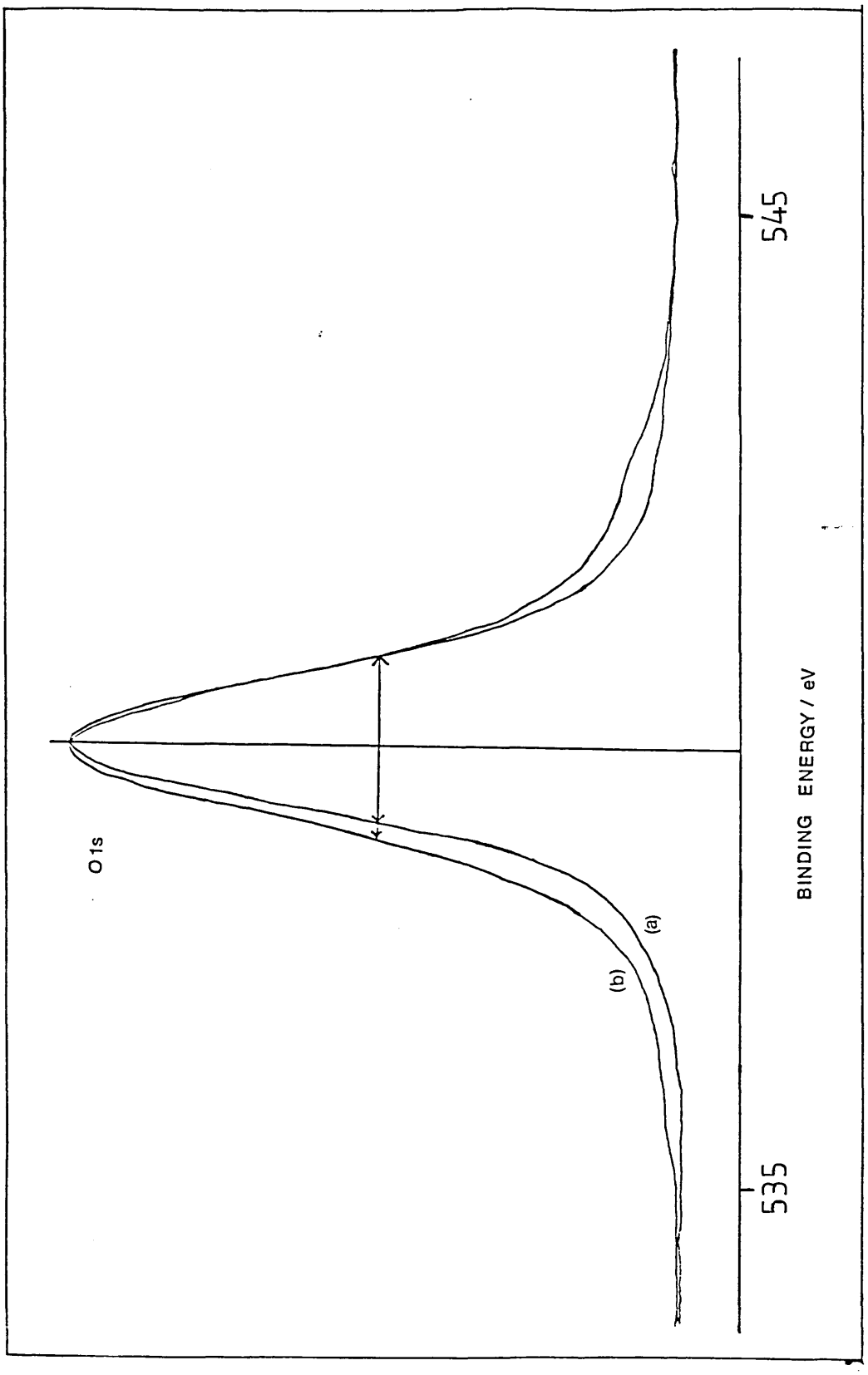


Figure 4.11 O1s XPS spectra of clean annealed MgO(001) at (a) 90° and (b) 15° angle of emission. Note the slight broadening with change of angle.

However it does appear that the SCS must be less than that expected from Madelung potentials. Two factors may play a part in this finding namely:

(a) There could be a noticeable difference between bulk and and surface core site polarisation energies. However the theory that suggests that the long range contributions from surface and bulk cannot differ[7], so the difference must be due to short range effects.

(b) Rieder[36] suggests that his results involving helium diffraction on MgO(100) indicate a change in ionicity at the surface although this idea is in marked contrast to the theoretical considerations of Causa et al[1]. Helium diffraction studies can examine the change in the "rumpling" shown in an electron density contour map, which in turn would be affected by a change in ionicity.

Further experimental work on MgO using syncrotron radiation tuned to give enhanced surface sensitivity is highly desirable.

Chapter 5. Growth of BaO layers on MgO{001}

5.1 Introduction

As previously discussed, MgO (100) has a simple termination of the bulk structure with a very small relaxation of the surface ions away from their bulk positions. This is demonstrated both by careful LEED[1] studies and theoretically via atomistic simulations[2], showing that the outward rumpling of O^{2-} anions relative to the Mg^{2+} cations is only of the order of 0.05Å. This situation does change however when MgO is doped with large isovalent ions such as Ca^{2+}, Sr^{2+} and Ba^{2+}. The strain induced in the lattice is concomitant with a large heat of segregation, as shown by the experimental work with Ca^{2+} segregation to MgO(001) by Wynblatt[5] and the theoretical simulation of the same system by Mackrodt et al[3][4]. The close agreement between these two findings strengthens the arguments for the case that the strain of the lattice can be relieved if the large ion is removed to a surface site. Thus significant concentrations of large dopant ions accumulate at the MgO(001) surface, and these ions cannot be incorporated into an unrelaxed structure.

In particular Mackrodt and coworkers suggest that a monolayer of BaO on MgO can be accomodated by the displacement of alternative Ba ions above and below a plane containing equivalent O ions occurs, producing a $\sqrt{2}\times\sqrt{2}$ superstructure in the surface unit cell. However the calculated structure is sensitive to the interionic potentials used in the simulation and the $\sqrt{2}\times\sqrt{2}$ monolayer

was derived from rather crude potentials that ignore polarizability of the Ba^{2+} ions. When allowance was made for cation polarizibility a more complex ? x ? structure was obtained. It was against this background that we decided to study the deposition of BaO onto MgO(001) in relation to the theoretical predictions, with the specific aim of observing the predicted superstructures. Rather than rely on segregation of BaO out of the bulk MgO, we chose to deposit BaO onto the MgO surface.

With overlayer studies, a surface-sensitive electron spectroscopic technique usually XPS, AFS or ELS is used to follow simultaneously the signals arising from both the substrate and the overlayer as deposition proceeds. The plots of signal intensity versus deposition time can be used identify the growth mode of the system and possibly enable an absolute coverage calibration to be made[6]. This method of calibration is based on the principle that each atomic layer of the overlayer will attenuate both overlayer and substrate signals ar ising from lower atomic layers. The inherent difficulties with overlayer quantifications are discussed in section 5.3.

LEED initially provides a qualitative means of assessing whether the overlayers are ordered or not. Quantitative analysis of spot positions enables one to measure the size of the surface unit cell in the overlayer[7]. ELS is probably more surface sensitive than XPS and it provides a means of studying electronic stucture of the overlayer in terms of plasmons and interband

excitations of the overlayer[8]. Even at moderate beam energies ELS is applicable to insulators, unlike UPS.

It is our belief that the method employed here for epitaxial growth has not been used previously. It involves the deposition of a metal from a getter source, subsequent oxidation using oxygen gas and then high temperature annealing using RF power. This in situ method may possibly be used for preparation of other highly reactive oxides similar to BaO.

The system we have chosen to study has several favourable characteristics:

(1) The Ba^{2+} ion has a large heat of segregation[9] to the the surface of MgO(100) and is unlikely to diffuse into the bulk.

(2) Ba oxidises very easily as indicated by its use as a getter source[10].

(3) The $Ba3d_{5/2}$ peak in XPS has a large photoionisation cross section[11] and therefore Ba is easily detected even in submonolayer concentrations on the MgO surface.

5.2 Experimental

5.2.1MgO crystal preparation

The MgO crystal slices were prepared and mounted as in chapter 4.

5.2.2 The Ba Evaporator

Barium metal was deposited onto the ambient temperature

MgO surfaces from a shrouded $BaAl_4$ getter source (SAES Getters, Milan Italy) held 2cm above the substrate. The evaporator is shown schematically in figure 5.1. The getter source was spot welded to tungsten rods which were in turn spot welded to the UHV feedthrough. The getter temperature was measured by a chromel-alumel or tungsten-rhenium thermocouple spot-welded near to one leg. Before use getters were carefully degassed and the evaporation characteristics of individual getters had to be established by slowly increasing the current passed through the getter until a measurable Ba:3d peak was found in the XPS spectrum. Each getter once initialised gave a smooth deposition of barium if held at constant temperature[12]. Usually a current of around 3A was needed to outgas the evaporator and 6A to 7A was needed to evaporate barium metal at a suitable rate. The evaporation was controlled by the getter temperature at about 920K, which could be held stable for a given source to ± 4°C . The evaporation rate, of approximately 0.05 monolayers per minute, only changed markedly towards the end of the getters lifetime and did so very rapidly, signalling the end of an experimental run.

In previous work involving the evaporation of alkali metals from a getter source[12] special attention was paid to oxygen outgassing of the metal surround. In this work no significant change in the background oxygen signal was observed using quadrupole mass spectroscopy throughout the metal deposition.

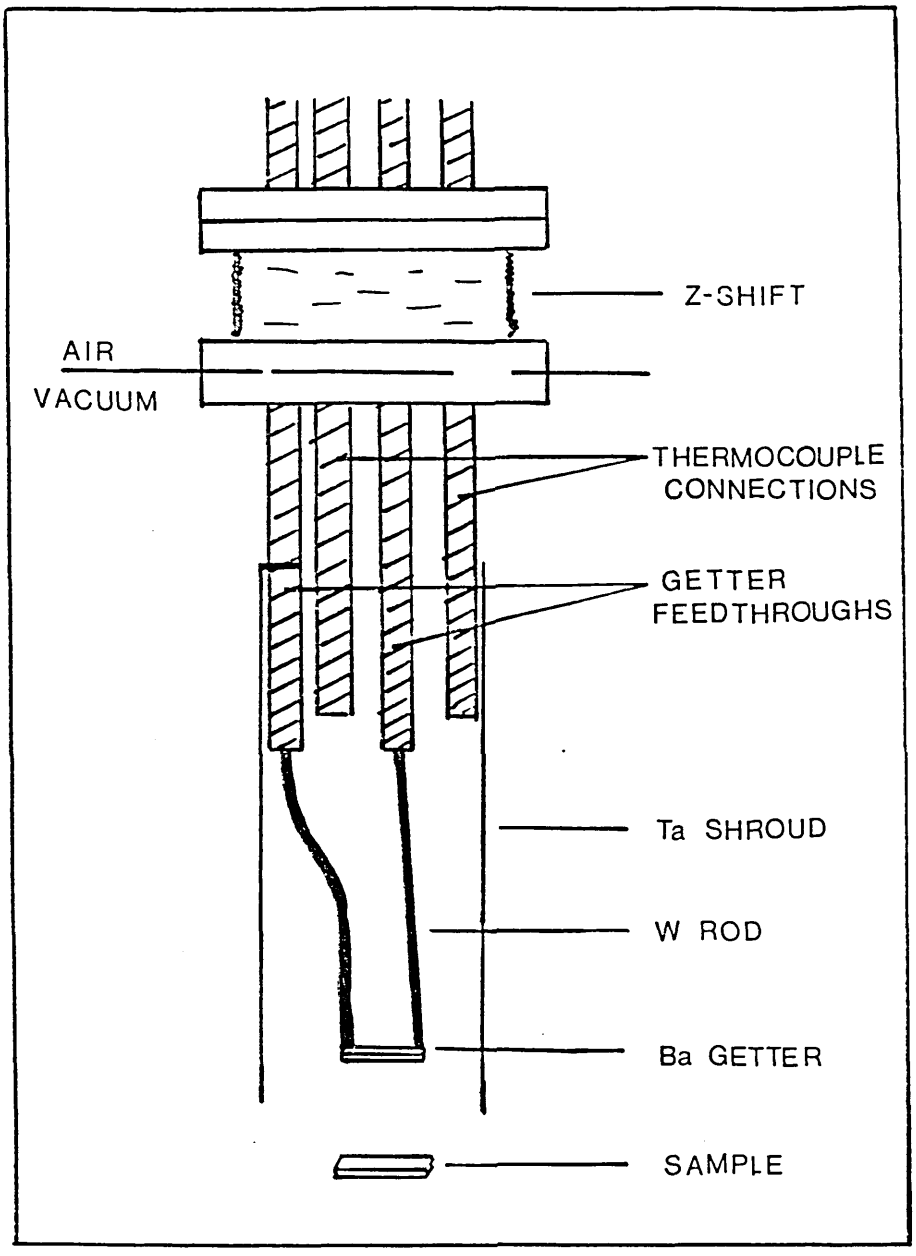


Figure 5.1 Diagram of the barium getter source. Current was passed through the getter via two of the four feedthroughs and the temperature measured by the remaining two with a thermocouple

5.2.3 R.F. heating/annealing

The MgO crystals were cleaned and annealed by heating the underlying Ta sheets to temperatures in excess of 1500K for periods of at least 10 minutes. The annealing and ordering of the surface was monitored by XPS and LEED. Prior to evaporation the LEED spots were very sharp, very intense and gave the lattice parameter of MgO bulk to within a percent. C1s, or other impurity peaks, could not be seen in the XPS spectrum of the MgO crystal surface.

Whilst annealing the crystal after barium deposition it was necessary to establish conditions where no loss of the overlayer was occurring and where we were obtaining an ordered structure. This was achieved by tentative heating to "red heat" and checking the XPS spectrum when an ordered overlayer was obtained shown by LEED. No extensive interdiffusion of Ba^{2+} occured during the overlayer studies, even during extensive high temperature heating at 1200K where some loss of Ba into the chamber occured. This was checked by XPS following light argon bombardment, giving MgO substrate signal only.

5.2.4 Oxygen dosing

The oxygen was admitted through a leak valve into the preparation chamber after the barium evaporation. The purity of the gas was monitored by quadrupole mass spectroscopy, and the XPS spectrum of the resultant overlayer. The dose was usually 300L at 10^{-6}torr of oxygen

which proved to be well in excess of that needed to oxidise all the barium metal.

5.2.5 Experimental flow chart

The experimental method is shown by a flow chart in figure 5.2. Section (1) is the initial cleaning, section (2) is the cyclic mode of evaporation and section (3) the annealing of the ordered overlayer.

It was also necessary for the XPS quantification to prepare a BaO overlayer that was thick enough to represent bulk BaO. This was done by repetition of cycle (3) in the flow chart until the MgO signal was completely attenuated.

5.3 XPS results

5.3.1 XPS of Ba metal (only) growth on MgO(100)

In order to help establish the characteristics of the getter sources preliminary work involved deposition of Ba metal onto MgO(001). The metal was deposited in stages onto a clean, annealed and ordered substrate. The $Ba3d_{5/2}$ / Mg1s ratio was monitored as a function of evaporation time as shown in figure 5.3 for a typical run. The coverage ranges from submonolayer to about four monolayers. The smooth, continuous curve probably indicates a three dimensional nucleation of the overlayer without monolayer formation.[13]

5.3.2 XPS of epitaxial growth of BaO on MgO

XPS was mainly used for two purposes during the growth of BaO firstly to check the effect of annealing on the

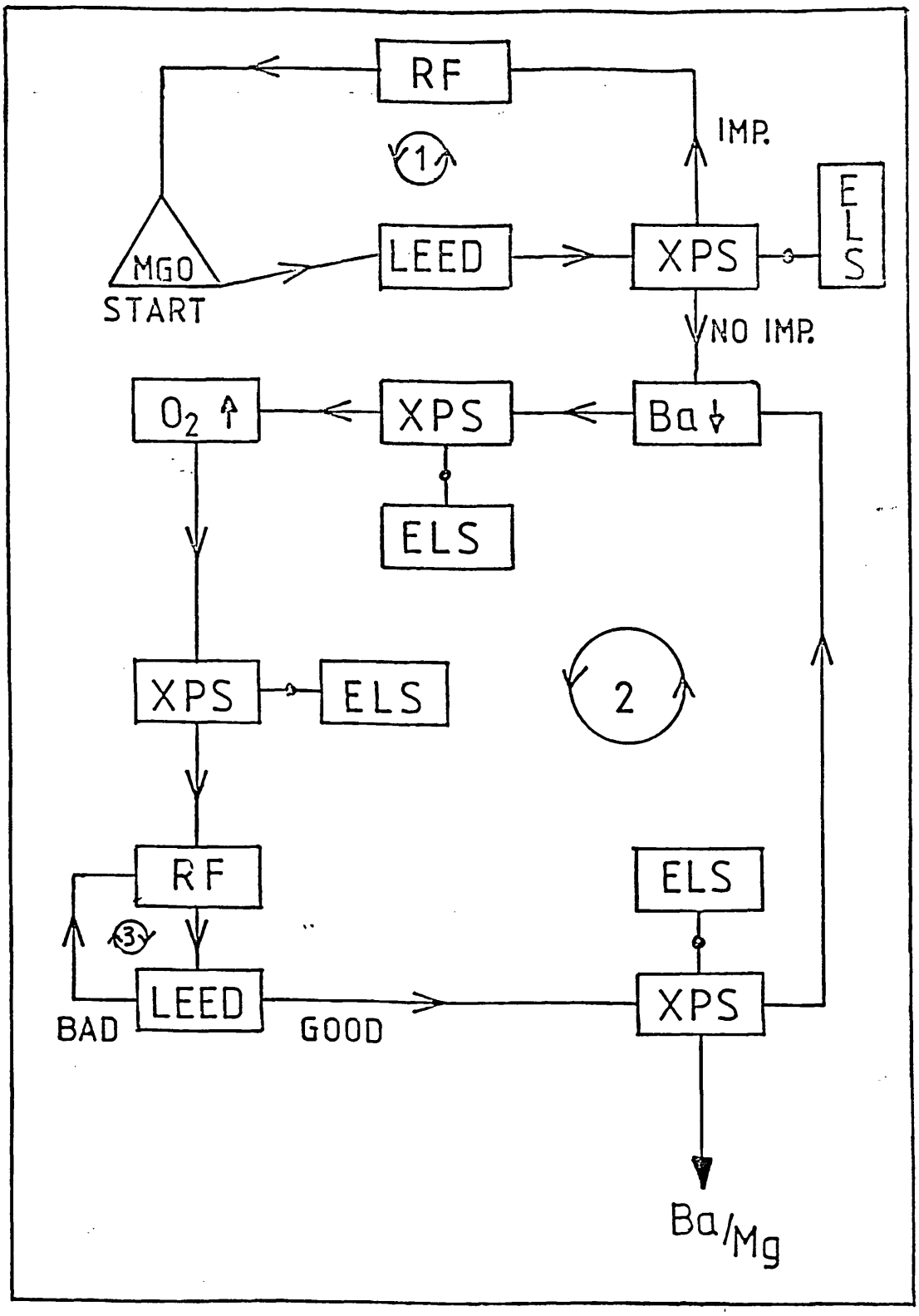


Figure 5.2 Experimental flow chart of BaO growth. Section (1) is the initial cleaning section, section (2) is the cyclic mode of evapo ration and section (3) the annealing of the ordered overlayer.

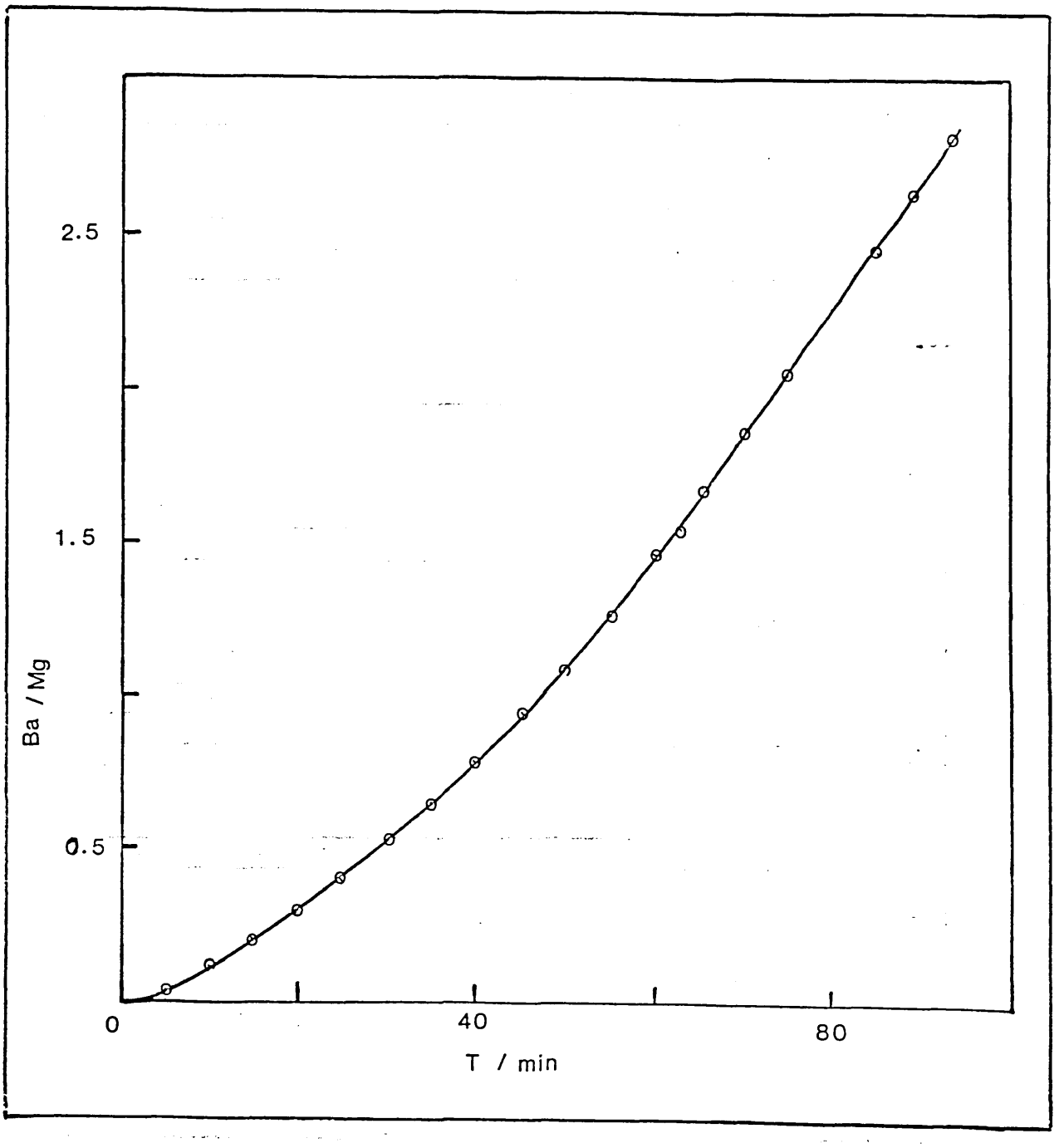


Figure 5.3 Ratio of Ba:$3d_{5/2}$ / Mg:1s monitored as a function of evaporation time during a typical growth run.

amounts of BaO put down, and secondly to monitor the $Ba3d_{5/2}$ / Mg1s ratio corresponding to the various LFFD patterns observed.

Figure 5.4 shows the widescan Al:Kα excited spectrum of (a) Clean MgO(001) and (b) The BaO overlayer at about four monolayers thick. Peaks marked with an asterisk are due to Mg:Kα and Cu:Kα impurity radiation. Note the marked attenuation of the MgO features in 5.4(b).

Figure 5.5 shows the relative increase in the intensity of the Ba:3d peak as a function of deposition time in conjunction with figure 5.3. Figures 5.6 and 5.7 show the O:1s core level during BaO growth with figure 5.6 showing the O:1s core level structure at normal emission as a function of increased BaO coverage. The $Ba:3d_{5/2}$ / Mg:1s intensity ratios corresponding to the spectra are shown in the caption. The high BF component to the O:1s peak grows up with BaO deposition with the pronounced effect of the overlayer being further demonstrated by angle resoved XPS. Figure 5.7 shows the O:1s XPS of clean MgO, MgO with the BaO overlayer at about four monolayers coverage, and the latter at 15° angle of emission showing the stronger BaO type O:1s signal at smaller emission angle.

Two details of the XPS show that there is no extensive interdiffusion to produce a homogenous solid solution whose thickness is large compared to the pathlengths of the photoionised electrons. Firstly the Mg2p/Mg1s intensity ratio in the AlKα XPS increases from its value of 0.05 for

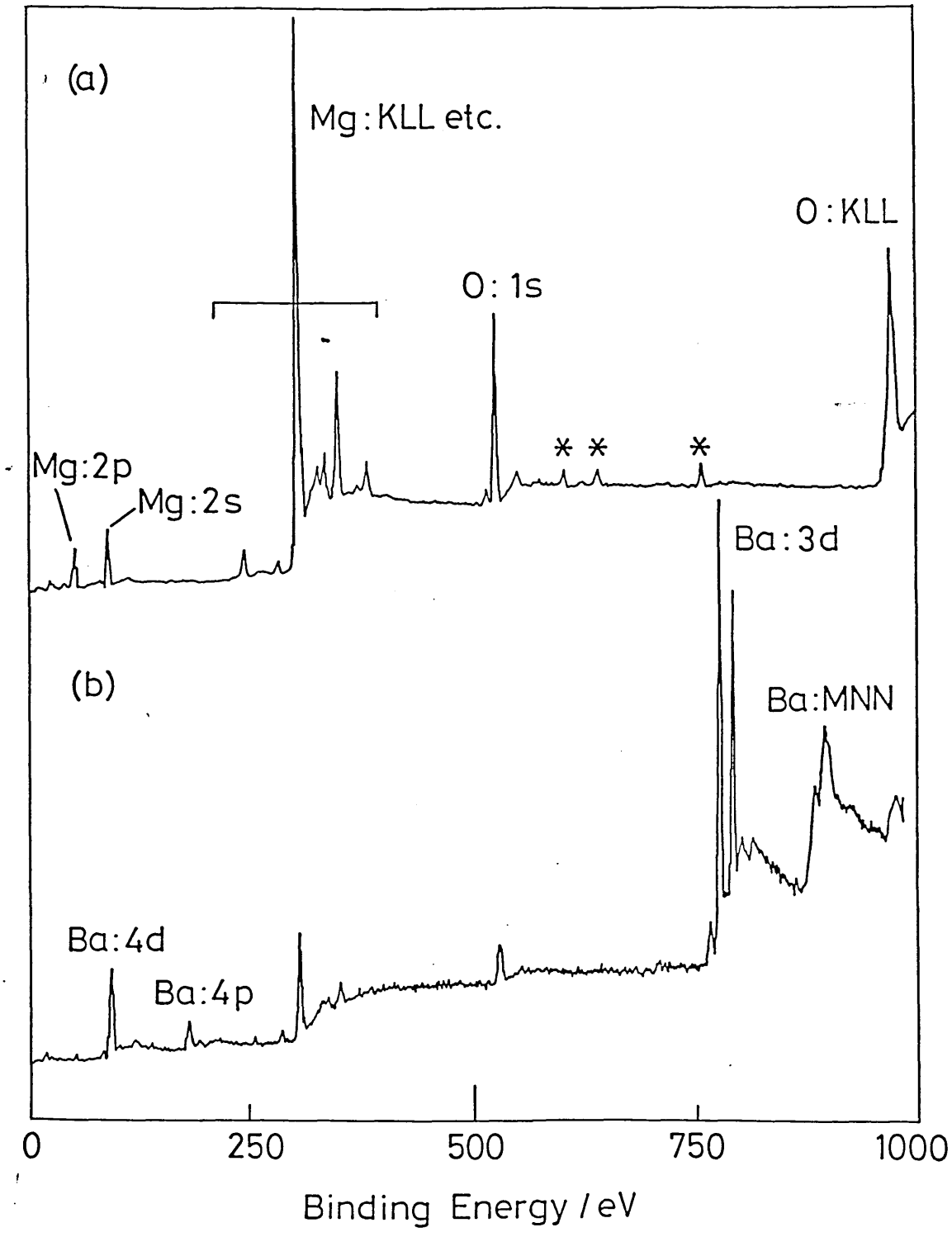


Figure 5.4 Widescan Al:Kα excited XPS of (a) clean MgO(001) (b) BaO overlayer about 4 monolayers thick. Peaks marked with * are due to Mg:Kα and Cu:Kα impurity radiation.

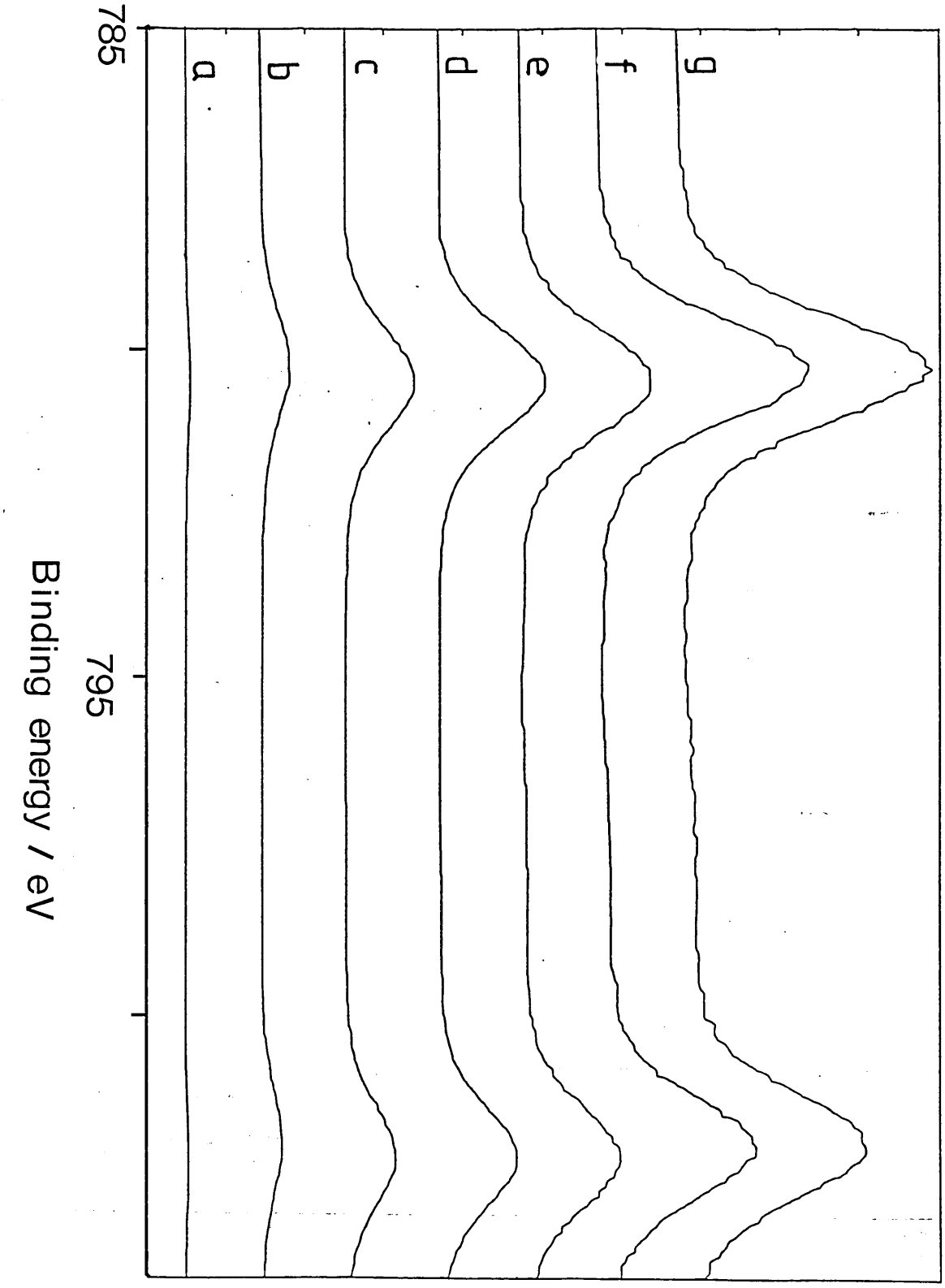


Figure 5.5 Ba:3d core level spectra showing the relative increase in the intensity with deposition time in conjunction with figure 5.3. a is after 5 minutes going to g after 65 minutes in 10 minute increments.

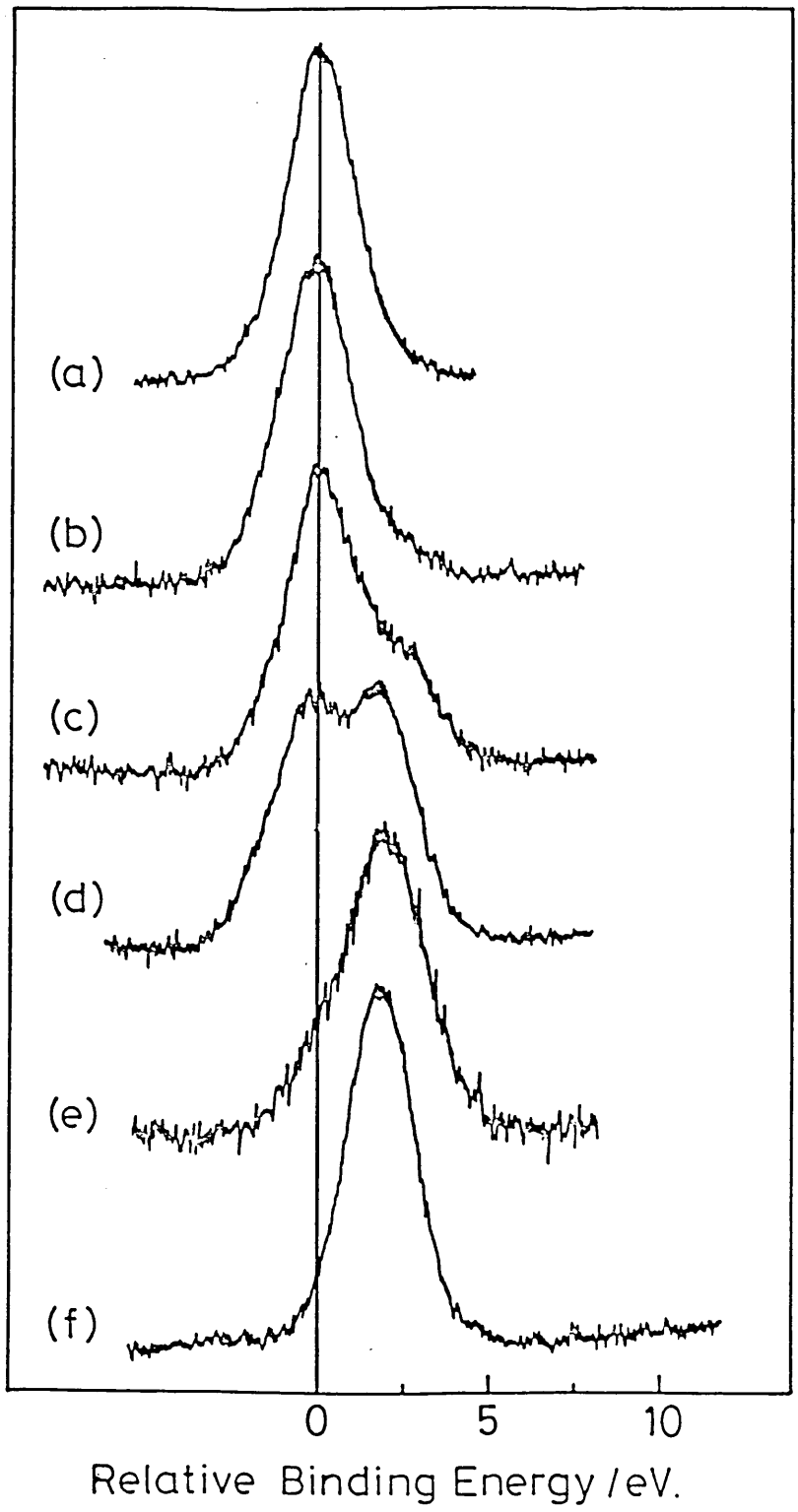


Figure 5.6 O:1s core level structure in Al:Kα XPS at normal emission as a function of increasing BaO coverage. The Ba:$3d_{5/2}$/Mg:1s intensity ratios corresponding to the spectra are as follows: (a) 0 (b) 1.7 (c) 4.5 (d) 23.8 (e) > 100 (f) Mg:1s peak not visible

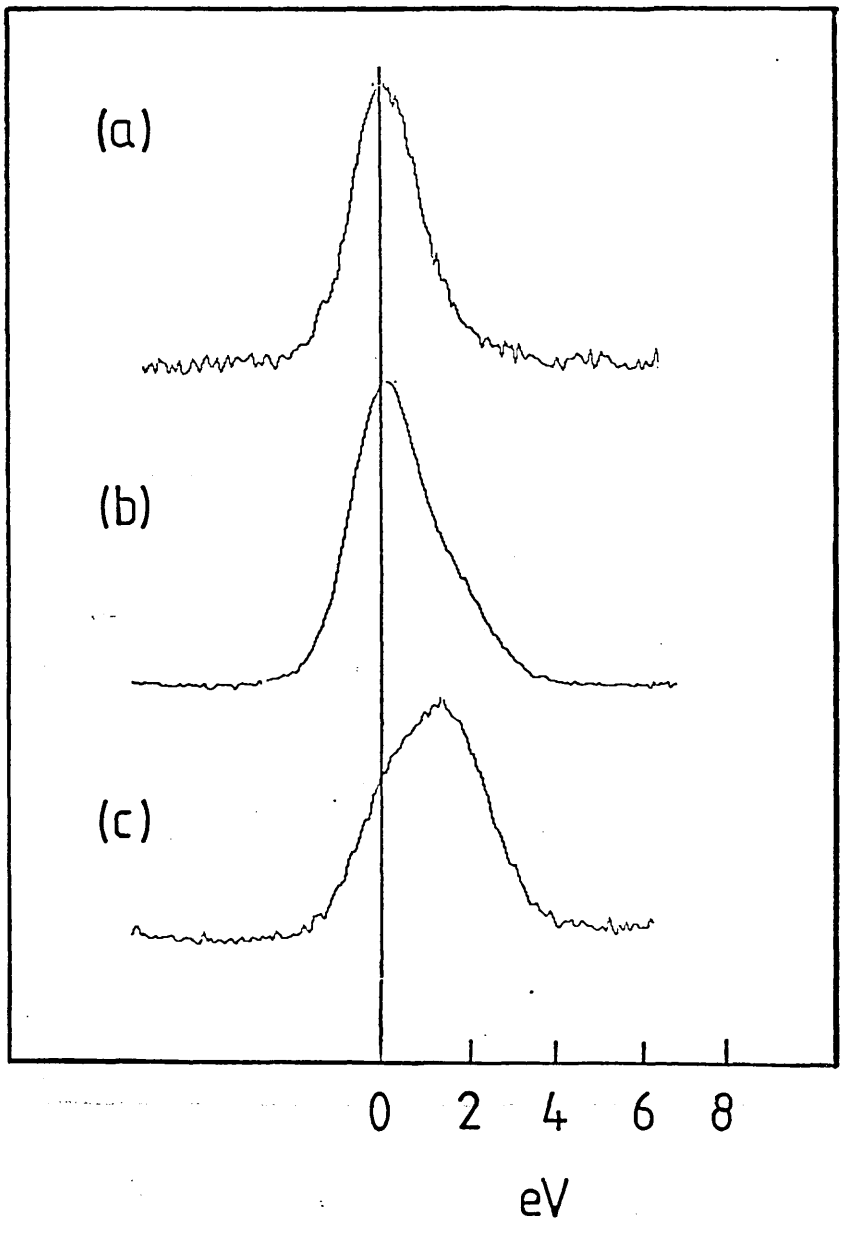


Figure 5.7 (a) Al:Kα O:1s signal of MgO at normal emission (b) After growth of a BaO layer about 4 monolayers thick, again at normal emission (c) spectrum as in (b) but at 15° emission angle.

clean MgO(001) to 0.125 after 2-3 monolayers of BaO deposition. This is in accord with the more marked attenuation of the electrons with low kinetic energy by the overlayer. Secondly it was found that for low angles of emission the $Ba3d_{5/2}$/Mg1s ratio increases remarkably from 2 at normal emission to 15 at 15° emission (in the case of 1-2 monolayers growth). No changes in these two ratios would be expected for a thick surface layer of $Ba_{1-x}Mg_xO$. This lack of interdiffusion is directly related to the large enthalpy of segregation of Ba^{2+} to the surface of MgO and the associated large energy of activation for diffusion of Ba^{2+} into the bulk MgO crystal.

5.3.3 The anomalous chemical shift associated with Ba and Ba^{2+}

As noted previously barium shows an anomalous chemical shift in that the Ba^{2+} state has a lower binding energy than the Ba^{o} state. Wertheim[14] gives a magnitude of -0.5 ± 0.3 eV for the shift which is almost the same as the -0.7 ±0.3 eV found in this work when the barium metal overlayer is oxidised.

The explanation for this unusual shift apparently lies in the increased population of the Ba:5d valence levels of Ba metal upon oxidation. The 5d orbitals seem to play a significant role in the Ba-O bond but are little involved in the band structure of the Ba metal itself. As they are more compact than the Ba:6s orbitals, the flow of charge

into an orbital with smaller spatial extent decreases the core electron binding energy. The coulomb repulsion between core and 5d levels effectively more than compensates for the decreased Coulomb repulsion between core and valence 6:s levels.

5.3.4 Quantification of XPS associated with BaO coverages

Quantification of Ba coverage was achieved in the following way. The intensity ratio I(Mg:1s)/I(O:1s) was measured for clean, annealed MgO(001) at normal emission. BaO was deposited onto the MgO(001) surface using the cycles outlined above until the emission from the Mg core peaks including the strong Mg:KLL Auger peak was completely suppressed. The intensity ratio $I(Ba{:}3d_{5/2})/I(O{:}1s)$ was then measured at normal emission and is representative of bulk BaO. The ratio R_c between $Ba{:}3d_{5/2}$ and Mg:1s intensities each normalised to the O:1s intensity was found to be 1.56. Now R_c (see appendix A) is given by:

$$R_c = \frac{\sigma(Ba{:}3d_{5/2})}{\sigma(Mg{:}1s)} \times \frac{1 - \exp[-a_0(MgO)/2\lambda(Mg{:}1s,MgO)]}{1 - \exp[-a_0(BaO)/2\lambda(Ba{:}3d_{5/2},BaO)]} \times \frac{1 - \exp[-a_0(BaO)/2\lambda(O{:}1s,BaO)]}{1 - \exp[-a_0(MgO)/2\lambda(O{:}1s,MgO)]} \times \frac{T(Ba{:}3d_{5/2})}{T(Mg{:}1s)} \quad \ldots 5.1$$

where:

σ are subshell ionisation cross sections

a_0 are lattice parameters

λ are electron pathlengths for the specified photoelectrons in a given oxide

T are instrumental transmission factors

For n monolayers of BaO on MgO the intensity ratio between Ba:$3d_{5/2}$ and Mg:1s peaks R_n is given by:

$$R_n = \frac{\sigma(Ba:3d_{5/2})}{\sigma(Mg:1s)} \times \frac{a_0(MgO)^2}{a_0(BaO)^2} \times \frac{1 - \exp[-a_0(MgO)/2\lambda(Mg:1s,MgO)]}{\exp[-na_0(BaO)/2\lambda(Mg:1s,BaO)]}$$

$$\times \sum_{j=0}^{n-1} \exp[-ja_0(BaO)/2\lambda(Ba:3d_{5/2},BaO)] \times \frac{T(Ba:3d_{5/2})}{T(Mg:1s)} \quad \ldots. 5.2$$

In deriving equations 5.1 and 5.2 we assume that BaO grows on MgO with its own characteristic lattice parameter $a_0(BaO)$. Effects such as photoelectron diffraction of MgO substrate electrons by the BaO overlayer are ignored in this simple model. We also ignore asymmetry in the photoelectron flux, but in any case effects due to the asymmetry parameter vanish when we combine equations 5.1 and 5.2 to obtain an expression for R_n independent of the cross sections and transmission function terms:

$$R_n = R_c \times \frac{a_0(MgO)^2}{a_0(BaO)^2} \times \frac{1 - \exp[-a_0(MgO)/2\lambda(O:1s,MgO)]}{1 - \exp[-a_0(BaO)/2\lambda(O:1s,BaO)]} \times$$

$$\sum_{j=0}^{n-1} \frac{\exp[-ja_0(BaO)/2\lambda(Ba:3d_{5/2},BaO)]}{\exp[-na_0(BaO)/2\lambda(Mg:1s,BaO)]} \times$$

$$\{1 - \exp[-a_0(BaO)/2\lambda(Ba:3d_{5/2},BaO)]\}$$

Analogous expressions for coverages between integral monolayer values can be formulated algebraically assuming a layer by layer growth mode. Thus the calibration of surface coverage depends only on the choice of electron pathlengths.

Following Leckey and coworkers[15][16] it is assumed that the inelastic pathlength is determined mainly by scattering from valence electron plasmon modes of the oxides. The λ values obtained from this model are as follows:

λ(Mg:1s,MgO) = 5.1Å

λ(Mg:1s,BaO) = 4.7Å $\quad \{ \lambda_{BaO} = 0.0995(E_{ke})^{3/4} \}$

λ(O:1s,MgO) = 18.5Å $\quad \{ \lambda_{MgO} = 0.1077(E_{ke})^{3/4} \}$

λ(O:1s,BaO) = 17.1Å

λ(Ba:3d,BaO) = 13.6Å

Note that these values are sensibly close to those of the so-called universal curve [17].

The calculated intensity ratio between Ba:$3d_{5/2}$ and Mg:1s peaks as a function of coverage is shown in figure 5.9. There are small cusps in the computed intensity curves upon completion of successive monolayers but it is doubtful if these could be located experimentally even if continuous operation of the getter source were possible. Figure 5.8 also classifies the LFED patterns observed for various BaO coverages, as discussed in section 5.5.

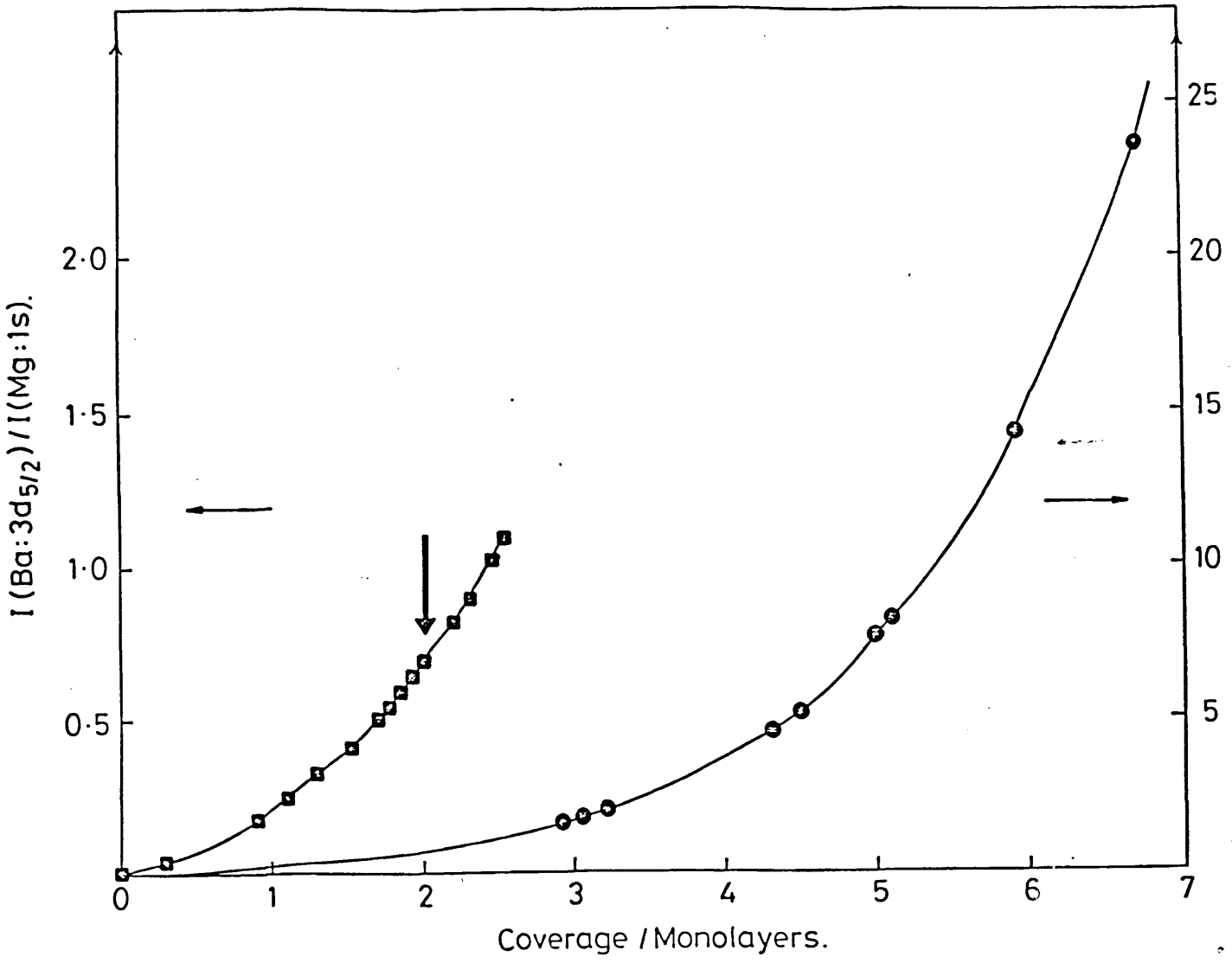


Figure 5.8 Calculated Ba:$3d_{5/2}$ / Mg:1s Al:Kα XPS intensity ratio as a function of BaO coverages in monolayers (see text). The squares (▪) denote surface coverages for which (1x1) LFFD patterns with the lattice spacing characteristic of MgO were observed. These patterns became progressively less well defined with increased BaO coverage. The circles (•) denote coverages for which LEED patterns with the LEED pattern characteristic of BaO were observed. The bold vertical arrow denotes the BaO loading at which the 2x2 or $\sqrt{2}$x$\sqrt{2}$ superstructure LEED patterns had been expected.

5.4 ELS

ELS proved to be of particular value in studying oxidation of Ba deposits during growth of BaO. Figure 5.10 shows the specular ELS spectrum of barium metal deposited onto 4.5 monolayers of BaO on MgO(100) excited by a 100eV beam of electrons and then a similar spectrum after subsequent oxidation. The surface and bulk plasmons[18] at X and Y respectively due to barium metal are indicated by arrows. There is also loss structure close to the elastic peak between about 0.7 and 2.5eV. The peak Z corresponds to the surface plasmon of BaO and is present in both spectra.

Low energy loss structure in ELS has been observed before in BaO and structure close to the elastic peak in electron bombarded BaO has been attributed to V^- centres i.e. cation vacancies compensated for by two O^- anions. However as shown by figure 5.10 when metal is deposited onto BaO loss structure is generated and an alternative theory might be that it is related to small metallic islands of barium. The corresponding growth of loss structure close to the elastic peak in SrO and CaO has been attributed to V^- centres[19] also. In the present work it seems extremely unlikely that cation vacancies should be generated by deposition of metal, so the experiments rule out the earlier assignment of the loss structure in the case of BaO at least. Further experiments of metal deposition onto MgO, CaO and SrO would be of great value in clarifying the situation for other oxides.But whatever the

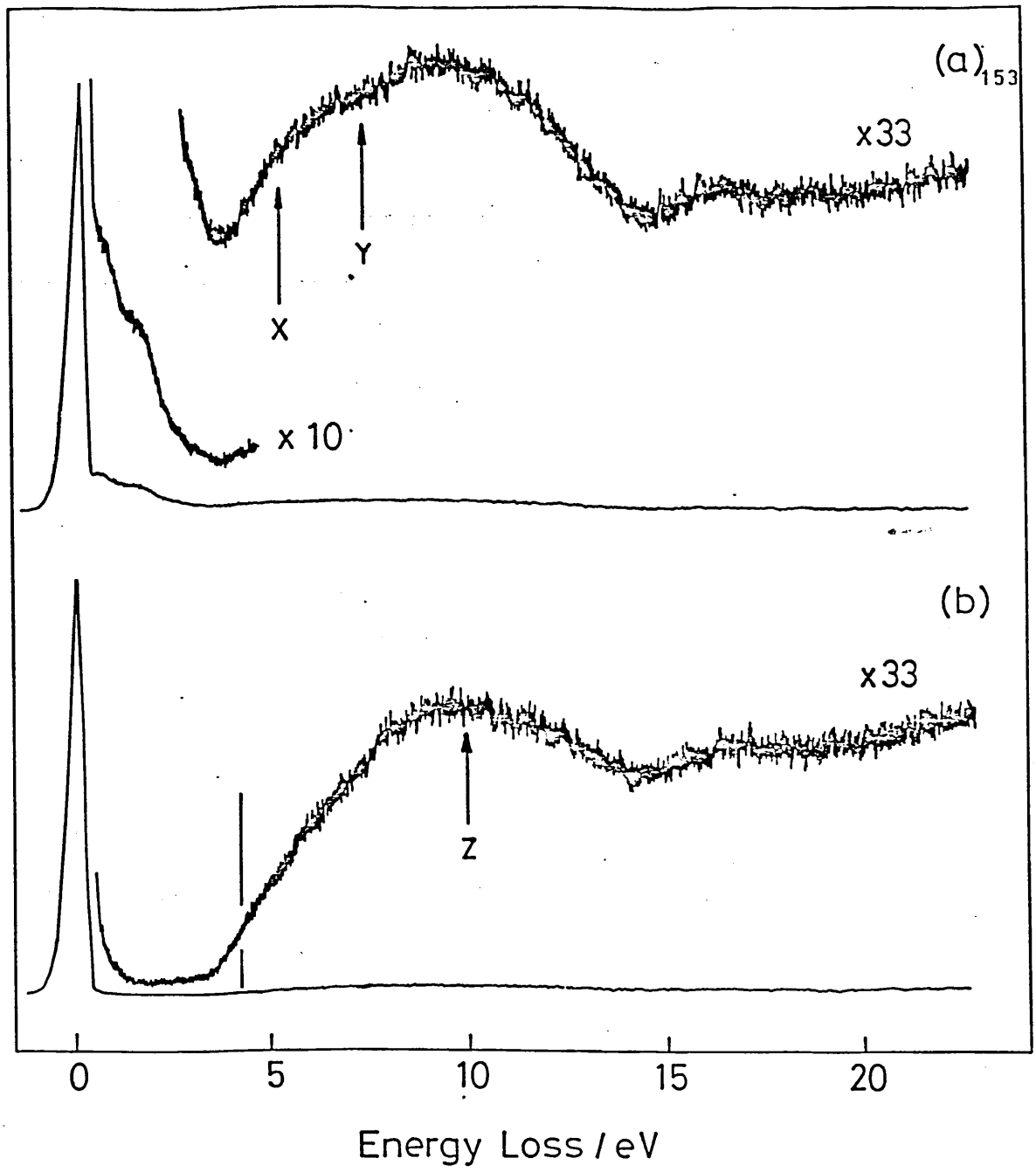


Figure 5.9 EEL spectra excited with 100eV electron beam in specular mode (angle of incidence : 45°) showing the effect of oxygen exposure on the Ba deposit.
(a) The spectrum recorded after deposition of ~ 0.1 monolayer of Ba metal onto 4 monolayers of BaO. The arrows mark positions of bulk and surface plasmons of Ba metal.
(b) The spectrum after oxygen exposure. Note the vertical line showing the bandgap of bulk BaO.

assignment the disappearance of this loss structure in the Ba/BaO system is due to the effects of oxidation on electronic structure. The rest of the spectrum is dominated by interband excitations across the bandgap of 4.2eV which is smaller than for MgO.

5.5 LEED and the structure of BaO overlayers on MgO

Progressive deposition of barium metal in 0.2 monolayer doses, followed by oxidation and annealing led to the gradual extinction of the MgO(100) LEED spot patterns. Above a cumulative coverage of about 2 monolayers of BaO diffuse scattering was observed. Overlayers displaying sharp LEED patterns could be grown by oxidation of a large initial deposit of metal of about three monolayers, leading to the epitaxial growth of an ordered BaO overlayer. At first because the patterns appeared similar to those of MgO itself it was thought the BaO had been desorbed during annealing, but the XPS showed this not to be so. Subsequent detailed analysis of photographs showed that the spot positions in the sharp overlayer LEED patterns corresponded to slightly different lattice spacing to those of MgO(100). This is illustrated in figure 5.1 where a plot of sinθ versus the inverse square root of the beam energy for the (11) spots of MgO(100) can be found alongside those for the lowest order spots of the BaO overlayer. The d spacing for the MgO pattern itself is 2.98

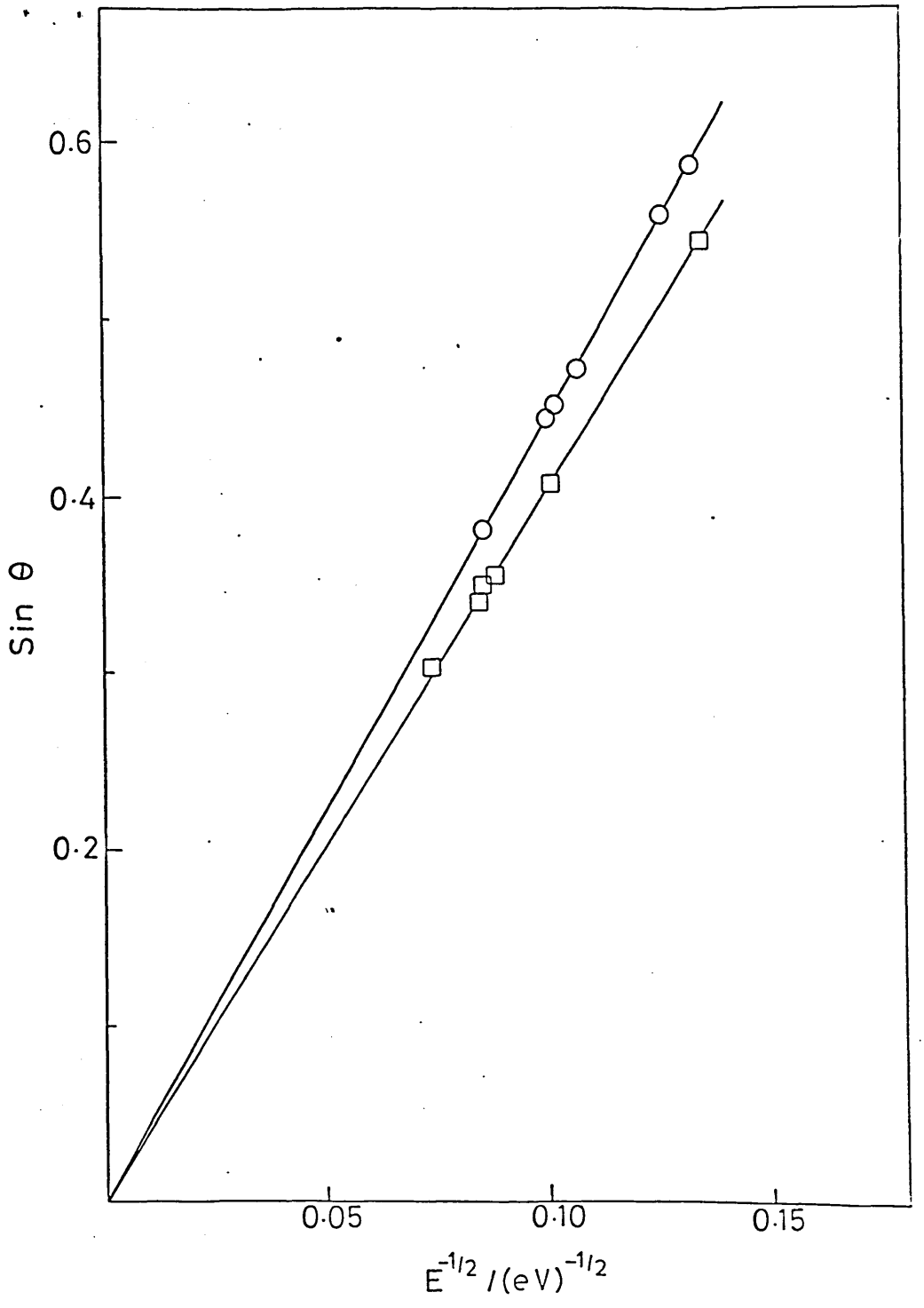


Figure 5.10 A plot of sinθ versus $1/E^{1/2}$ (E is the beam energy) for the lowest order LFED spots of MgO(001) and for the BaO overlayer on MgO. Squares (▪) are from the MgO(001) LFED patterns: circles (•) are from BaO overlayer LFED patterns.

± 0.06Å corresponding to $a_o(MgO)/\sqrt{2}$ = 2.978Å as expected for (11) spots. The overlayer spots gave a d spacing of 2.73 ± 0.03Å corresponding to a(BaO)/2 = 2.76Å, where a(BaO) is the lattice parameter for rocksalt BaO. The analysis shows the spots to be the (20) beams from a BaO overlayer rotated through 45° relative to that of the substrate. Ordered growth is apparently encouraged by the near equality between $a_o(BaO)$ = 5.52Å and $\sqrt{2}\ a_o(MgO)$ = 5.955Å. Growth from solution of alkali halide on alkali halide systems with similar relationships between lattice parameters is well documented[19].

The photographs figures 5.11,5.12 and 5.13 show the sequence from MgO to BaO spots with BaO coverage. The absence of (11) beams from the overlayer is puzzling, and even after extensive visual inspections at energies between 50eV and 300eV they were not seen. There are two possible explanations for the loss of the (11) spots in the rocksalt structure of the BaO overlayer. The first involves an explanation by Prutton[20] in terms of kinematic LEED theory. He suggests that a destructive interference occurs for (11) spots whose intensities depend on a difference of structure factors for cation and anion sites. However it is expected that structure factors will only be equal if cations and anions have equal numbers of electrons and with BaO the electron density surrounding Ba^{2+} is much higher than around O^{2-}. In any case the applicability of kinematic theory at low beam energies is highly questionable.

The second explanation involves consideration of the

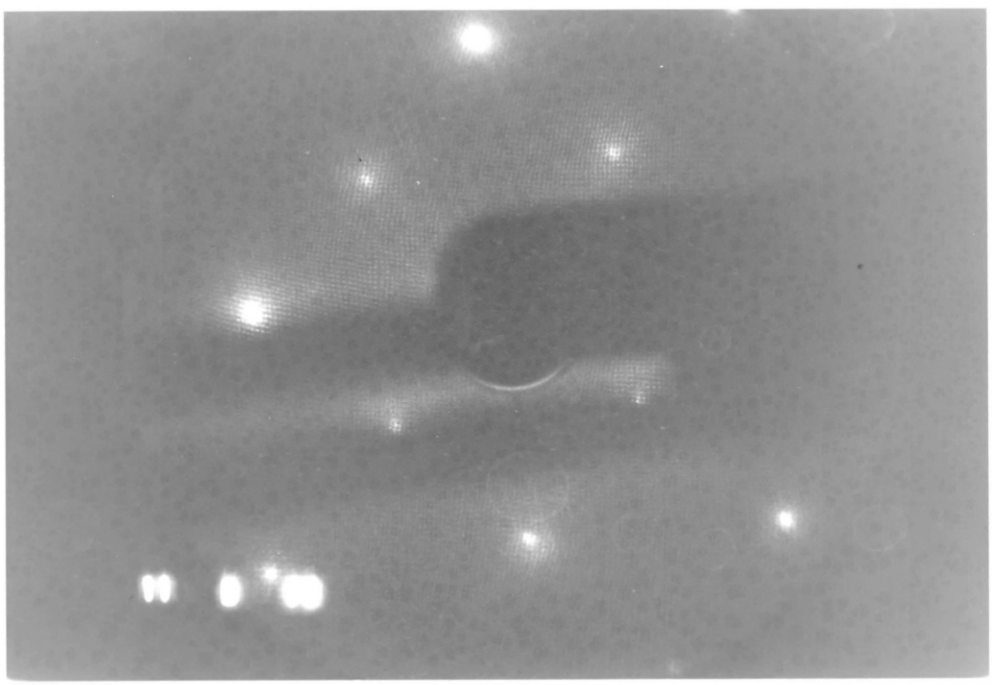


Figure 5.11 LEED pattern from MgO(001) at 138eV beam energy showing (11) and (20) spots.



Figure 5.12 LEED pattern from ▪ 4 monolayers of BaO on MgO at 142eV beam energy. The crystal has been rotated slightly in comparison to figure 5.11.

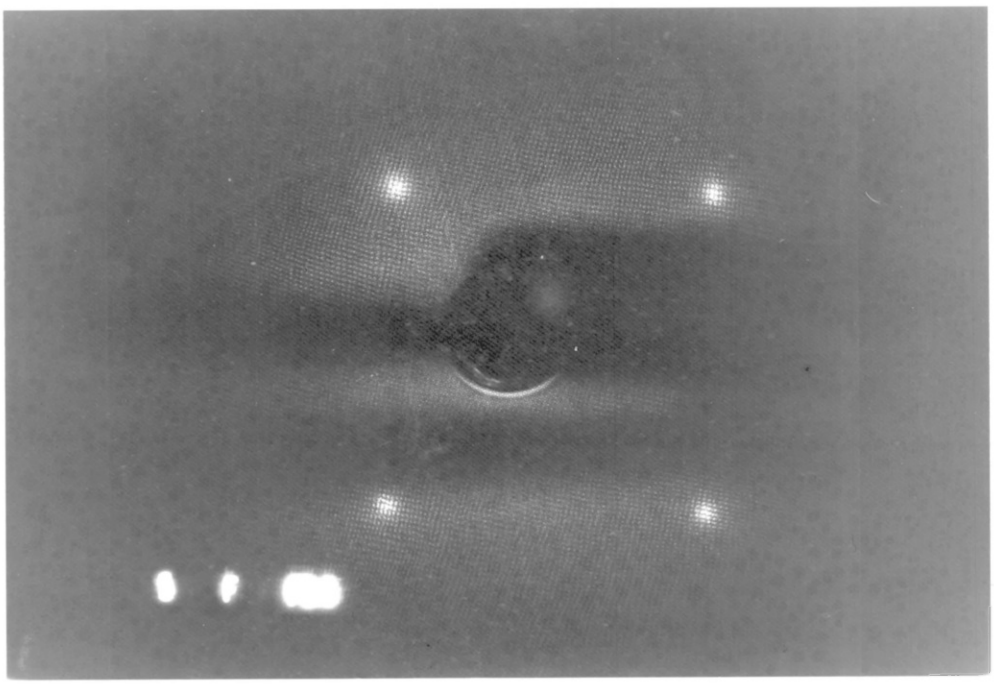


Figure 5.13 LEED spot pattern of the identical crystal as in figure 5.12 but at 97.6 eV beam energy.

growth mode of the BaO overlayer. The LEED pattern implies that the Ba and O positions could have become equivalent effectively halving the size of the unit cell. This may occur due to the growth in domains smaller than the coherence area of the LEED experiment shifted relative to each other by a(BaO)/2 along the (110) directions of the substrate. Averaged over a large number of domains the amplitudes in the (11) beams from different domains will cancel, leading to the extinction of the spots. The antiphase boundaries separating the BaO domains should produce diffuse scattering which is observed in a brighter background in the LEED patterns of BaO on MgO.

5.6 Ionic model simulation of the MgO/BaO interface

As indicated in the introduction, the previously predicted $\sqrt{2} \times \sqrt{2}$ or 2×2 superstructure of BaO on MgO were not seen at any stage of our experimentation. The calculations were therefore extended to include a structure such that $a_o(BaO) = \sqrt{2}a_o(MgO)$. The simulation involved a surface block of MgO and two monolayers of BaO (see figure 5.14). Relaxation was allowed along the surface normal both in the BaO and the first three layers of MgO with ten more layers of MgO being taken to represent the bulk crystal in the sum.

The repulsive part of the potentials used in the calculations were derived as follows:

(i) Mg^{2+}— Mg^{2+} and Ba^{2+}— Ba^{2+} and are based on the

free ion wavefunctions.

(ii) Within the MgO block. Mg^{2+}— O^{2-} and O^{2-} — O^{2-} potentials were based on O^{2-} wavefunctions calculated for MgO.

(iii) For the overlayer two types of potentials were used based on O^{2-} wavefunctions calculated for MgO and O^{2-} calculated for BaO.

Three configurations were considered as shown in figure 5.15:

(1) Ba^{2+} and O^{2-} on top of O^{2-} and Mg^{2+} respectively. This configuration relaxes to the rumpled structure previously discussed[9], when using MgO potentials, but with BaO potentials gave no stable minimum. The relaxed structure is nonetheless higher in energy than the separated MgO block and the 2 monolayers of BaO.

(2) A structure with two BaO monolayers conforming to $a_o(BaO) = \sqrt{2}a_o(MgO)$ parallel to the surface. The overlayer ions sit above the substrate ions and it is not possible to match ions of opposite charge. There are equal numbers of nearest neighbour repulsive and attractive interactions and the MgO surface ionic layer can relax considerably to accomodate the structure. Two distinct arrangements based on substrate Mg^{2+} and O^{2-} sublattices can be envisaged which have similar energy below that of the separated blocks. The separation between the two BaO layers is significantly less than BaO bulk, see figure 5.16, which is a result of the lengthening of the lateral Ba^{2+}—O^{2-} bond

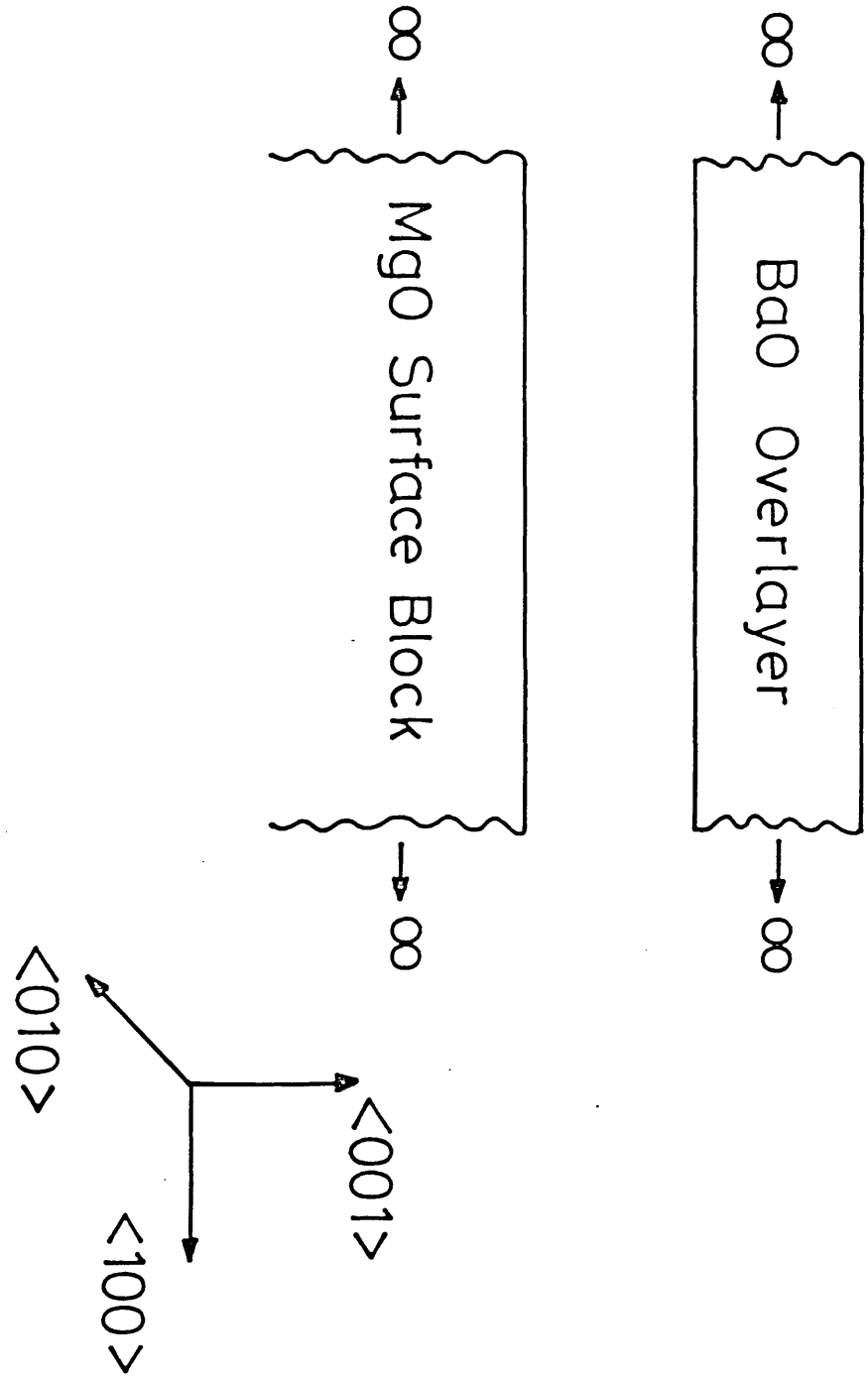


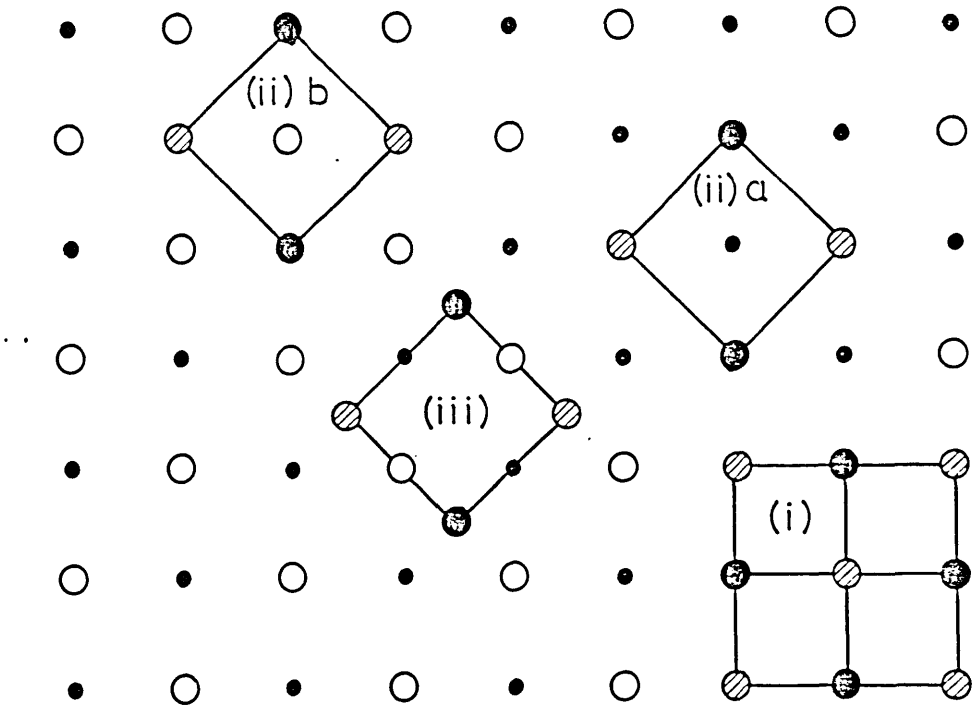
Figure 5.14 Schematic of the MgO and BaO blocks used in the ionic model calculations.

in the calculations.

(3) A third structure similar to (2) but with occupation of hollow sites to avoid short range repulsive interactions. This structure was found to have higher energy than (2).

From the above arguments structure (2) is the most likely to exist but these calculations do need to be extended to take account of the slight mismatch between the $\sqrt{2}a_o(MgO)$ and $a_o(BaO)$. As with most simulation the more complicated treatment awaits access to a more powerful computer, but nevertheless in conclusion we can say that the predictions give stong backing to the experimental findings and our interpretations and do indicate a preservation of a Ba^{2+}—— O^{2-} separation in the surface layers similar to that in BaO. A table with the relevant energies can be found on page 192.

I am greatful to Dr. W.C.Macrodt for carrying out the calculations descibed in this section.



Mg^{2+}

Ba^{2+}

O^{2-} (MgO surface layer)

O^{2-} (BaO layer)

Figure 5.15 The plan view of the alternative configurations for the growth of BaO on MgO(001).
(1) The top sites occupied
(2a) Where $a_o(BaO) = \sqrt{2}\,a_o(MgO)$ based on O^{2-} sublattice
(2b) as (2a) but with Mg^{2+} sublattice
(3) as (2) but in the hollow sites

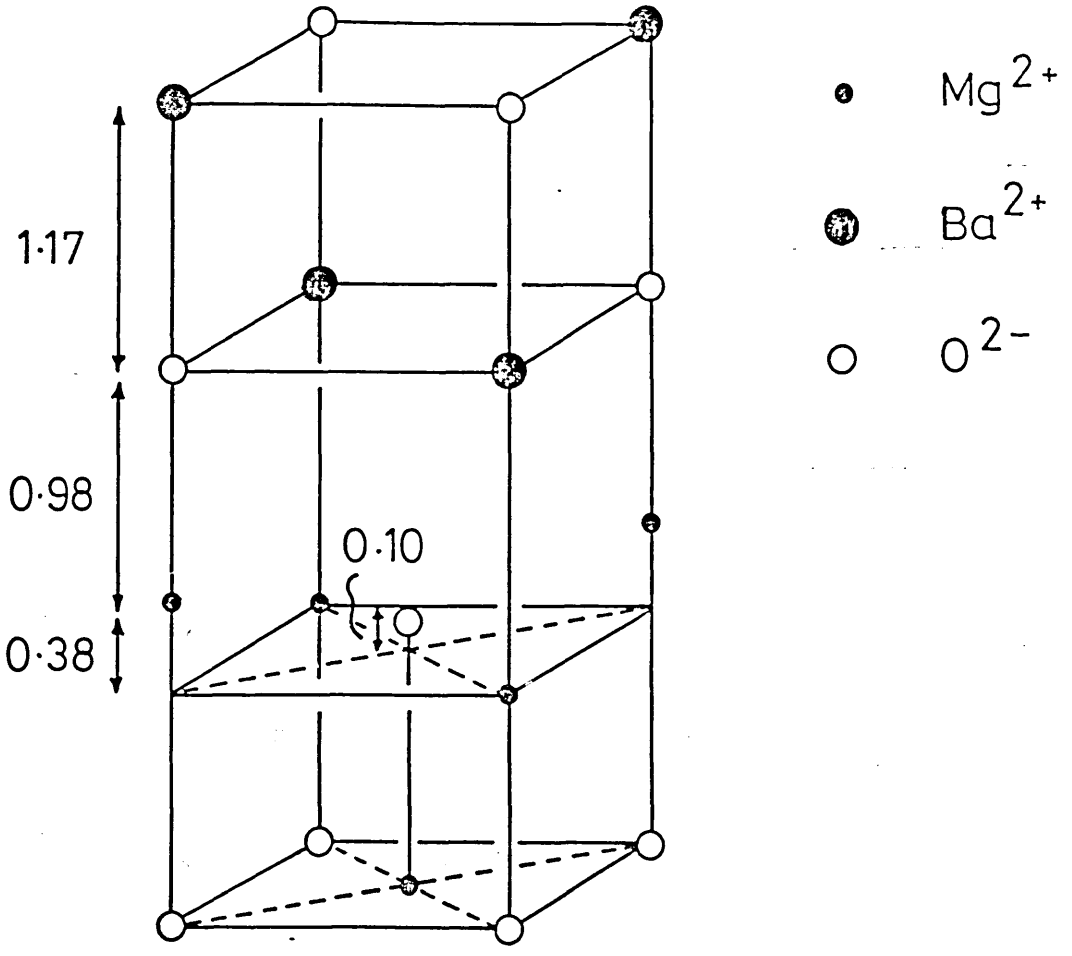


Figure 5.16 Fully relaxed structure for 2 monolayers of BaO on MgO. Distances are given as multiples of the Mg^{2+} — O^{2-} separation in MgO. (i.e. $a_o(MgO)/2 = 2.1717\text{Å}$).

Chapter 6. Barium segregation in doped MgO

6.1 Introduction

Segregation of dopants or impurities to the surface of a material can in general lead to a profound modification of the surface structure and surface energy. This in turn can have significant practical consequences in fields such as catalysis, ceramic sintering and surface corrosion. This chapter concerns the surface segregation of Ba in MgO. XPS data for Ba doped MgO powders is presented and compared with data relating to single crystal MgO doped by indiffusion of Ba into the crystal. Included also are LEED patterns associated with Ba-segregated surface of MgO(001) that are complex but are in close association with the observed segregation in the powders. Isovalent cation dopants in highly ionic oxides are also of major interest for theoretical simulation work based on the ionic model and we relate the experimental findings to theoretical calculations on the same system.

XPS, AES, LEED and other UHV techniques have been used in recent years to study segregation in a number of oxide systems but the inherent difficulty of obtaining reliable experimental values for heats of segregation has also led to a large number of theoretical papers concerned with simulating lattice impurities and their propensity for segregation to the surface of ionic crystals. Most of the experimental work and calculation of enthalpies of oxides in this field so far is based on the interpretation of data in the form of Arhenius plots of the type:

$$r_s = r_b \exp(-\Delta H / kT) \quad .... 6.1$$

Where r_s and r_b represent the concentration ratio of two elements in the surface and bulk respectively and ΔH the enthalpy of segregation. Plots of $\log_e r_s$ versus $1/T$ yield a value for ΔH. In this chapter it is shown that for segregation of Ba in MgO this sort of analysis is inappropriate as the heat of segregation varies strongly with surface coverage due to the large size of the segregant cation.

There is not a great deal of experimental literature on the segregation of cation dopants in oxides but Bank et al[1] have derived an experimental enthalpy of segregation of Mg^{2+} to the surface of α-Al_2O_3(0001) of about -146kJ/mole and McCune et al[2] have derived an enthalpy of segregation of -44kJ/mole for the segregation of Y at the surface of polycrystalline α-Al_2O_3. Specifically for MgO there have been a number of interesting studies concerned with both the experimental and theoretical determination of enthalpies of segregation[3][4]. McCune and Wynblatts[5] pioneering study involved measuring the concentration of Ca^{2+} at the (100) surface of a doped crystal as a function of temperature using ion scattering and Auger spectroscopies. This allowed the determination of the heat of segregation 50 kJ/mole, which agreed accurately with the calculated value. This work was extremely time consuming because long in-situ high temperature anneals

were necessary to allow the crystal surface to come into equilibrium with the bulk at the lower end of the temperature studied. Cimino and de Angelis[6] studied MgO/NiO solid solutions and showed that the Mg/Ni ratio at the surface is similar to the bulk. With reference to this study other authors have calculated bulk substitution energies that are very dependent on cation size[7]. For instance the Be^{2+} ion has a negative substitution energy of -385kJ/mole in bulk MgO, whereas the much larger Ba^{2+} ion has a positive substitution energy of +1123kJ/mole[3]. If the large ion causing the lattice strain segregates to the surface with a negative heat of segregation the situation is somewhat relieved. The similar ionic size of Mg^{2+} and Ni^{2+} is thus in accordance with Cimino's and de Angelis's result, which points to a small heat of segregation

In simulation studies, the calculated enthalpies of segregation are strongly dependent on coverage. Mackrodt et al[8] have developed a procedure for a determination of segregation isotherms that includes coverage-dependent enthalpy of segregation and these calculations are used for interpretation of experimental results here. The detailed thermodynamic relations involved are formulated elsewhere[8].

Experimentally the segregation of Ba in MgO has not been studied using UHV spectroscopies, but the theoreticians have explored many details of the system. The heat of segregation of Ba^{2+} to MgO(001) has been estimated

to be -376.25kJ/mole at zero coverage and 28.94kJ/mole at full coverage of an unreconstructed surface[3][7]. Allowance of reconstruction to a less sterically hindered $\sqrt{2} \times \sqrt{2}$ surface layer lowers the value to -136.03kJ/mole. Reconstruction also lowers the surface energy by 2.40 J/m^2 for Ba^{2+}/MgO(001) and 4.85 J/m^2 for Ba^{2+}/MgO (110). The surface energies for the pure crystals are 1.06J/m^2 and 2.79J/m^2 respectively showing that Ba segregated surfaces have a negative surface energy and hence a thermodynamic barrier to sintering.

6.2 Experimental

Polycrystalline Ba doped MgO pellets were prepared from the respective nitrates. Carefully weighed out amounts of $Ba(NO_3)_2$ and $Mg(NO_3)_2$ 0.25 H_2O (Johnson Matthey Specpure Grade) were dissolved in dilute nitric acid and each solution was cautiously evaporated to dryness. The powders were then heated to 1273K in a temperature programmable furnace at a rate of 1K/minute to ensure smooth decomposition of the nitrates. The temperature range over which the solid melts and decomposes is short and care must be taken that the gases given off do not blow the solid all over the furnace. Each powder, of specific dopant level (7, 35, 70, 700 and 7000ppm), was compressed into 13mm diameter pellets between tungsten carbide dies at a pressure of 10-12 tons/cm^2. The pellets are fragile at this stage and care must be taken. Each pellet was fired at 1623K in recrystallised alumina boats

for 48 hours in a clean muffle furnace and quickly quenched in air on removal from the furnace. This has the effect of quenching the crystals under constant conditions and retaining the segregation effects that occured at the higher temperature.

Tantalum trays were specially designed to hold the pellets with as much thermal contact as possible, and were themselves mounted on UHV compatible stubs. In situ cleaning, via RF heating for several minutes at about 1073K rid the pellets of any carbonaceous overlayers. At 1073K one does not expect cation mobility to be great and over such a short time the surface composition of the pellet is unlikely to change from that established in the muffle furnace. In a single crystal study the MgO crystal slice was cleaned as before in situ to give sharp LEED spots and no impurity peaks in the XPS. Several monolayers of Ba metal were deposited and exposed to 300L of oxygen at 10^{-6} torr to oxidise the barium. Heating the crystal for an hour in-situ to the highest temperature possible with RF heating, 1475K, caused no measurable interdiffusion of the overlayer into the substrate. The crystal was then removed from the ESCALAB and heated in the muffle furnace at 1633K to allow interdiffusion of Ba^{2+} in the MgO. On reinsertion to the ESCALAB the crystal was cleaned by RF heating at 1073K as before and when analysed via XPS gave similar Ba surface coverages to that of the polycrystalline samples.

6.3 Results

Figure 6.1 shows widescan XPS for Ba doped MgO ceramic pellets at two different bulk doping levels 7 and 7000ppm indicating that the intensity of the Ba:3d peaks is similar. In conjunction with this figure 6.2 shows narrow scan XPS studies of the Ba:3d peaks of three different doping levels of the pellets and demonstrates that the shape and intensity is essentially invariant with the bulk doping level in the range 7ppm to 7000ppm. The Ba:3d peaks are quantified in terms of a ratio with Mg:1s and the surprising lack of variation of this ratio with doping level is shown in figure 6.3. As the latter ratio is anomalous it is informative to calculate the predicted intensity ratio without segregation, using the methodology in appendix A developed in chapter 5, for comparison with the experimental findings. Use of an experimental intensity ratio R_c again to cancel the cross sectional and transmission function terms (as in chapter 5) allows the intensity ratio between Ba and Mg peaks in the absence of segregation to be calculated from only pathlength terms[9][10]. If one considers a fraction χ of the Mg sites replaced by Ba, the intensity ratio between Mg and Ba peaks in the absence of segregation is given by:

$$R_\chi = \frac{\chi}{1-\chi} \times \frac{\sigma(Ba:3d_{5/2})}{\sigma(Mg:1s)} \times \frac{T(Ba:3d_{5/2})}{T(Mg:1s)} \times$$

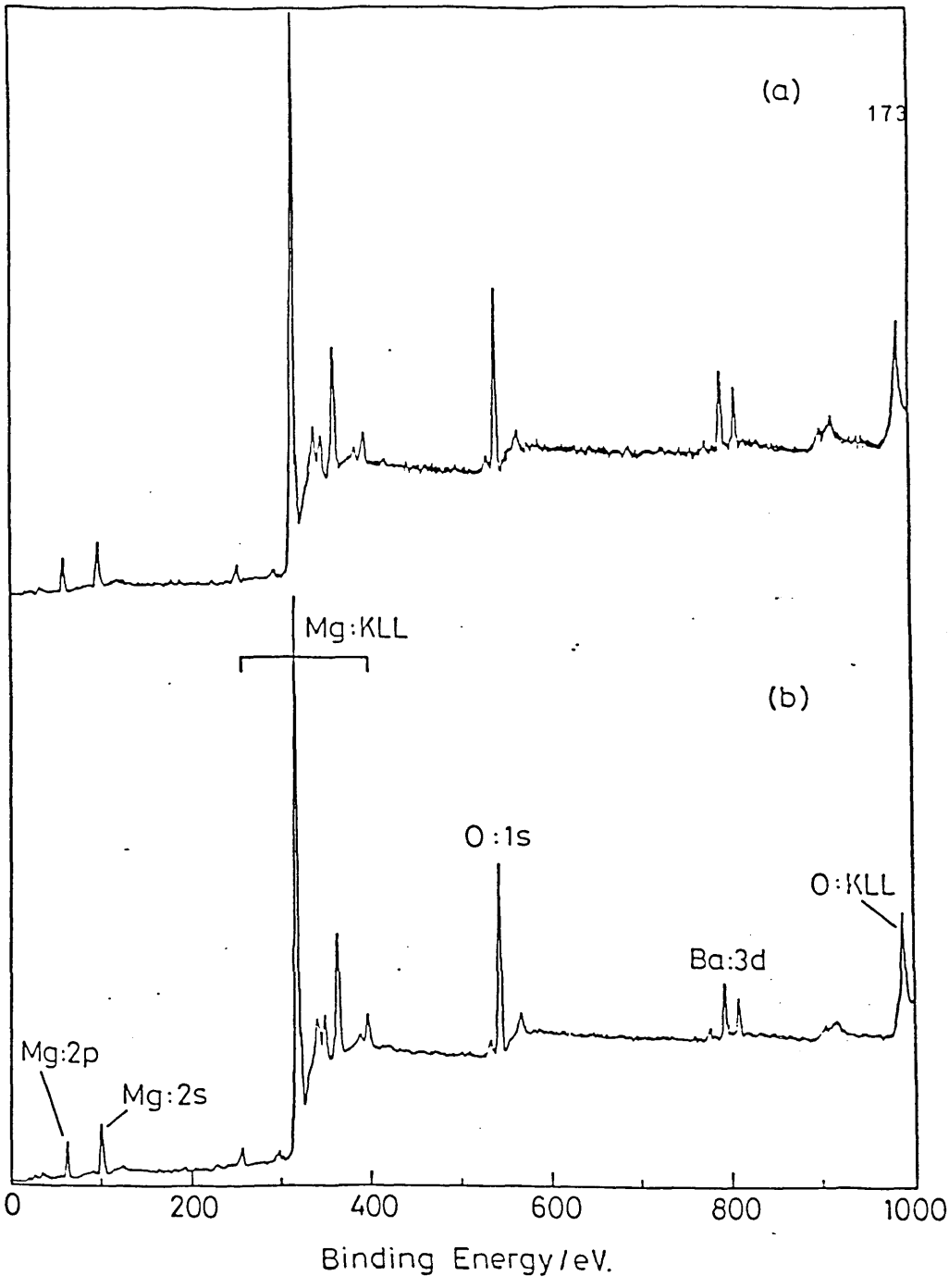


Figure 6.1 Widescan XPS excited with Al:Kα radiation for Ba doped MgO ceramic pellets at two different bulk doping levels (a) 7ppm (b) 7000ppm.

$$\frac{1 - \exp[-a(MgO)/2\lambda(Mg:1s,MgO)]}{1 - \exp[-a(MgO)/2\lambda(Ba:3d_{5/2},MgO)]} \quad \ldots\ldots 6.2$$

Hence using R_c as before:

$$R_\chi = \frac{\chi}{1-\chi} \times R_c \times \frac{1 - \exp[-a(MgO)/2\lambda(O:1s,MgO)]}{1 - \exp[-a(BaO),2\lambda(O:1s,BaO)]} \times$$

$$\frac{1 - \exp[-a(BaO)/2\lambda(Ba:3d_{5/2},BaO)]}{1 - \exp[-a(MgO)/2\lambda(Ba:3d_{5/2},MgO)]} \quad \ldots\ldots 6.3$$

It must be pointed out that the calculation applies strictly only to (001) single crystal surfaces and that we have neglected photo-electron diffraction terms in the calibration factor. However the measured intensity ratio is so different to that expected by these calculations (see figure 6.3) that it is clear that marked segregation of Ba^{2+} to the pellet surface is occuring.

To proceed further with the quantification the model of known simulation studies[8] is adopted which indicate that segregation would be limited to the topmost ionic layer. There were three aspects of the XPS spectra that supported this idea. Firstly mild argon ion bombarment (2 KeV at about $5\mu A/cm^2$) led to a drastic reduction of the Ba:3d signal. Secondly it was found that there is only half as much background intensity and satellite loss intensity

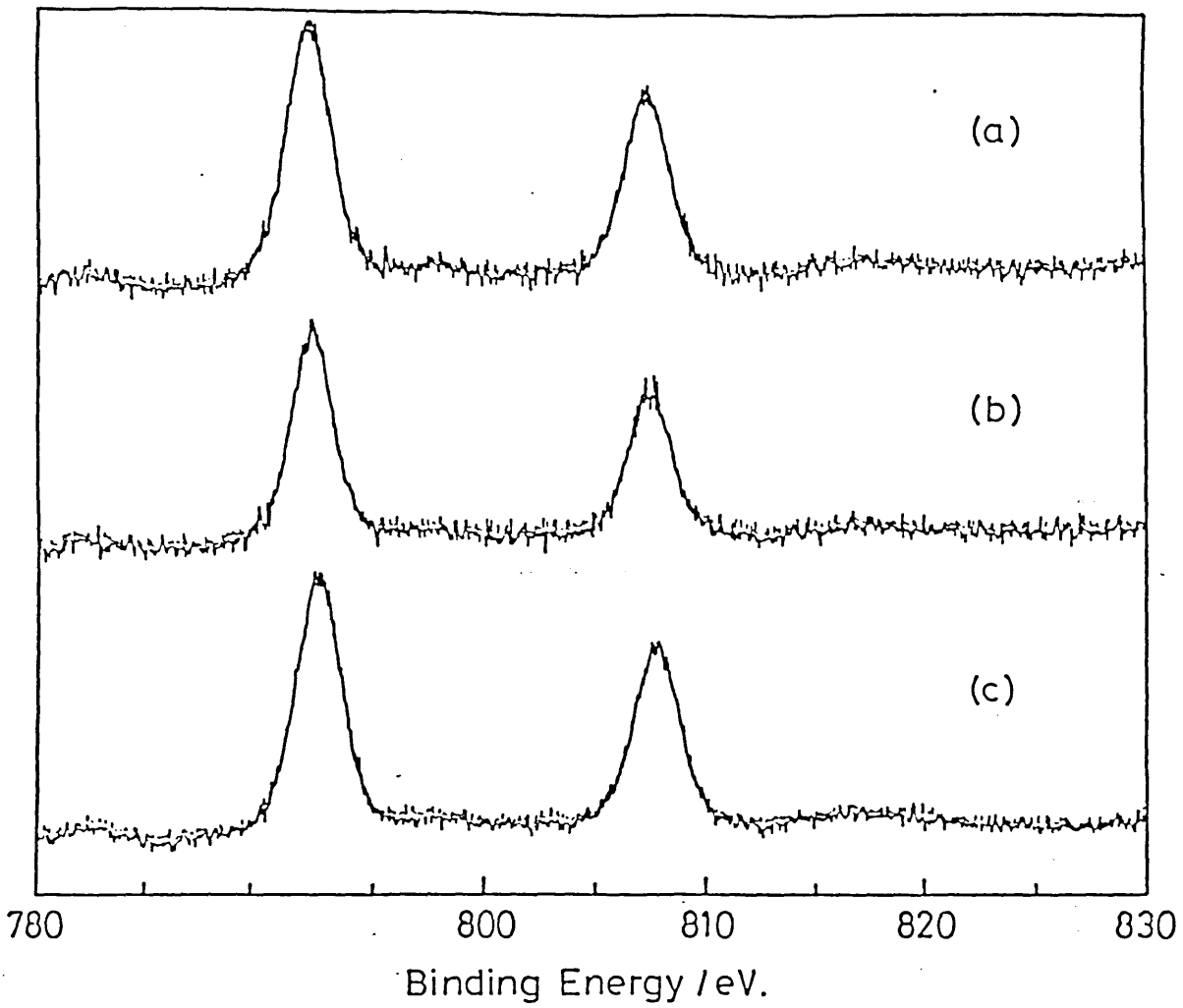


Figure 6.2 Ba:3d structure in Al:Kα XPS of doped MgO ceramic pellets at three different bulk doping levels (a) 700ppm (b) 70ppm (c) 7 ppm.

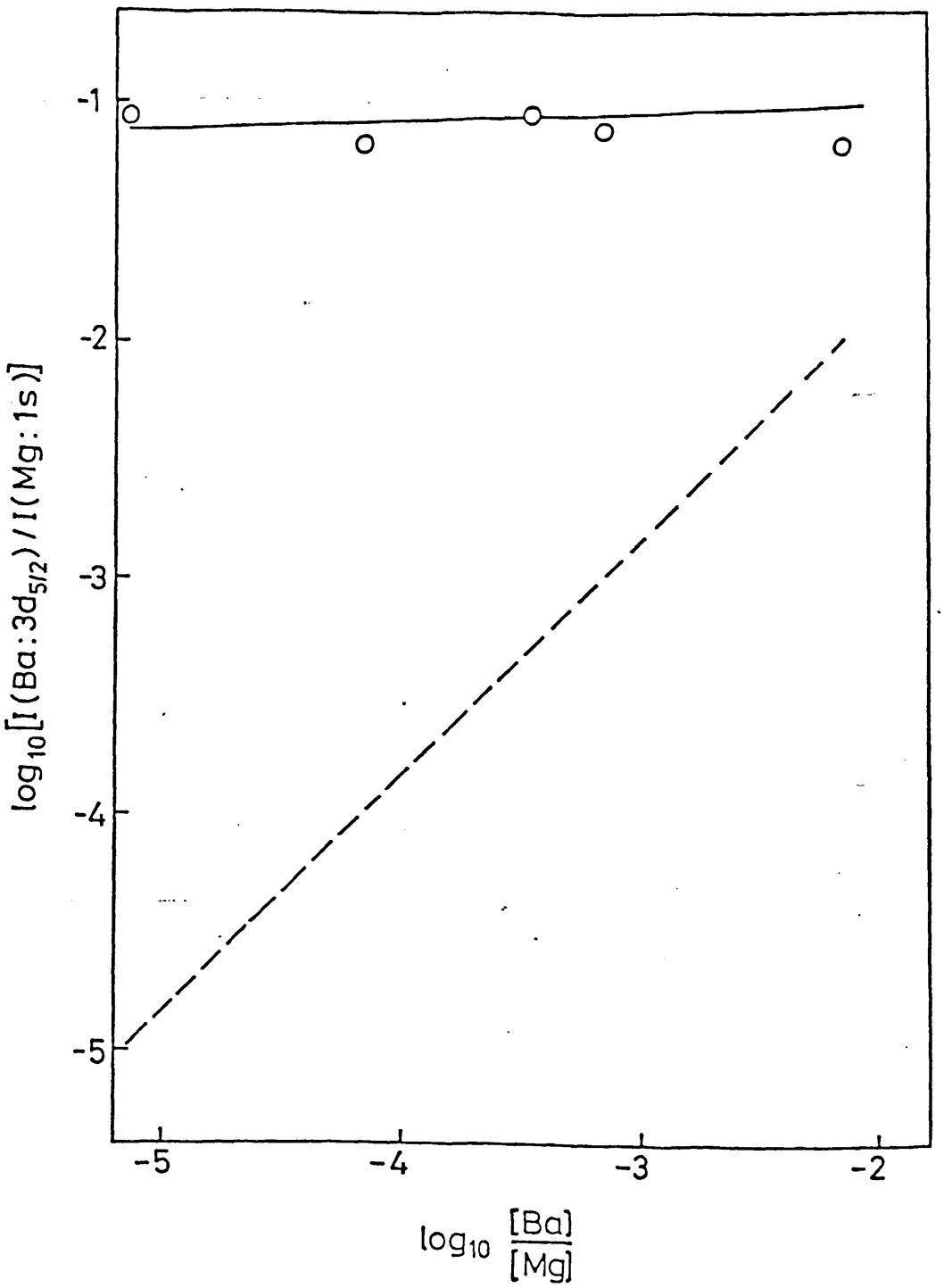


Figure 6.3 Intensity ratio between Ba:$3d_{5/2}$ and Mg:1s peaks in Mg:Kα excited XPS of Ba-doped MgO as a function of bulk doping level. Full circles represent experimental data. The full line is calculated from the theoretical heat of segregation and the dashed line is the calculated intensity ratio assuming no segregation, as described in the text.

associated with the pellets compared with the "bulk" BaO (see figure 6.4). This can be related to intrinsic and extrinsic plasmon modes[11]. Calculations for photoemission from simple metals have shown that extrinsic plasmons make up half of the satellite loss intensity. The lack of any extrinsic plasmons associated with only one segregant layer would coincide with the loss of background. A brief survey of figure 6.4 shows the change in loss intensity to be about one half going from bulk BaO to a monolayerof BaO on top of MgO. Thirdly the Ba:$3d_{5/2}$ / Mg:1s intensity ratio showed the expected increase with increasing take off angle associated with the top most layer as shown in figure 6.5.

If a fraction θ of Mg ions has been replaced by Ba ions in the surface layer, the intensity ratio of Ba:$3d_{5/2}$ / Mg:1s denoted by R_θ is given by:

$$R_\theta = \frac{\sigma(Ba:3d_{5/2})}{\sigma(Mg:1s)} \times \frac{T(Ba:3d_{5/2})}{T(Mg:1s)} \times \frac{\theta\{1 - \exp[-a(MgO)/2\lambda(Mg:1s,MgO)\}}{\{1-\theta\}\{1-\exp[-a(MgO)/2\lambda(Mg:1s,MgO)]\}+\exp\frac{-a(MgO)}{2k(Mg:1s,MgO)}} \quad \ldots\ 6.4$$

From R_c and equation 6.4 :

$$R_\theta = R_c \times \frac{1-\exp[-a(MgO)/2\lambda(O:1s,MgO)]}{1-\exp[-a(BaO)/2\lambda(O:1s,BaO)]} \times$$

$$\frac{1-\exp[-a(BaO)/2\lambda(Ba:3d,BaO)]}{1-\exp[-a(MgO)/2\lambda(Mg:1s,MgO)]} \times$$

$$\frac{\theta\{1-\exp[-a(MgO)/2\lambda(Mg:1s,MgO)]\}}{\{1-\theta\}\{1-\exp[-a(MgO)/2\lambda(Mg:1s,MgO)]\}+\exp\frac{-a(MgO)}{2k(Mg:1s,MgO)]}} \quad \ldots\ldots 6.5$$

The calculated curve of equation 6.5 is shown in figure 6.6. Values of θ = 0.3-0.4 encompass the experimental data. The ratio Ba:$3d_{5/2}$ / Mg:1s for the single crystal overlayer study was within the range of values for Ba doped powders and as the doping has been shown to be relatively unimportant in determining surface coverage this can be taken as representative of the saturation coverage associated with the pellets. The LEED patterns, figure 6.7(a) and 6.7(b), from this surface are of a streaky appearance and have a high background intensity, which is indicative of disorder. However careful tuning of the incident electron beam allowed observation of a few distinct 1/4 order super structure spots.

Facetting of the surface can be ruled out in the light of Henrich's study on MgO(111)[12]. Facetted surfaces give an extremely complex LEED pattern with increasing beam energy with spots converging on several different origins. In our experiments the LEED pattern was centered around a single origin. Analysis of the spot pattern shows a d-spacing of 2.6±0.1Å which is between the values 2.106Å and 2.76Å expected for the {20} reflections of MgO and BaO respectively. Assuming a linear Vegard relationship a

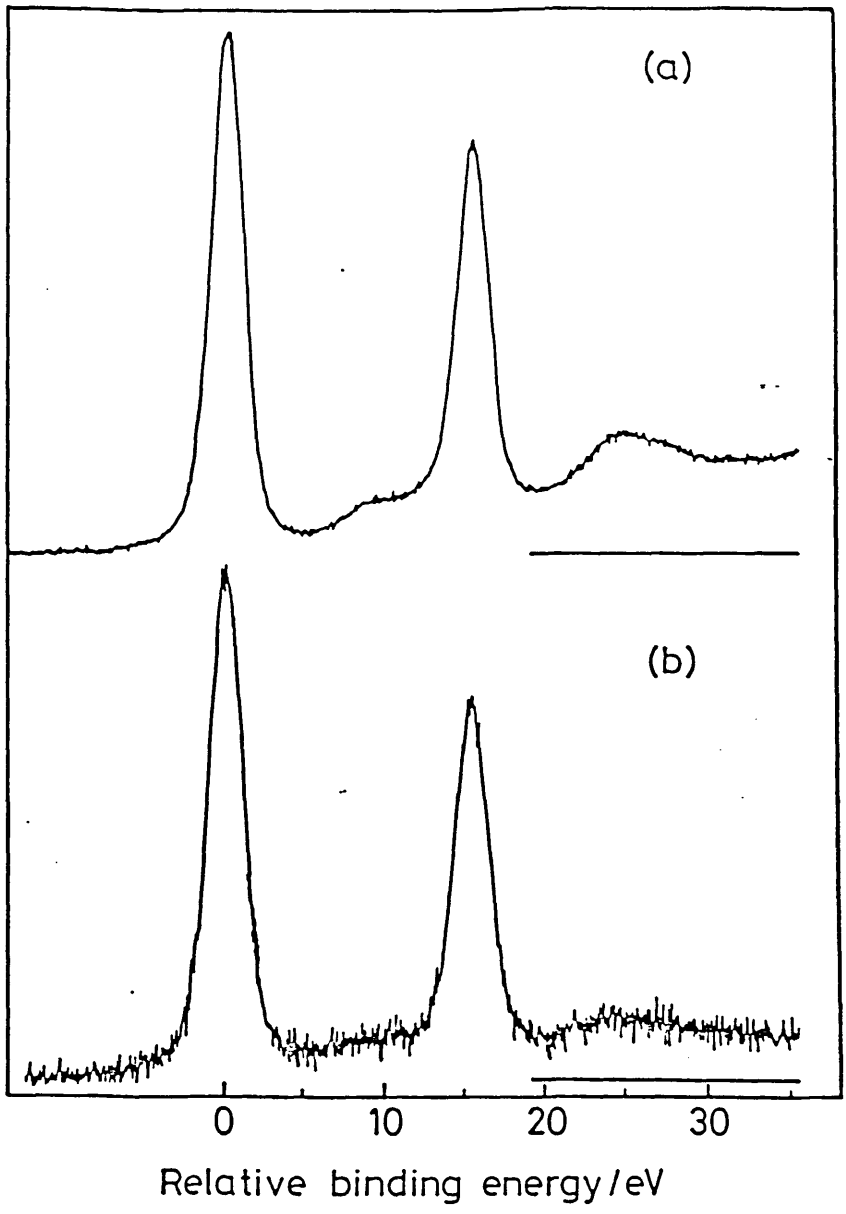


Figure 6.4 Comparison between Ba:3d structure (a) from bulk BaO and (b) from Ba-segregated MgO (70ppm doping level). X-ray satellite structure has been subtracted from these spectra. Note that the intensity of the background and energy loss structure is much weaker in (b) than in (a) by a factor of about 1/2.

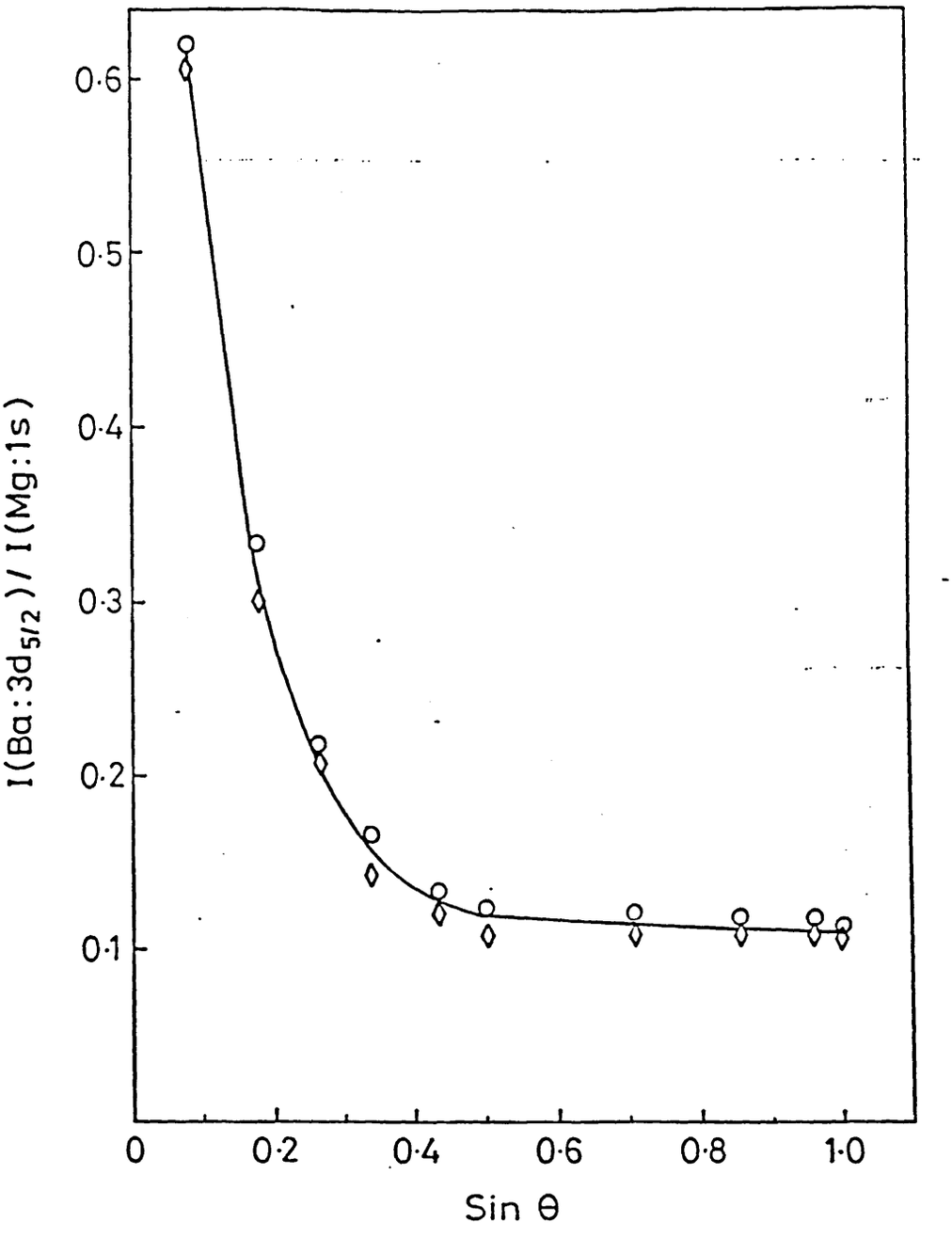


Figure 6.5 The variation of Ba:$3d_{5/2}$ / Mg:1s intensity ratio as a function of take-off angle of photoelectrons θ, for two Ba-doped MgO ceramics. Circles: 7000ppm Ba doping. Diamonds: 700ppm Ba doping. This experiment was performed by L.L.Cao at Tsinghua University, Beijing.

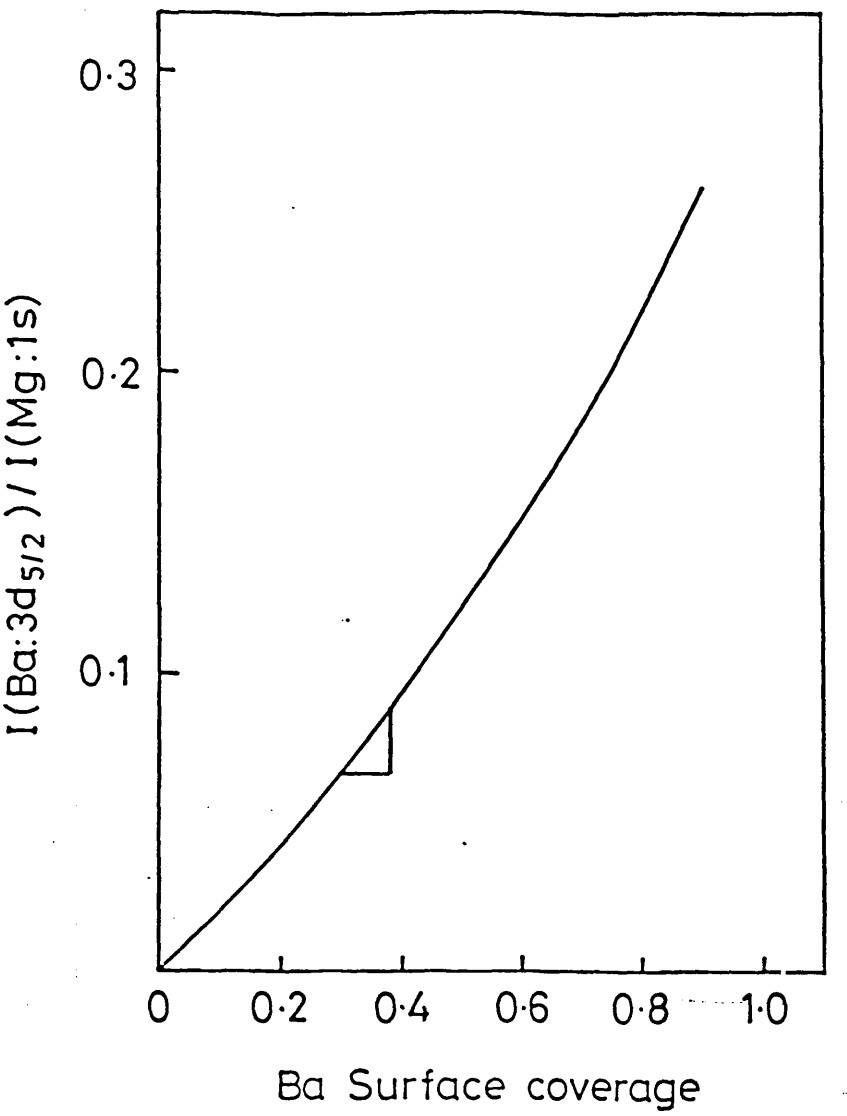


Figure 6.6 The calculated variation of Ba:$3d_{5/2}$ to Mg:1s intensity ratio with substitutional incorporation of Ba at the Mg(001) surface. The range of scatter encompassed by the experimental data is indicated.

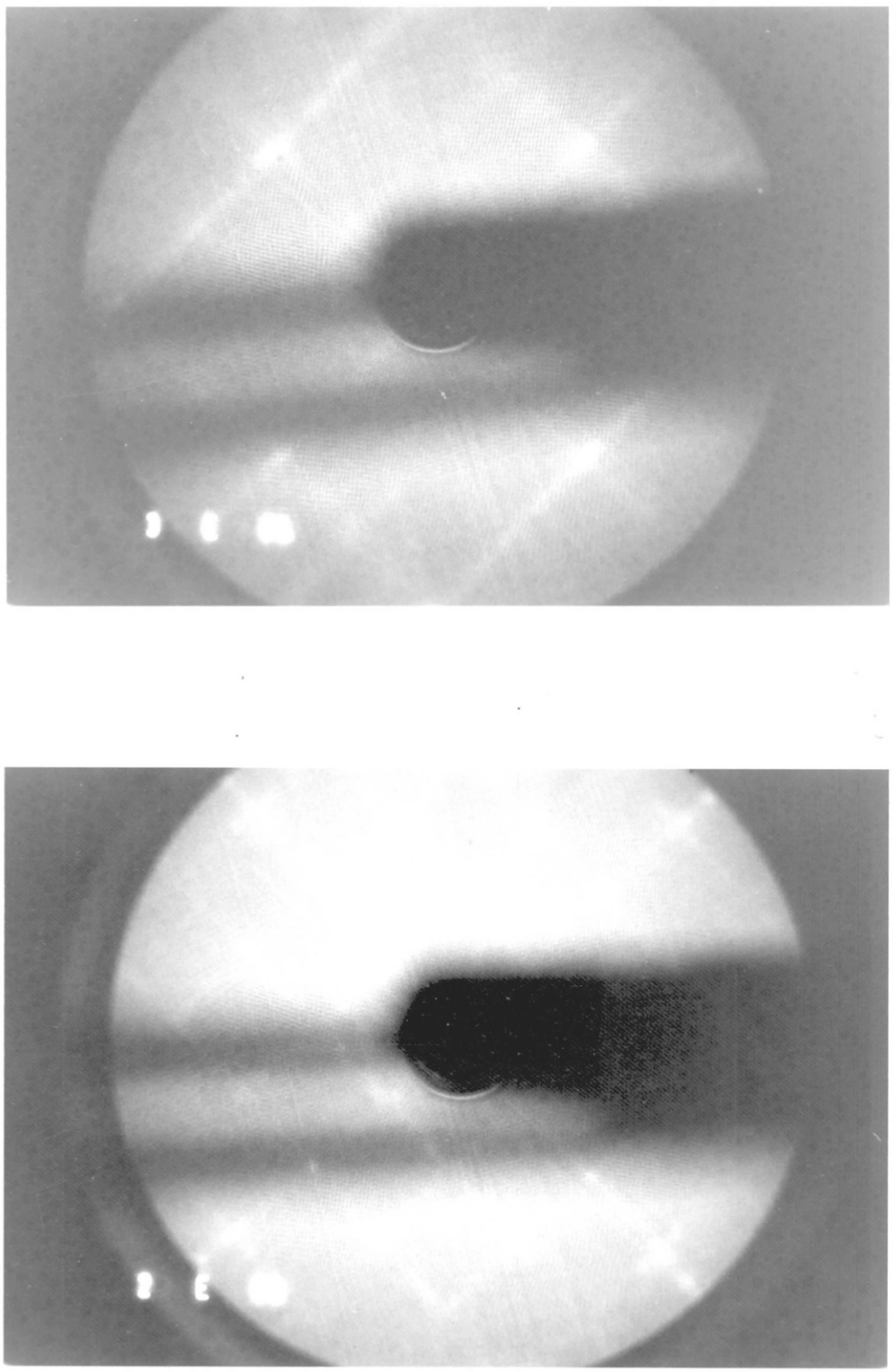
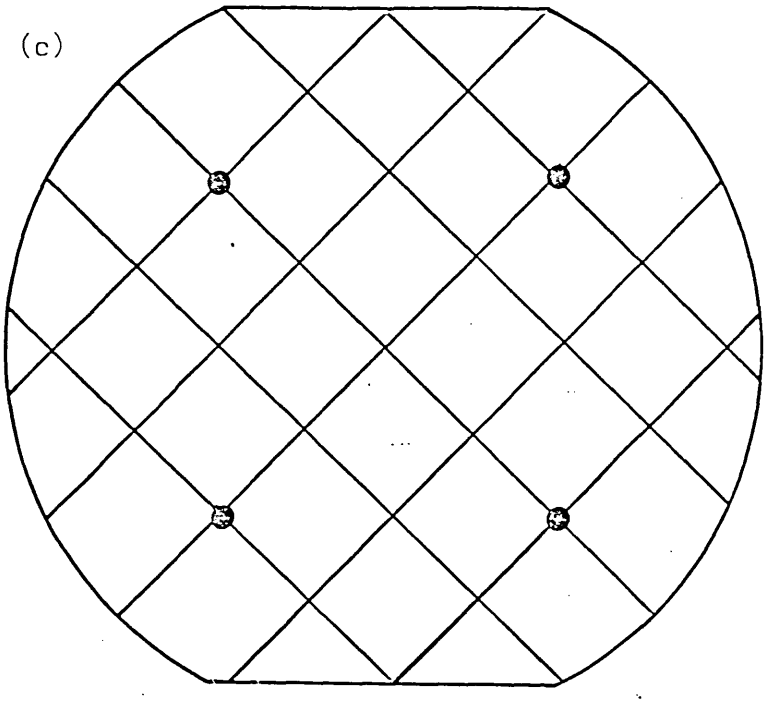
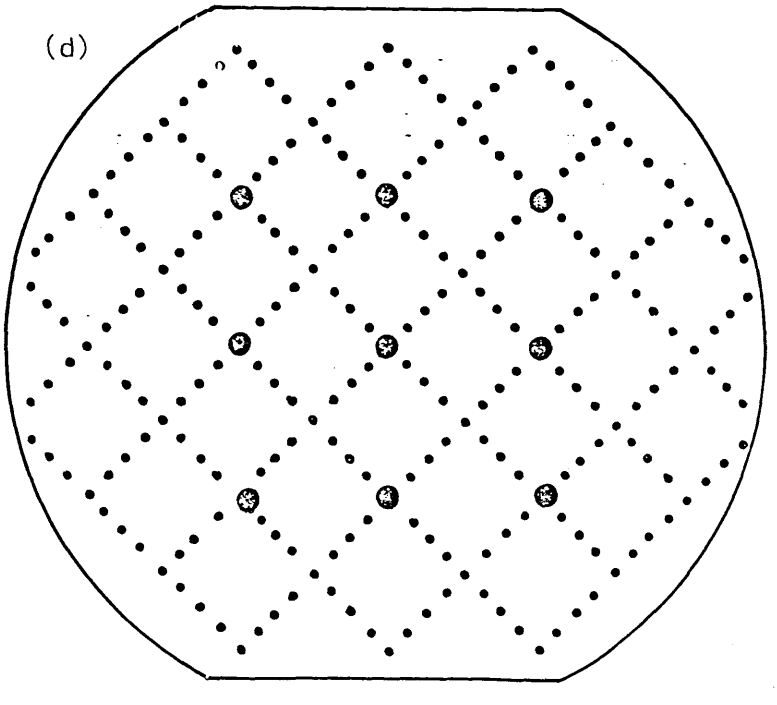


Figure 6.7 LEED patterns for Ba-segregated MgO(001) as descibed in the text (a) 86eV beam energy (b) 115eV beam energy. Idealised patterns corresponding to (a) and (b) are shown in (c) and (d).

(c)



(d)



surface composition of $Ba_{1-x}Mg_xO$ with x = 0.2 is obtained. As the concentration of Ba ions in natural BaO in a specific 2D area is half that of Mg ions in MgO in the same area one arrives again at a surface coverage consistent with θ = 0.3-0.4 . Furthermore an overlayer with a_0 = 5.2Å obeys an approximate coincidence relationship:

$$4a_o(Ba_{1-x}\,Mg_x\,O) = 5a_o(MgO) \quad .... \; 6.6$$

This would give a complex LEED pattern with superlattice spots characteristic of the coincidence lattice. Due to the poor quality of the patterns it is however difficult to pursue a more detailed analysis.

6.4 The heat of segregation

This section involves calculations of heats of segregation using ionic model simulations. The calculations were done at ICI by W.C.Macrodt et al in conjunction with our experimental work. A brief summary of results can be found in table 6.1. The basis for these atomistic simulations lies in the calculation of interionic potentials, and their subsequent use in summations[13][14]. The most versatile calculation of the repulsive part of the potentials is from ab-initio Hartree Fock procedures, and these have been used for this work and elsewhere. The interionic potential involving O^{2-} will be different between the MgO substrate and the BaO overlayer due to the different Madelung potentials which stabilise the O^{2-} atom within the lattice and the problem arises as to which value for the potential to take but for small coverages it can be assumed to be more accurate to use MgO-type potentials and the growth of a complete BaO monolayer must incur a switchover to BaO potentials.

The definition of ΔH_{seg} is the difference in energy between Ba in the bulk and that in the surface. The substitution energy of Ba in bulk MgO is 11.64 eV and for zero coverage the substitution energy into the surface is only 7.74eV giving a heat of segregation at zero coverage of -3.90eV. At 1/4 coverage steric factors play some importance and ΔH_{seg} decreases to -3.01eV. At 1/2 coverage steric overcrowding produces major relaxations and two

basic types of structure were put forward. The first involves the Ba ions constrained to replace the Mg ions substitutionally but allowed free relaxation in the surface layers normal to the surface. Here it really is unclear as to which potentials are to be preferred. With MgO-type potentials two minima were found at ΔH_{seg} of -2.18eV and -1.14eV. With BaO-type potentials correspondingly they were -0.42eV and 0.65eV. Secondly the possibility of more radical structural re-organisation is considered. As before it is noted that a_o(BaO) is 5.52Å and $\sqrt{2}$ a_o(MgO) is 5.96Å giving only a 10% mismatch. This overlayer structure involves ions occupying on-top positions, but there are equal numbers of nearest neighbour attractive and repulsive interactions. Calculations for a monolayer coverage of this structure, using the BaO potentials, give the average energy per Ba ion to be 29.82eV in the overlayer. The energy per Ba ion in bulk MgO is -29.09eV (MgO potential) thus giving ΔH_{seg} for monolayer coverage of -0.73eV which is less than 1/2 monolayer segregation using direct substitution as above. With the addition of more layers of " $\sqrt{2}$ " type BaO monolayers we lower the heat of segrgation further. Treatment of the overlayer summation is computationally difficult if we allow the BaO overlayer to adopt its natural lattice spacing, because of the non-commensurate relationship between $\sqrt{2}a_o$(MgO) and a_o(BaO). The programmes need a coincidence in a 2D surface unit cell which would be prohibitively large in this case. However

the atomic energy per Ba ion in the 'free' overlayer has been calculated and is -30.76eV, a value lower than that calculated for the substitutional case and for the "√2" overlayer. Also this value must be lowered further when the interaction with the MgO surface layer is considered. In fact one monolayer of BaO with its characteristic lattice spacing corresponds to 0.580 in terms of substitutional replacement and we can conclude that as we pass through 1/2 coverage the lowest energy structure is one in which an overlayer of BaO at its own natural lattice spacing sits on top of the MgO surface layer.

The region in which there is a switch from substitutional replacement of Mg to formation of the BaO overlayer is difficult to define, but the LEED results indicate a lattice parameter just below that of BaO at 20% incorporation of Mg into an essentially BaO-like overlayer. The use of MgO- type potentials at low coverages and BaO-type above 1/2 coverage appears therefore to be reasonable and is further discussed in the next section.

6.5 Segregation isotherms

The conventional method of obtaining enthalpies of segregation is from plots of log(surface concentration) against 1/T. This analysis only pertains if ΔH independant of surface coverage and Mackrodt and Tasker[8] have developed a strategy for coverage dependent enthalpies which is used in the present work. In order to explain some deductions a short precis of the methodology follows.

Let g^b and g^s denote free energies of cations in the bulk and surface and similarly for n^b and n^s representing the number of ions. G the total free energy of the system is therefore represented:

$$G = n^b_{Ba} g^b_{Ba} + n^s_{Mg} g^s_{Mg} + n^b_{Ba} g^b_{Ba} + n^s_{Mg} g^s_{Mg} - kT\log_e \Omega \quad \ldots\ 6.7$$

where $\log_e \Omega$ is the configurational entropy of the system.
($k\ln\Omega = k\ln \{ n^b!/n^b_{Ba}!n^b_{Mg}! \times n^s!/n^s_{Ba}!n^s_{Mg}! \}$)

Let Δg be the free energy of segregation excluding configurational entropy such that:

$$\Delta g = (g^s_{Ba} - g^s_{Mg}) - (g^b_{Ba} - g^b_{Mg}) \quad \ldots\ 6.8$$

also let

$$r^s = n^s_{Ba} / n^s_{Mg} \quad \ldots\ 6.9$$

$$r^b = n^b_{Ba} / n^b_{Mg} \quad \ldots\ 6.10$$

As Δg is a function of r^s it is more realistically represented as $\Delta g(r^s)$. At equilibrium $dG/dn^s_{Ba} = 0$ which after manipulation gives:

$$r^s = r^b \exp[(-\Delta g(r^s) + r^s(1 + r^s)\, d\Delta g(r^s)/dr^s)/kT] \quad \ldots\ 6.11$$

To evaluate the surface atomic fraction of impurity we must therefore calculate Δg. Masri et al's [15] calculation of the vibrational entropy contribution to the free energy for Ca^{2+} segregating to MgO(001) at 50% coverage to be only a few percent of the enthalpy contribution(3KJ/mole at 1000K against 40- 100 KJ/mole). Thus the term $T\Delta S_{seg}$ can be neglected. Equation 6.11 can therefore be rewritten:

$$r^s = r^b \exp[(-\Delta h(r^s) + r^s(1 + r^s)\, d\Delta h(r^s)/dr^s)/kT] \quad .... 6.12$$

over a limited range we may assume a linear relationship of the sort:

$$r^s = r^b \exp[-\Delta h_{eff}/kT] \quad .... 6.13$$

Equation 6.12 must be solved numerically to obtain r^s from r^b and the known variation of $\Delta h(r^s)$ with r^s. This has been done for both MgO and BaO potentials and for a case where we switch over to Mgo potentials at low coverage to BaO potentials at high coverage. The results are summarised in table 6.1 and plotted as $\ln(r^s)$ against $10^4/T$ in figure 6.8.

It is obvious that the equilibrium surface coverage is very dependent on the potentials chosen and as such it is necessary to rationalise what they mean. Section 6.4 indicates that there is a switch over from MgO potentials at low coverage to BaO potentials at 1/2 coverage. (This

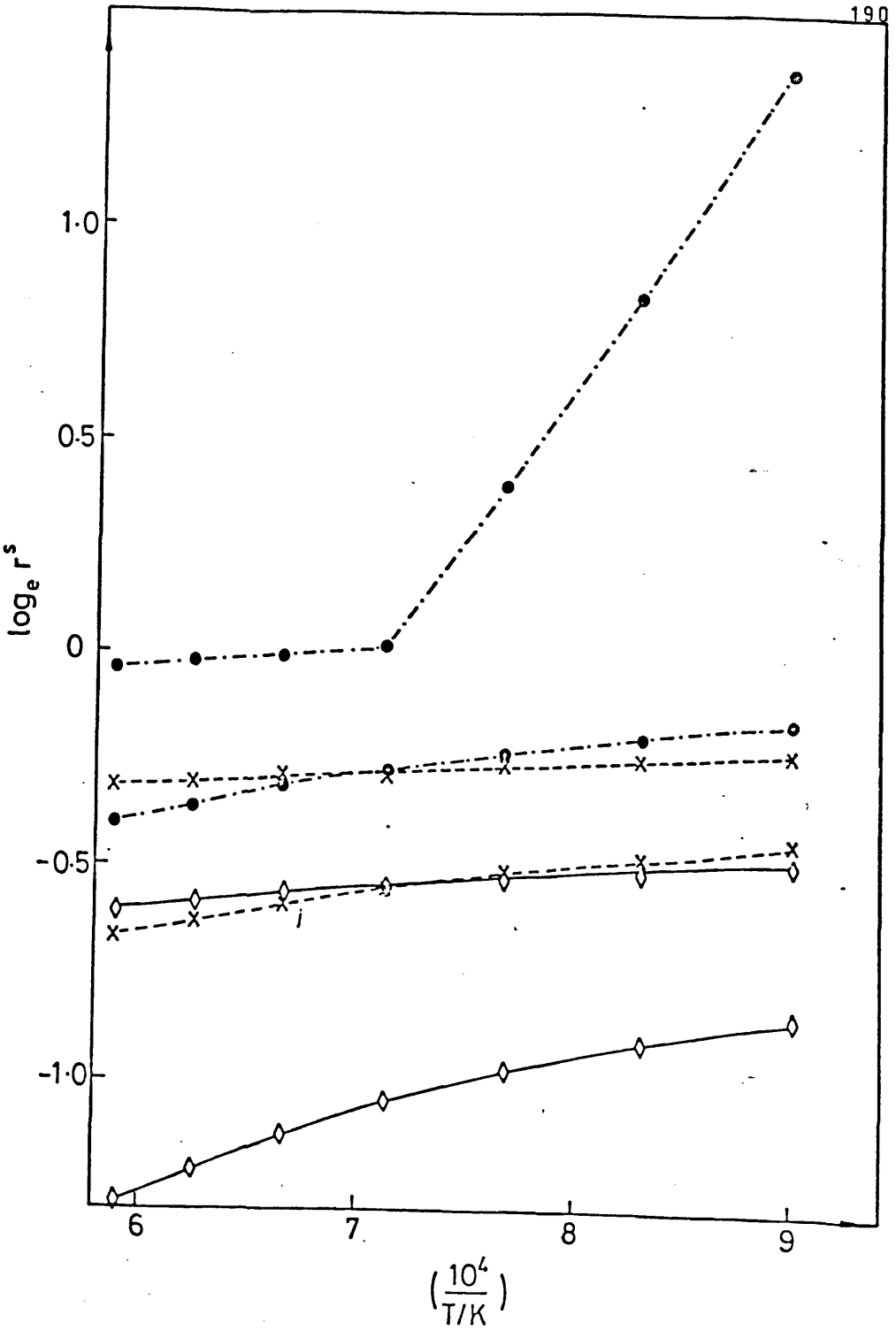


Figure 6.8 Surface coverages of Ba at Mg(001) as a function of temperature for 7000ppm and 7ppm above and below respectively. Dash dot lines: MgO potentials. Solid lines: BaO potentials. Dash lines: intermediate potentials.

is the "natural" BaO monolayer discussed). The use of "intermediate" potentials is therefore appropriate to descibe complete isotherms. Figure 6.8 also shows that apart from the 7,000ppm sample the coverage is not strongly dependent on temperature.

In fact for the 7ppm doping and intermediate potentials, the slope of $\log_e r^s$ versus 1/T is only about 688K. For this particular (and looking to the experimental results most representative of the system) case using equation 6.13 to calculate ΔH_{eff} gives a value of only 0.06eV. This is because ΔH_{eff} is comprised of two parts the ΔH_{seg} term and the term in $d\Delta H_{seg}/dr^s$. The first term is large and negative and the second positive. The latter positive term is largest for intermediate potentials and we obtain a variation of coverage only very weakly dependent on temperature. The calculated surface coverage is also insensitive to the huge amount of change of bulk doping as shown by the superimposed plot on figure 6.3. The expected ratio without segregation differs greatly from the theoretical ratio with segregation. The experimental ratios agree very well with the simulation results which is a gratifying conclusion to this piece of work.

Table 6.1

Heats of segregation of Ba to MgO(001)

MgO lattice energy	40.73eV
BaO lattice energy	32.04eV
Defect energy of Ba^{2+} in MgO	11.64eV

(1) Heat of segregation of Ba in MgO by substitutional replacement of Mg surface cations (/eV)

Coverage	MgO potentials	BaO potentials
0	-3.90	-2.45
1/4	-3.01	-1.55
1/2 (a)	-2.18	-0.42
1/2 (b)	-1.14	+0.65
1	-1.37	

(2) Heat of segregation of Ba into BaO overlayers bound to MgO with BaO lattice parameter constrained to $a(BaO)=\sqrt{2}a(MgO)$ (/eV)

Number of BaO layers	MgO potentials	BaO potentials
1	-1.38	-0.73
2	-2.53	-1.76
3	-2.99	-1.99
4	-3.08	-2.15

(3) Heat of segregation of Ba into free BaO layers at the natural lattice spacing

Number of BaO layers	BaO potentials
1	-1.67
2	-2.33
3	-2.53
4	-2.64
∞	-2.95

References

References for chapter 1

(1) A.Einstein

Ann.Physik 17 132 (1905)

(2) Solid State Physics

N.Ashcroft and N.Mermin

Holt-Saunders Japan Ltd. (1981)

(3) T.Koopmans

Physica 1 104(1934)

(4) Topics in Applied Physics

Photoemission in solids (II)

eds. L.Ley and M.Cardo na

(5) C.N.Berglund and W.G.Spicer

Phys.Rev. 136A 1030(1964)

(6) M.Karolevski

Ph.D. Thesis Imperial College London 1980

(7) Topics in Applied Physics

Photoemission in solids (I) & (II)

eds.L.Ley and M.Cardo na

(8) "Practical surface analysis by Auger and X-ray

photoelectron spectroscopy"

eds. D.Briggs and M.P.Seah

John Wiley & sons Chichester 1981

(9) M.P.Seah

Surface Interface Anal. 2 222(1980) and

M.P.Seah and W. A. Dench

Surface Interface Anal. 1 2(1979)

(10) J.Szajman, J.G.Jenkin and R.C.G.Leckey

J. Electron Spectrosopy 23 97(1981) & 23 83(1981)

(11) Hand book of X-ray and UV Spectroscopy

ed. D.Briggs (Heyden 1977)

(12) Esca: Atomic, molecular and solid state structure

studied by means of electron spectroscopy

K.Siegbahn et al

Almqvist & Wiksells Uppsala 1967

(13) Kratos Analytical (workshops)

Barton Dock Rd. Manchester 1985.

(14) D.N.Hendrickson, J.M.Hollander and W.L.Jolly

Inorg. Chem 8 2642(1969)

(15) ESCA applied to free molecules.

K.Siegbahn etal

North Holland, Amsterdam 1961

(16) J.W.Cooper

Phys.Rev 128 681(1982)

(17) P.H.Citrin and P.M.Eisenberger

Phys. Rev. B 10 1762(1974)

(18) C.Devey

J.Phys. C7 1 335(1979)

(19) S.Evans and M.D.Scott

Surf.Interface Anal. 3 269(1981)

(20) D.A.Shirley

Phys. Rev B5 4709(1972)

(21) Low energy electron diffraction

J.B.Pendry

in Techniques of Physics Series

eds G.K.T.Conn and K.R.Coleman

(Academic Press New York 1974)

(22) J.S.Lander

Progress in Solid state chemistry 2 26(1965)

(23) J. H. Scofield
J. Elec. Spec. Relat. Phenom., 8 129 (1976)

(24) S. Evans, R. Pritchard and J. Thomas
J. Elec. spec. Relat. Phenom., 14 341 (1978)

References for chapter 3

(1) I.Stubican, R.C Huil and S.P.Ray

J.Am.Ceram.Soc 61 17 (1978)

(2) P.Duwez, Frank. H. Brown Jr., and Francis Odell

J.Electrochem. Soc. 98 356 (1951)

(3) T.H. Etsell and S.N. Flengas

Chem. Rev. 70 339 (1970)

(4) D.S.Tannhauser, J.A.Kilner and B.C.H.Steele.

Proceedings of the Sixth International Conference of Ion Beam Analysis, Tempe, Arizona, 1983.

(5) L.J.Olmer, J.C.Viguie and F.J.L.Schouler.

Solid State Ionics 7 23 (1981)

(6) V.A.Loebs,T.W.Haas and J.S.Solomon

J. Vac. Sci. Technol. A 2, 596 (1983)

(7) W.J.A Winnbust, A.J.Burrgraaf and P.J.M Kroot

J. Phys.Chem.Solids 44 955(1983)

(8) J.S.Solomon and J.T.Grant

J. Vac. Sci. Technol. A 3 373(1985)

(9) Low energy electron diffraction

J.B.Pendry

Techniques of physics series

eds G.K.T.Conn and K.R.Coleman

Academic Press New York (1974)

(10) P.W.Tasker

J.Phys.C. 12 4977(1979)

(11) T.N.Taylor and W.P.Ellis

Surf. Sci. 77 321(1978)

(12) M.Prutton and M.R.Welton Cook

Surf. Sci. 88 (1979) L9

(13) V.E.Henrich

Surf. Sci 57 385(1976)

(14) T.N.Taylor and W.P.Ellis

Surf. Sci. 107 249 (1981)

(15) P.W.Tasker

Surf. Sci.78 315(1979)

(16) M.S.Hegde, A Srinivasan, D.D. Sarma and C.N.R Rao

J.Electron Spectrosc. 25 231-236(1982)

(17) D.K.G deBoer , C Haas and G.A Sawatzky

Phys. Revs. B 29 4401(1984

(18) The Oxide Handbook

ed. G.Samsonov

IFI/Plenum New York (1982)

(19) M.A.Langell and S.L.Bernasek

J. Vac. Sci. Technology 17 1287(1980)

(20) M.L. Knotek and P.J.Feibelman

Phys. Rev. Lett. 40 964 (1978)

(21) V.E. Henrich, G.Dresselhaus and H.J.Zeiger

Phys. Rev. Lett. 36 1335(1976)

(22) G.D.Watts, A. R. Jones and B.J. Hopkins

Surf. Sci. 45 705(1974)

(23) K.S.Kim, W.E. Baitinger, J.W.Amy and N.Winograd

J.Electron Spectrosc. 5 351(1974)

(24) Auger Electron spectroscopy

eds. M.O.Thompson, M.D.Baker A.Christie and J.F.Tyson

Wiley, New York (1985)

(25) R.Holm and S.Storp

Appl. Phys. 12 101 (1977)

(26) Transition metal oxides.

C.N.R.Rao and G.V.Subba Rao,

National Bureau of Standards U.S. Government Printing

Office, Washington 1974

(27) J.Szajman and C.G.Leckey

J.Electron Spectrosc. 23(1981)83

(28) V.E. Henrich

Surf. Sci. 57 385 (1976)

References for chapter 4

(1) M.Causa, R.Doveri, C.Pisani and C.Roetti
Surf. Sci 175 551(1986)

(2) E.A.Colbourn, W.C. Mackrodt and P.W.Tasker
Journal of Material Science 18 1917(1983)

(3) P.W.Tasker
J.Phys C: Solid State Physics 12 4977(1979)

(4) F. Henrich
Surf. Sci. 57 385(1976)

(5) K.O.Legg, M.Prutton and C.G.Kinniburgh
J.Phys. C 7 4236 (1974)

(6) P.H.Citrin and G.K.Wertheim
Phys. Rev. B 27 N^{o} 6 3176 (1983)

(7) Computer simulation of solids
Lecture notes in physics 166(1981)
Ed. C.R.A.Catlow and W.C.Mackrodt
Springer-Verlag 1985

(8) E.A.Colbourn and W.C.Mackrodt
Solid State Ionics 8 221(1983)

(9) D.E.Parry
Surf. Sci. 49 433(1975)

(10) R.E.Watson J.W.Davenport M.L.Perlman and T.K.Sham
Phys. Rev. B 24 1791(1981)

(11) B.Cord and R.Courths
Surf. Sci. 162 34(1985)

(12) C.M Timesdale S.H. Southworth D.H. Kobin
D.W.Lindle, G.Thornton and D.A.Shirley

J.Chem.Phys 76 860(1982)

(13) J.F.van der Veen, P.Heinmann F.J.Himpsel and D.E.Eastman
Solid State Commun. 38 595(1981);

(14) J.F. van der Veen, P.Heinmann F.J.Himpsel and D.E.Eastman
Solid State Commun 37 535(1981)

(15) J.F. van der Veen, F.J.Hinsel and D.E.Eastman
Phys. Rev. Lett. 44 189(1980)

(16) D.E.Fastman, T.C.Chang , P.Heiman and F.J.Himsel
Phys. Rev. Lett 45 656(1980);45 1112(1980)

(17) P.H.Citrin and G.K.Wertheim
Phys. Rev. B 27 3176(1983)

(18) P.R. Webber, Z.G.Zhang and M.A.Morris
J.Phys. F: Met. Phys 15 249(1985)

(19) P.R.Webber and M.A.Morris
Phys. Rev. B 29 5957(1984)

(20) D.A.Shirley, R.L.Martin S.P.Kowalczyk, F.R.McFreeley and L.Ley
Phys. Rev. 15 544(1977)

(21) P.A.Cox and A.A.Williams
Surf. Sci. , 175(1986) L782

(22) A.A.Williams PhD Thesis Oxford 1985

(23) W.J.Gignac, R.Stanley Williams and S.P.Kowalczyk
Phys.Rev.B 32 1237(1985)

(24) J.Szajman, J.Liesegang, J.G.Jenkin and R.C.G.Leckey
J.Electron Spec. 23 97(1981)

(25) D.K.G. de Boer, C.Haas and G.A.Sawatzky

Phys. Rev. B 29 8(1984)

(26) S.Hagstrom, C.Nordling and K.Siegbahn

Phys. Lett. 9 235(1964)

(27) P.A.Cox, R.G.Egdell, J.B.Goodenough, A.Hamnett and C.C.Naish

J. Phys. C, 16 6221 (1983)

(28) P.H.Citrin and P.M.Eisenberger

Phys. Rev. B 10 1762(1974)

(29) Photoemission in Solids

eds. M.Cardon a and L.Ley

Springer Verlag 1978

(30) M.Iwan and C.Kunz

Phys. Lett 6 345(1977)

(31) C.S.Fadley, S.B.M.Hagstrom, M.P.Klien and

D.A.Shirley

J.Chem. Phys 48 3779(1968)

(32) E.A.Colbourn and W.C.Mackrodt

J. Mat. Sci. 17 3021(1982)

(33) C.S.Fadley, S.B.M.Hagstrom, M.P.Klien,D.A.Shirley

J.Chem. Phys. 48 3779(1968)

(34) C.Kittel

"Introduction to Solid State Physics"

(Wiley&Sons 5th Ed. 1976)

(35) W.C.Mackrodt

To be published

(36) K.H.Reider

Surf. Sci., 57 118(1982)

Refences for chapter 5

(1) B.D.Campbell, G.A. Haque and H.F.Farnsworth in
The structure and chemistry of solid surfaces
ed. G.A.Somorjai Wiley New York 1969

(2) Computer simulation of solids
ed. C.R.A.Catlow and W.C.Mackrodt
Springer Verlag, Berlin 1982

(3) R.C.McCune and P.Wynblatt
J. Amer. Ceram. Soc: 66 11(1983)

(4) W.C.Macrodt and R.F.Stewart
J.Phys.C 125051(1979)

(5) E.A.Colbourn and W.C.Mackrodt
J.Mater.Sci. 17 3021(1982)

(6) Practical surface analysis by auger and X-ray
photoelectron spectroscopy.
D.Briggs and M.P ..Seah
John Wiley & sons 1983

(7) J.B.Pendry
Low Energy Electron Diffraction
Academic Press, London 1976

(8) Electron energy loss spectroscopy and surface
vibrations
H.Ibach and D.L.Mills Academic Press 1982

(9) P.W.Tasker, E.A.Colbourn and W.C.Mackrodt
J.Am. Ceram. Soc : 68 74(1985)

(10) SAES Getters ITALY

(11) J.H.Sc ofield

J. Electron Spect 8 129(1976)

(12) S.D.Parker

Surface Science (1986)

(13) D.Chadwick and M.A.Karolewski

Surf. Sci 126 41(1983)

(14) G.K.Wertheim

J.Electron. Spect. 34 309(1984)

(15) J.Szajman and R.C.G.Leckey

J.Electron. Spect. 23 83(1981)

(16) J.Szaj man, J.Liesegang, J.G.Jenkin and

R.C.G.Leckey

J.Electron. Spect.23 97(1981)

(17) M.P.Seah and W.A. Dench

Surf. Sci. 175 (1986)L782

(18) A.R.Protheroe, A.Steinbrunn and T.E.Gallon

Surf.Sci 126 534(1983)

(19) D.W.Pashley

Advances in Physics 5 173(1956)

(20) K.O.Legg, M.Prutton and C.G.Kinniburgh

J.Phys.C.7 4236(1974)

References for chapter 6

(1) S.Bank, D.E.Fowler, J.M.Blakely and R.Raj
J. Am. Ceram. Soc. 68 281(1985)

(2) R. C. McCune, W.T.Bonean and R.C.Ku
J. Am. Ceram. Soc. 69 C 196(1986)

(3) P.W.Tasker, E.A.Colbourn and W.C.Mackrodt
J. Am. Ceram. Soc 68 74(1985)

(4) W.C.Macrodt, P.W.Tasker
Mat. Res. Soc. Symp. Proc 60 291(1986)

(5) R.C.McCune and P.Wynblatt
J.Am. Ceram. Soc 66 111(1983)

(6) A. Cimino, B.A.de Angelis, G.Minelli, T.Persin and P. Scarpini
J. Solid State Chem. 33 403(1980)

(7) E.A.Colbourn and W.C. Mackrodt
J. Mat. Sci. 18 1917(1983)

(8) W.C.Mackrodt and P.W.Tasker
Surf. Sci. submitted

(9) J.Szaj man and R.C.G. Leckey
J.Electron Spect. 23 83(1981)

(10) J.Szaj man, J.Liesegang, J.G.Jenkin and R.C.Leckey
J.Electron. Spec 23 97(1981)

(11) S.Tougaard and A.Ignatiev
Surf. Sci. 129 355(1983)

(12) V.E.Henrich
Surf. Sci. 57 385(1976)

(13) Computer simulation of solids

Eds C.R.A.Catlow and W.C.Macrodt

Springer Verlag Berlin (1982)

(14) C.R.A.Catlow in Solid state chemistry

Eds P.Day and A.K.Cheetham

Elsevier Amsterdam 1987

(15) P. Masri, P.W.Tasker, J.P.Hoare and J.H.Harding

Surf. Sci. 173 439(1986)

Appendix A

If the attenuation is determined by λ ,the IMFP, we can assume that the intensity of an XPS peak for a single crystal of atomic spacing a can be represented by the progression:

$$I = A\sigma \left(1 + e^{-a/\lambda} + e^{-2a/\lambda} + \ldots . e^{-na/\lambda} \right) \qquad \ldots . A.1$$

Where n indexes the number of atomic layers of the crystal, σ is the ionisation cross section and A is a constant absorbing the other terms shown in equation 1.1.
From the arithmetic progression:

$$\sum_{n=1}^{\infty} br^{n} = b \,/\, 1-r \qquad \ldots . A.2$$

We can formulate:

$$I = \frac{Ao}{(1-e^{-a/\lambda})} \qquad \ldots . A.3$$

The objective is to replace the terms involving the cross section and transmission function with terms calculated from equations similar to A.3 knowing the intensity I from experiment. Hence if λ,a and I are known we obtain a magnitude for $A\sigma$. This can then be replaced in other equations.

For example if we use the known intensity of a peak for pure BaO and MgO to determine peak intensities of overlayers of BaO on MgO.

For the BaO crystal alone:

$$\frac{I[Ba:3d_{5/2}]}{I[O:1s]} = \frac{\sigma(Ba:3d_{5/2})}{\sigma(O:1s)} \times \frac{1-\exp[-a_o(BaO)/2\lambda(O:1s,BaO)]}{1-\exp[-a_o(BaO)/2\lambda(Ba:3d_{3/2},BaO)]} \times \frac{T(Ba:3d_{5/2})}{T(O:1s)} \times \frac{C(Ba)}{C(O)} \quad ....A.4$$

For the MgO cystal alone we take a similar ratio (I[Mg:1s]/I[O:1s]). The ratio R_c between $Ba:3d_{5/2}$ and Mg:1s intensities of the pure compounds each normalised to the O:1s intensity was found to be 1.56. Now R_c must be given:

$$R_c = \frac{\sigma(Ba:3d_{5/2})}{\sigma(Mg:1s)} \times \frac{1 - \exp[-a_0(MgO)/2\lambda(Mg:1s,MgO)]}{1 - \exp[-a_0(BaO)/2\lambda(Ba:3d_{5/2},BaO)]} \times \frac{1 - \exp[-a_0(BaO)/2\lambda(O:1s,BaO)]}{1 - \exp[-a_0(MgO)/2\lambda(O:1s,MgO)]} \times \frac{T(Ba:3d_{5/2})}{T(Mg:1s)} \quad ....A.5$$

where:

σ are subshell ionisation cross sections

a_0 are lattice parameters

λ are electron pathlengths for the specified photoelectrons in a given oxide

T are instrumental transmission factors

For overlayer studies allowance must be made for the attenuation of the substrate signal by the overlayer. Therefore for n monolayers of BaO on MgO the intensity ratio between $Ba:3d_{5/2}$ and Mg:1s peaks R_n is given by:

$$R_n = \frac{o(Ba:3d_{5/2})}{o(Mg:1s)} \times \frac{a_0(MgO)^2}{a_0(BaO)^2} \times \frac{1 - \exp[-a_0(MgO)/2\lambda(Mg:1s,MgO)]}{\exp[-na_0(BaO)/2\lambda(Mg:1s,BaO)]}$$

$$\times \sum_{j=0}^{n-1} \exp[-ja_0(BaO)/2\lambda(Ba:3d_{5/2},BaO)] \times \frac{T(Ba:3d_{5/2})}{T(Mg:1s)} \quad \ldots.A.6$$

We can hence formulate an expression for R_n independent of the cross sections and transmission function terms:

$$R_n = R_c \times \frac{a_0(MgO)^2}{a_0(BaO)^2} \times \frac{1 - \exp[-a_0(MgO)/2\lambda(O:1s,MgO)]}{1 - \exp[-a_0(BaO)/2\lambda(O:1s,BaO)]} \times$$

$$\sum_{j=0}^{n-1} \frac{\exp[-ja_0(BaO)/2\lambda(Ba:3d_{5/2},BaO)]}{\exp[-na_0(BaO)/2\lambda(Mg:1s,BaO)]} \times$$

$$\{1 - \exp[-a_0(BaO)/2\lambda(Ba:3d_{5/2},BaO)\} \quad \ldots. A.7$$

This equation can be used to calculate the expected intensity at a specific coverage and therefore we can assume a specific coverage for our experimental results.

Fractional coverages for BaO on MgO

(1) The case for between 0 and 1 monolayer of BaO

For simplification let

$\exp[-a_0(BaO)/2\lambda(Mg:1s,BaO)] = P$

$\exp[-a_0(BaO)/2\lambda(Ba3d5/2,BaO)] = L$

If I_1 is the intensity of Mg:1s with one monolayer of BaO and I_0 the intensity without any overlayer then:

$$I_1 = I_o \times P \qquad \text{.... A.8}$$

If I_2 is the intensity from one monolayer of BaO (no self attenuation) then in the case of φ(BaO) coverage where φ is a fraction between 0 and 1 :

$$\frac{I(BaO)_u}{I(MgO)} = \frac{I_2 \times \varphi}{[(1 - \varphi)\, I_1]/P + \varphi I_1} \qquad \text{.... A.9}$$

$$= \frac{I_2}{I_1} \times \frac{\varphi P}{(1 - \varphi) + \varphi P} \qquad \text{.... A.10}$$

$$= R_1 \times \frac{\varphi P}{(1 - \varphi) + \varphi P} \qquad \text{.... A.11}$$

(2) For the general case:

Let I_3 be the intensity of Mg:1s passing through n layers of BaO and I_n be the intensity of Ba:$3d_{5/2}$ from n layers.

If $\varphi(BaO)_n$ is the coverage on the n^{th} layer where φ is a number between 0 and 1 then:

$$I_{n+\varphi}(MgO) = (1 - \varphi) I_{Mg} + \varphi I_{Mg} P \qquad \text{.... A.12}$$

$$I_{n+\varphi}(BaO) = \varphi(\, I_{n+1}\,) + (\, 1 + \varphi\,)\, I_n \qquad \text{.... A.13}$$

Allowing for self attenuation of the BaO overlayers gives:

$$I_n = I_2 \sum_{i=0}^{n-1} e^n P \qquad \text{.... A.14}$$

$$I_{n+1} = I_2 \sum_{i=0}^{n-1} e^n L \qquad \text{.... A.15}$$

From A.14 and A.15

$$I_{n+1} = I_n \times \frac{\sum_{i=0}^{n} e^n P}{\sum_{1=0}^{n-1} e^n L} = I_n M \qquad \text{.... A.16}$$

From equations A.13 and A.16

$$I_{n+\varphi} = \varphi M + (1-\varphi) I_n \qquad \text{.... A.17}$$

We can hence formulate the ratio:

$$R_{n+X} = \frac{I(Ba:3d_{5/2})}{I(Mg:1s)} = \frac{I_n [(1-\varphi) + \varphi M]}{I_3 [(1-\varphi) + \varphi P]} \qquad \text{.... A.18}$$

As $I_n / I_3 = R_n$

$$R_{n+\varphi} = R_n \times \frac{(1 -\varphi) + \varphi M}{(1 - \varphi) + \varphi P} \qquad \text{.... A.19}$$

From this equation all the fractional points between the overlayers were calculated.

Appendix B

The calculation of the plasmon energy and MFP's

Szajman and Leckey* showed that λ can be described by the formula giving a dependence on KE of the form $AE^{3/4}$ where A is the sample-dependent. They formulate:

$$\lambda(E) = \frac{1.8\bar{E}E^{3/4}}{E_p^2}$$

Where E_p is the plasmon energy characteristic of the valence electrons such that:

$$E_p = 28.8(\rho Z/A)^{1/2}$$

$\bar{E}$ is the centroid of the optical loss function which approximates to:

$$\bar{E} = E_p + E_g$$

Where E_g is the band gap. A correction to the plasmon energy to include the bandgap energy (interaction of valence electrons) such that:

$$E_p = (E_p^2 + E_g^2)^{1/2}$$

allows more accuracy.

Values of λ calculated by this method are within the bounds of the co-called universal curve. The calculated bulk and surface plasmons are also in very good agreement with the experimentally determined value (See chapter 3).

* Refs for ch 6, N°s 9, 10